Critical, statistical, and thermodynamical properties of lattice models

Dissertation
zur
Erlangung des Doktorgrades (Dr. rer. nat.)
der
Mathematisch-Naturwissenschaftlichen Fakultät
der
Rheinischen Friedrich-Wilhelms-Universität Bonn

von
Vipin Kerala Varma
aus
Cochin, India

Bonn, 2013

Abstract

In this thesis, we investigate zero temperature and low temperature properties of lattice models as realized in and applicable to condensed matter systems and optical lattices. Optical lattices - created using counterpropagating laser beams - can mimic a clean lattice model of a material, thereby opening up the doorway towards accurate simulation of the latter. We treat lattice models of these systems where the interactions between the constituent particles range from very weak to very strong.

In the first part of the thesis, we separately consider the effects of the kinetic energies and potential energies of the constituent particles in the lattice model. In the non-interacting limit, we use the formalism of lattice Green's functions to compute the density of states of three related lattices: kagome, diced and hyperkagome. Such tight-binding descriptions are realized in materials like graphene and are useful as starting points to analyse the effects of turning on the inter-particle interactions.

In the opposite limit of immobile and interacting particles, we consider Ising spins on quasi-one dimensional ladders and the kagome lattice at their respective saturation fields, the latter physics being realized at the saturation field of the spin ice compound $Dy_2Ti_2O_4$. We accurately evaluate the zero temperature entropy at this phase point using transfer matrix methods and Binder's algorithm, and compare with the available experimental value. Our method of constructing higher dimensional lattices from lower dimensional ones can be similarly used, in conjunction with Binder's algorithm, to accurately evaluate the partition functions of large spin systems in complex lattice geometries.

In the next part of the thesis, the effects of both kinetic and potential energy terms are included in the lattice model. The soft-core and hard-core Bose-Hubbard models, which are realized in optical lattices and bosonic systems like Helium-4, are investigated using linked cluster expansions and spin-wave theory. We study the effect of introducing three and four body interactions in the soft-core Bose-Hubbard model in one and two dimensional systems using linked cluster expansions. We formulate a novel scheme to fully renormalize the two body interactions from the addition of these higher body interactions, and show that the latter preserve the universality of the transition between two of the zero temperature phases in the model - the Mott insulator and superfluid. These results will aid in a better understanding of the physics in optical lattice experiments where higher body interactions in bosons can be controllably manipulated.

In the hard-core Bose-Hubbard model with nearest neighbour interactions, we formulate a spin wave theory for a d-dimensional hypercubic lattice and compare with quantum Monte Carlo simulations for the square and simple cubic lattice models; we find good agreement between the two approaches in the weak to moderate coupling limits. Our comparison of the phase diagrams in one to three dimensions using various methods provides a good gauge for the effect of fluctuations in the model upon changing dimensionality.

On the kagome lattice, the same model is investigated using numerical linked cluster expansions at finite temperatures. We compute thermodynamic quantities like system compressibility, internal energy, specific heat and Grüneisen parameter for various coupling strengths and fillings. We provide evidence for a weak first order transition between the valence bond solid and the superfluid phases at zero temperature using Grüneisen parameter scaling. In the immobile or Ising limit, the transition to the polarized state from the 1/3-filled phase is shown to be a first order transition. Low temperature scaling of the specific heat in the Ising limit at small fillings suggests the presence of low energy excitations in this compressible regime. Our results are relevant for extensitons to the recent realizations of hard-core bosons on optical lattices, and the investigation of the transitions and phases therein.

Contents

Introduction

Condensed matter systems are physical systems where the constituent particles are lumped or condensed together so as to render unique properties to the whole system. Such systems comprise a wide range of materials, substances and phenomena. For instance: the physics of transistors, superconductors, and alloys; the properties of gaseous plasma, nuclear matter, and matter within neutron stars; the nature of superfluidity, antiferromagnetism, and phase transitions; and so on.

The dualist or Cartesian approach to scientific problems has traditionally been one where the system is broken up into smaller parts and each part is then studied separately; this has been the long-followed reductionist strategy in science which has worked quite well. However, oftentimes the system to begin with is sufficiently complex and interesting in and of itself that it neither becomes useful nor convenient to break it up into smaller parts. Consider, for instance, an ideal gas of hydrogen atoms in an otherwise empty room; at high temperatures (room temperature) and low pressures (atmospheric pressure), quantum effects may be ignored and the ideal gas law relating pressure P, temperature T, volume V and number of moles n is given by

$$PV = nRT, \tag{1.1}$$

where R is the universal gas constant. No single hydrogen atom in isolation has a pressure or temperature associated with it, and therefore these are properties which apply only to the entire collection. No amount of knowledge about a single hydrogen atom, even within its fullest quantum mechanical description of orbitals, energy spectrum and suchlike, can ever predict (1.1) that governs the behaviour of the collection. Therefore, although an approximation, (1.1) is a law that has *emerged*. With such an emergence of laws that are even in principle unattainable from laws governing the constituent particles, the notion of a fundamental law gets redefined at every stage of added complexity. In that sense, whether laws give rise to systems or systems give rise to laws becomes a chicken-and-egg situation. For if a *phenomenological* description may be derived from a more microscopic one, as, for instance, in Gor'kov's derivation of the Ginzburg-Landau theory of superconductors [1], it seems a congenial situation for both the reductionist and the phenomenologist. However, more importantly, how do our relative, a priori trusts in the two descriptions change if such a connection cannot be developed? The point we make is that the existence of such a microscopic derivation of a phenomenological law is more often the exception than the rule for emergent properties.

The property of emergence is an ubiquitous one and certainly did not arise for the first time as a methodological underpinning for condensed matter systems. In the field of ethics, Plato clearly distinguished between public and personal morality, arguing how the two are distinct issues of concern; in the

field of linguistics, Ludwig Wittgenstein, in *Philosophical Investigations*, sets up the notion of a private language only to destroy this straw man immediately afterwards, with the point being that language is a property definable only for a group of individuals; in the field of biology, collective animal behaviour has long been known to be different from that of the single member of the herd.
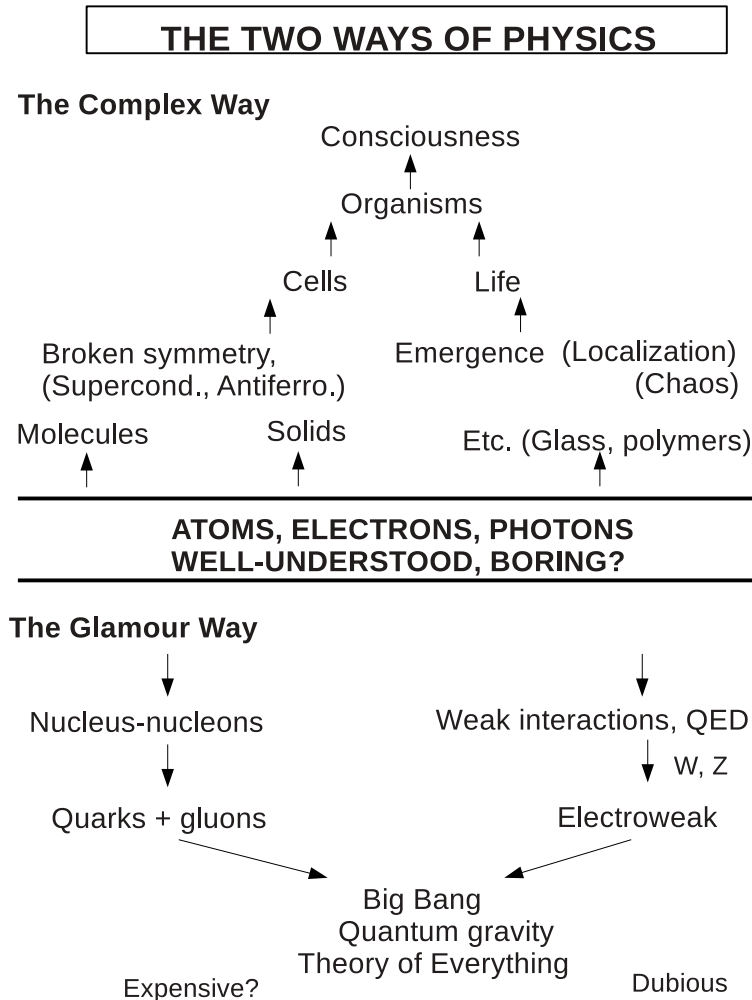
Figure 1.1: The emergent and reductionist views of physics, reproduced from Ref. [2].

We may then use, by contrast to the dualist methodology, a working definition of the nondualist approach to science as one where the system is studied as a whole, and investigate what laws operate at this level.[1] The dualist and nondualist approaches to science may be succinctly depicted with Fig. 1.1 reproduced from Ref. [2]. We begin with relatively well-understood single atoms, electrons, photons etc. (basic blocks) and go along either one of two directions: the upwards direction corresponds to the increase in system complexity whereby the systems become larger and more complex as the basic blocks are arranged in various ways; the downwards direction corresponds to splitting the basic blocks and investigating the nature of laws operating at these lower levels. We point out that although P. W.

---

[1] Although our definition of nondualism bears some semblance to the Eastern philosophical schools of nondualism where the importance of the whole is stressed, we caution that the similarities must end here and not be stretched too far.

Anderson expresses doubts as regards the reductionist approach's goal towards a theory of everything - as evidenced from the Fig. 1.1 - we merely reproduce the figure for clarifying the differences between the two ways.

In this thesis, we deal with models of condensed matter systems such as bosonic and spin models as applicable to ultra-cold gases in optical lattices (simulators of condensed matter systems) and magnetic materials. As the preceding paragraphs suggest, the practicality of considering every constituent particle's degree of freedom in the system is rendered out of the question because bottlenecks in computing power are reached even for particle numbers many orders of magnitude lesser than that in the actual system under study. In order to deal with systems having particle numbers N anywhere between $10^{12} - 10^{23}$, this number may effectively be taken as infinite; this (a) is justified because we assume that corrections to the thereby computed observables are usually of order N^{-k} with $k > 0$, and (b) simplifies calculations because finite differences and summations (which inevitably must appear in any science dealing with changes in system properties) are converted to continuous differentials and integrals, which are generally more tractable mathematically.

In chapter 2 we introduce the linked cluster expansion technique to be used in two later chapters. We recapitulate how this may be carried out using Rayleigh-Schrödinger perturbation theory and exact diagonalization of lattice models. Extrapolation and interpolation procedures for the series thus obtained are described in context: Padé approximation, Wynn extrapolations and Thiele's algorithm, all of which to be variously used to analyse the series expansion results, will be described.

In chapter 3, we investigate lattice models in the non-interacting and the Ising limits. First, we describe and use the formalism of lattice Green's functions to evaluate the density of states of a few two and three dimensional lattices in the non-interacting limit. Its relevance to electronic systems will be briefly described. Then we consider quasi-one dimensional ladders and the kagome lattice in the Ising limit at their saturation fields. The latter is relevant to the spin ice pyrochlore compound $Dy_2Ti_2O_4$ at its saturation field where the physics is dominated by decoupled kagome planes. We describe and use transfer matrix methods and Binder's algorithm to accurately evaluate the entropy at this phase point and compare with available experimental measurements.

In chapter 4, we investigate the physics of the Bose-Hubbard model on bipartite lattices at zero temperature using mean field analysis and, primarily, high order linked cluster expansions. Using the latter, we systematically include the effects of three and four body local bosonic interactions into the system. The universality of the system, with these higher body interactions, at the quantum critical transition between the Mott insulator and superfluid phases is checked. We formulate a novel scheme to renormalize the effects of these higher body interactions into the two body interactions fully. These are relevant to experiments in optical lattices in order to readily assess the effect of higher body interactions of the component ultra-cold gases.

In chapters 5 and 6, we consider the interacting hard-core Bose-Hubbard model wherein only a single boson is allowed per lattice site with repulsive interactions V between neighbours. We first consider zero temperature spin wave analysis on the bipartite square and simple cubic lattices; we compare spin wave theory results with quantum Monte Carlo simulations at very low temperature for a range of V/t values, with t being the boson hopping amplitude. The physics of and transitions between the various phases - checkerboard solid, superfluid, empty lattice - are investigated.

On a non-bipartite lattice - the kagome - we study finite temperature properties of the model in the Ising limit $V/t = \infty$ and the strongly coupled limit $V/t \gg 1$ using linked cluster expansions combined with exact diagonalization. We compute thermodynamical properties and elucidate the critical properties of the transitions between the various zero temperature phases (valence bond solid, superfluid, empty lattice); relevant critical exponents are evaluated using scaling forms of observables in the quantum critical regime at finite temperatures. Comparisons with exactly known results, where avail-

able, are made. System properties such as compressibility and specific heat at low boson densities, relevant for experiments in optical lattices where such interacting hard-core gases may be realised, are considered.

Chapter 7 will end the thesis with a summary and outlook.

Parts of this thesis have been published or are under submission:

- Strong coupling expansion for bosons on the kagome lattice. V. K. Varma and H. Monien, *Phys. Rev. B* 84, 195131 (2011).

- Lattice Green's functions for kagome, diced, and hyperkagome lattices. V. K. Varma and H. Monien, *Phys. Rev. E* 87, 032109 (2013).

- Saturation field entropies of antiferromagnetic Ising models: Ladders and the kagome lattice. V. K. Varma, *Phys. Rev. B* 88, 134421 (2013).

- Renormalization of two-body interactions due to higher-body interactions of lattice bosons. V. K. Varma and H. Monien, arXiv:1211.5664 [cond-mat.quant-gas] (2012). Submitted to *Phys. Rev. Lett.*

- Spin-wave analysis for interacting hard-core bosons on cubic lattices: a comparative study. V. K. Varma and H. Monien, arXiv:1212:5191 [cond-mat.str-el] (2012).

- Thermodynamics of hard-core bosons on the kagome lattice. V. K. Varma, H. Monien and R. R. P. Singh. *Under preparation*.

Series expansion technique

A wide range of methodologies and applications fall under the umbrella of what is meant by series expansion, dating back to about c. 1400 in the southernmost parts of India before the development of calculus in Europe. The general philosophy adopted is one of developing a series representation for a quantity that needs to be computed, and then to extract as much information from a truncated version of the series as possible. For instance, the Madhava-Leibniz infinite series for the irrational number π [3] had been initially used, among its other series representations, to evaluate π to greater accuracy. Indeed Newton used an arcsine representation of π for the purpose, only to later express how "*ashamed*" he had felt in calculating its first 15 digits "*having no other business at the time*" [4].

Within physics, series expansion techniques would prove its scope as a venerable procedure to analyse thermodynamical and critical properties of statistical models beginning in the 1960s with the work of Domb and co-workers [5]. Here too the idea is to expand a quantity or an observable M of interest (like the susceptibility of a system of spins) as a finite series in an internal or external parameter of the system (like the coupling between spins J/T at temperature T of the system). For instance,

$$M = c_0 + c_1 \tanh\left(J/T\right) + c_2 \tanh^2\left(J/T\right) + \ldots \tag{2.1}$$

There is no set rule for what the correct expansion variable corresponding to a given observable M need be; it depends on a variety of factors like the observable of interest, the initial state of the system, the strength of the couplings, and so on. For each choice of the expansion variable and the length of the series available there is a radius of convergence within which the finite expansion will remain valid, which will ultimately determine the convergence of the results and the regime of applicability of the technique. In the expansions we adopt in the rest of the work, our choice of expansion variables will be explicitly mentioned and justified.

When an exact solution of the modelled system is lacking, such an approach can provide accurate information about the critical and thermodynamical behaviour of the system. This in turn may be used to elicit knowledge about the various phases that can arise as the system parameters are varied. We refer the reader to the reviews in Refs. [5] and [6] which include descriptions of the method's historical development. In our work one particular variant known as the linked cluster expansion will be employed.

2.1 Linked cluster expansion

The method of linked cluster expansion was extensively described in our earlier work [7] and references therein, to which we refer the reader for details; the discussion that follows will collect the salient points together. Our slightly backwards exposition will adopt a top-down approach, with technical definitions of terms presented subsequent to explanations of the general methodology.

Consider the extensive property of interest P for a model on a lattice $\mathcal{L}$ containing N lattice sites. P could be the ground-state energy, the uniform susceptibility, spin-spin correlations, and so on. The key idea is to express P, per lattice site, as a sum over distinct segments or graphs g of the infinite lattice

$$\frac{P(\mathcal{L})}{N} = \sum_c L(\mathcal{L}, c) \times W(c). \tag{2.2}$$

$L(\mathcal{L}, c)$ is called the lattice constant of the cluster c and corresponds to the number of ways per lattice site that the graph (explained precisely in subsection 2.1.2) corresponding to the cluster c can be embedded in $\mathcal{L}$; a cluster c is a finite segment of the infinite lattice created by embedding the graph on the lattice. Equivalent graphs making identical contributions to the desired quantity are lumped together as being the same cluster, and their contributions are included through the lattice constant. Hence all computations need be performed only for distinct clusters. $W(c)$ is called the weight of the cluster and is a number or a power series in the appropriate variable for some particular Hamiltonian parameters such that all contributions from smaller clusters are subtracted away; this implies that a larger cluster will have for its weight a series starting at a higher power or lower decimal value than that of a smaller cluster. This weight can be calculated by inverting the above equation:

$$W(c) = P(c) - \sum_{g \subset c}' W(g). \tag{2.3}$$

Here $P(c)$ is the series expansion for the property defined on the finite cluster c, with the prime indicating that the sum runs only over proper subsets or subclusters of the cluster c. The above two are the basic defining equations of the cluster expansion. Before we move onto some general properties of the expansion, we will give a sufficiently descriptive picture regarding the lattice constant $L(\mathcal{L}, c)$ and the weight $W(c)$.

2.1.1 Lattice constants and weights

Each graph G is a set of vertices $\{v_i, i = 1, 2, ...N\}$ connected by undirected edges $\{e_j, j = 1, 2, ...M\}$; each vertex can be mapped onto a site $\mathbf{r_k}$ of the lattice $\mathcal{L}$, and each edge can be mapped onto an interaction term between sites in the Hamiltonian. The lattice constant $L(\mathcal{L}, c)$ captures the number of ways a given graph can be mapped onto a given lattice (the geometry of the problem), while the weight captures the contribution from the Hamiltonian for the given cluster (the physics of the problem). Of course, changing the degrees of freedom in the Hamiltonian (like adding next-nearest neighbour interactions) will change the graph counting, so the geometry and the physics of the problem are not completely separated.

The weight $W(c)$ can be seen to be a power series if the perturbation expansion is written as a multi-variable expansion; let the bond between $\mathbf{r_i}$ and $\mathbf{r_j}$ be associated with an interaction strength λ_{ij}. Ex-

panding the property P as a power series gives:

$$P(\mathcal{L}) = p_0 + \sum_{ij} p_{ij}\lambda_{ij} + \sum_{ij}\sum_{kl} p_{ij,kl}\lambda_{ij}\lambda_{kl} + \cdots . \tag{2.4}$$

Regrouping the terms which depend on a single λ_{ij}, we obtain the following, with the primes indicating that λ_{ij} and λ_{jk} are different:

$$P(\mathcal{L}) = p_0 + \sum_{ij}\sum_{n=1}^{\infty} a_{ij}^n \lambda_{ij}^n + {\sum_{ij,kl}}' \sum_{m=1}^{\infty}\sum_{n=1}^{\infty} b_{ij,kl}^{m,n}\lambda_{ij}^m\lambda_{kl}^n + \cdots . \tag{2.5}$$

From (2.5), we can read off the various cluster weight contributions; for example, the weights of the first 2 linear clusters are given in table 2.1:

Table 2.1: Weights of 2 linear graphs from (2.5).

Cluster	Weight $W(c)$
●─●	$W(1) = \sum_{n=1}^{\infty} a_{ij}^n \lambda_{ij}^n$
●─●─●	$W(2) = \sum_{m=1}^{\infty}\sum_{n=1}^{\infty} b_{ij,jk}^{m,n}\lambda_{ij}^m\lambda_{jk}^n$

To summarise, we first construct all required graphs, count their contributions correctly, solve the Hamiltonian for each cluster (by setting all interactions not in the cluster to zero) and add them up as in (2.2). These three steps will be explained in the next section 2.1.2 cursorily in some parts, albeit self-contained, owing to our detailed descriptions in Ref. [7].

2.1.2 Graphs and clusters

In sections 2.2 and 2.3, we will define how the weights $W(c)$ are computed for each cluster c. In this section, we describe how the lattice constants $L(\mathcal{L}, c)$ and the clusters c are generated.

Generating graphs

The partitioning of the lattice into finite segments requires careful consideration of the geometry of the lattice. This may be accomplished by a bond expansion, a site expansion or a cell expansion [6, 8, 9]. In the bond expansion, a bond between two lattice points is taken as the building block. In the site expansion the building block is a single lattice site. And in the cell expansion the building block is an appropriately defined cell for the lattice; for instance, a cell for the square lattice may be taken as a simple square, whereas for the triangular and kagome lattices a simple triangle may be taken as the cell.

The expansions are carried out to a given *order*, defined as the maximum number of sites or bonds or cells to be used in the computation. Once this is fixed, we need to generate all graphs up to that order such that each graph (a) is of lesser order than the maximum expansion order, (b) is not topologically identical to one already generated (see next paragraph) and (c) each graph may be embedded on the lattice under consideration (see next subsection). For instance, all graphs up to 3 sites or cells are shown in Fig. 2.1 for the kagome lattice; the calculation of lattice constants indicated in the figure will be taken up later.

Therefore, given the order of expansion, we need to generate all the graphs that are topologically distinct up to and including this order. A graph may be represented by its interconnectedness; topologically
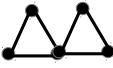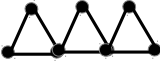
Graph	Site expansion	Cell expansion
•	1	1
•—•	2	0
•—•—•	4	0
△	2/3	2/3
△△	0	1
△△△	0	2

Figure 2.1: Graphs and lattice constants for a 3 site or 3 cell expansion on the kagome lattice; a cell is chosen to be a simple triangle. A lattice constant of 0 indicates that the graph is absent in the type of expansion considered to the given order.

equivalent graphs have the same interconnections between vertices, represented by a matrix called the adjacency matrix. For instance, consider the 3 graphs in Fig. 2.2 [6] for which the adjacency matrix is

$$A = \begin{pmatrix} 0 & 1 & 0 & 0 \\ 1 & 0 & 1 & 1 \\ 0 & 1 & 0 & 1 \\ 0 & 1 & 1 & 0 \end{pmatrix}, \qquad (2.6)$$

where an entry 1 indicates presence of a bond and 0 otherwise; the labelling is done clockwise from left. Therefore, the task of isomorphic graph identification is one of labelling the graphs in a unique way and comparing their connections to determine their topological equivalence.

This problem may be illustrated by considering the four graphs in Fig. 2.3. The graphs in Fig. 2.3a are not isomorphic as evident to the eye; however to prove that the two graphs in Fig. 2.3b are isomorphic is not a trivial task. For determining isomorphism between graphs and for choosing *canonical* representatives from among many equivalent graphs that are generated, we use algorithms from the library nauty [11]. And finally, a graph with its vertices and edges may be represented by data structures inherited from the Boost library [12].
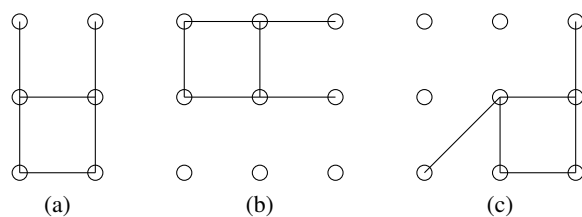
Figure 2.2: Topologically equivalent graphs all represented by the adjacency matrix (2.6). Note that the third embedding of the graph on the lattice may be disallowed by the physics of the problem but that is a different consideration.

(a)

(b)
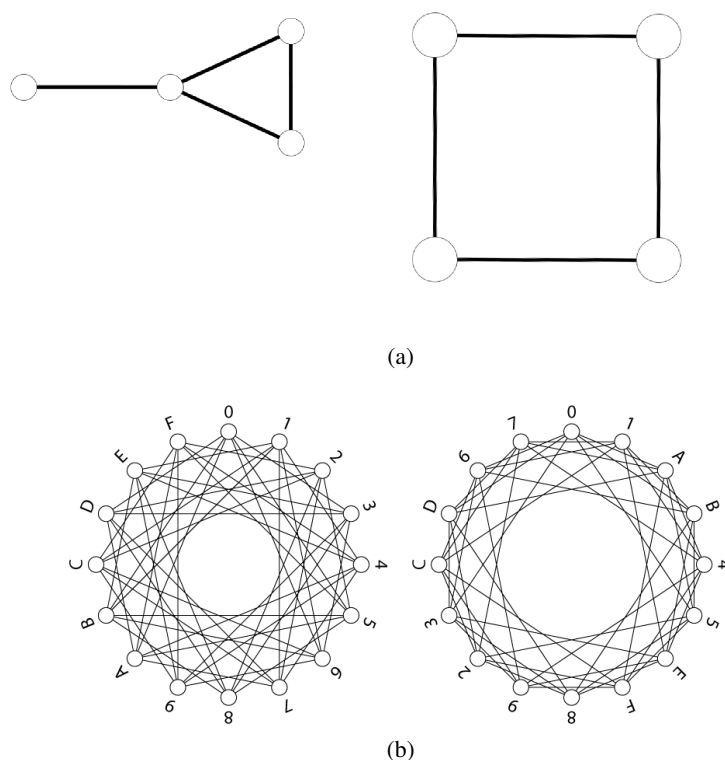
Figure 2.3: Isomorphic and not-so-morphic graphs [10].

Generating clusters

Once the graphs are properly generated and labelled up to a certain order of expansion, they need to be embedded on to the lattice under consideration. This is accomplished as follows. For each canonical graph g, map its first vertex to the (arbitrary) origin on the lattice. Then for every direction as allowed by the geometry of the lattice, map the other vertices to all possible neighbouring lattice sites. This procedure must be repeated along all directions at every vertex-embedded lattice point. That is, if a vertex cannot be embedded on the lattice (if all lattice directions are exhausted), we backtrack from this non-embedded vertex to the last embedded vertex, change direction and repeat the procedure [7].

Each such embedded graph is called a cluster c. Every such embedding contributes to the lattice constant of the cluster. However, the redundancies of translationally equivalent embeddings should be

taken care of by dividing the total number of embeddings $N_e(\mathcal{L}, c)$ by the automorphism order $a(c)$ of the cluster, which is simply the number of ways the cluster or graph may be relabelled keeping its topological nature intact. The lattice constant of the graph g on the lattice $\mathcal{L}$ is then given by

$$L(\mathcal{L}, c) = \frac{N_e(\mathcal{L}, c)}{a(c)}.$$
(2.7)

A site expansion differs from a bond expansion in that the former includes only those bond embeddings of the same cluster c such that no two vertices of c may be adjacent on the lattice without an edge connecting them [8, 9]; this is because for an n-site cluster, all possible bond connections on the lattice are to be made keeping its topological signature intact. Therefore, the site expansion will generate more embeddings with loops on the lattice thereby better capturing the lattice symmetries than a bond expansion to the same order. And for a cell based expansion, the embeddings are now evaluated with respect to the building block, which, as explained earlier, is an appropriately defined unit block the lattice.

Graph\Lattice	Square	Triangular	Kagome
•	1 (1)	1 (1)	1 (1)
•—•	2 (2)	3 (3)	2 (2)
•—•—•	6 (6)	15 (9)	6 (4)
•—•—•—•	18 (14)	69 (27)	16 (8)

Figure 2.4: Bond (site) embedding lattice constants of linear graphs on the square, triangular and kagome lattices.

We show in Fig. 2.4 the lattice constants of the linear graphs for a bond and site (in brackets) expansion on the square, triangular and kagome lattices. The embeddings required to generate the lattice constants of the 3-bond linear graph on the square and kagome lattices, and the 2-bond linear graph on the triangular lattice are shown in Appendix B.

For **excited state properties** and spatially dependent ground-state properties (like correlators), one needs to associate a quantity $\Delta(\mathbf{r})$ to each lattice point (identifiable by a vector $\mathbf{r}$). This is done by going through each embedding, and identifying all the vertex pairs in this embedding which are separated by $\mathbf{r}$. Now assuming we had already calculated $\Delta(v_1, v_2)$ for this vertex pair for the graph under question, we simply add $O(v_1, v_2)$ (divided by the automorphism order of the graph) to $\Delta(\mathbf{r})$ as one of its contributions. Then we go onto the next embedding and continue adding contributions; we repeat this for the next graph. This concludes the calculation of a dynamic lattice constant as well.

Finally for calculating the dispersion of single-particle excitations which is diagonalizable by plane waves (ignoring interactions or collisions between the quasiparticles), we perform the Fourier transform of the real-space gaps $\Delta(\mathbf{r})$ (calculated as above)

$$\epsilon(\mathbf{q}) = \sum_{\mathbf{r}} \Delta(\mathbf{r}) e^{i\mathbf{q}\cdot\mathbf{r}}. \tag{2.8}$$

For lattices with more than one site per unit cell, like the kagome for instance, embeddings for $\mathbf{r}$ dependent properties must be implemented with respect to each of the sites in the unit cell; failing which, the expansion will break symmetries of the lattice.

2.1.3 Linked cluster theorem

We present here an important theorem that enables the inclusion of only a finite number of clusters for the calculation of ground state properties, with all disconnected clusters being excluded. A cluster is said to be connected, if its sites cannot be decomposed into two non-empty groups, such that the sites of one group have no bonds connecting them to the sites of the other group.

The linked cluster theorem states that if a cluster C is composed of two disconnected clusters A and B i.e. disjoint union of non-empty subclusters, and for a property which is additive over disjoint clusters, then this property has zero weight for C:

$$P_C = P_A + P_B \Rightarrow W_{[P]}(C) = 0. \tag{2.9}$$

The Hamiltonian $\mathcal{H}_C$ on the full space can be written as a sum of subcluster Hamiltonians $\mathcal{H}_{A,B}$ acting on direct product spaces:

$$\mathcal{H}_C = \mathcal{H}_A \otimes \mathcal{I}_B + \mathcal{I}_A \otimes \mathcal{H}_B. \tag{2.10}$$

The two above terms commute (directly implied by the fact that there is no interaction term between $\mathcal{H}_A$ and $\mathcal{H}_B$ above), meaning that for any ground-state property calculated for C, only one of the above terms will contribute. But this term will be precisely subtracted away during subcluster subtraction. This may be seen as

$$
\begin{aligned}
W_{[P]}(C) &= P_C - \sum_{C' \subset C} W_{[P]}(C') \\
&= P_A - \sum_{C' \subseteq A} W_{[P]}(C') + P_B - \sum_{C' \subseteq B} W_{[P]}(C') \\
&= 0.
\end{aligned}
\tag{2.11}
$$

Thus the ground-state energy and other ground-state properties which are additive over disjoint unions will have a connected or linked cluster expansion. That excited state properties also have a connected cluster expansion will be shown in section 2.2.2.

2.2 Perturbation theory

2.2.1 Ground state energy

The calculation of $P(c)$ for finite clusters in (2.3) will be discussed now; this will be the next essential step required to calculate $P(\mathcal{L})$ for the infinite lattice. To this end we require Rayleigh-Schrödinger perturbation theory [13], which requires that exact eigenstates $|k\rangle$ and eigenvalues e_k of the unperturbed

Hamiltonian must be obtainable:

$$\mathcal{H}_0|k\rangle = e_k|k\rangle. \tag{2.12}$$

The cluster Hamiltonian has the same form as the full lattice Hamiltonian, with the restriction that for a finite cluster all the operators must act only within the cluster; this is indeed possible if the $\mathcal{H}$'s can be split up into local operators, with the assumption henceforth being that the interaction strength between all the bonds are the same:

$$\mathcal{H} = \mathcal{H}_0 + \lambda\mathcal{H}_1. \tag{2.13}$$

The cluster ground-state energy and the wavefunction are expanded in powers of λ as

$$E = \sum_{i \geq 0} E_i \lambda^i, \tag{2.14}$$

$$|\psi\rangle = \sum_{i \geq 0} |\psi\rangle_i \lambda^i, \tag{2.15}$$

and inserting these into the Schrödinger equation $\mathcal{H}|\psi\rangle = E|\psi\rangle$, one gets the following recurrence relations

$$E_i = \langle 0|\mathcal{H}_1|\psi_{i-1}\rangle \tag{2.16}$$

and

$$\langle k|\psi_i\rangle = \frac{1}{e_0 - e_k}[\langle k|\mathcal{H}_1|\psi_{i-1}\rangle - \sum_{i'=1}^{i-1} E_{i'}\langle k|\psi_{i-i'}\rangle], \tag{2.17}$$

with $|k\rangle \neq |0\rangle$ the ground state. Implicit in the derivation above is the use of an arbitrary normalization condition that essentially determines the starting initial conditions:

$$\langle 0|\psi_i\rangle = \delta_{i,0}, \tag{2.18}$$

where $\delta_{i,0}$ is the Kronecker delta function.

2.2.2 Excited states

At first glance it seems that there can be no linked cluster expansions for excited state properties because these are not extensive and therefore not additive over disconnected subclusters. However, after a second glance, it was shown [14] that one can indeed identify a quantity that describes excited states and which is additive over disjoint unions of clusters.

The basic approach is to isolate the degrees of freedom in which we are interested (e.g. single particle energy gaps) from the rest of the system using a similarity transformation which is a common enough technique (e.g. Foldy-Wouthuysen transformation of the Dirac equation). These transformations are applied to each cluster Hamiltonian, resulting in an effective Hamiltonian for each cluster that has essentially two separated subspaces: one containing all the degenerate single-particle excitations while the other containing the rest of the physics of the system. The separation ensures that the full matrix is block diagonalized and that there are no matrix elements between the block representing the single-particle excitations and the block representing the rest of the matrix. The required transformation is

$$S^{-1}\mathcal{H}S = \begin{pmatrix} \boxed{\mathcal{H}^{\text{eff}}} & 0 \\ 0 & \boxed{\text{Higher excitations}} \end{pmatrix} \tag{2.19}$$

Thus each cluster will have associated with it a single particle manifold (an effective Hamiltonian matrix), and Rayleigh-Schrödinger perturbation theory must now be applied to these matrices rather than simple numbers as before in the non-degenerate case. As an additional benefit, this will also lead to a considerable reduction in computational complexity because we now restrict our calculations only to a single-particle manifold, whose Hilbert space can be considerably smaller than that for the full system. That is we can now work with matrices with subspaces many orders of magnitudes smaller than the initial full Hilbert space.

The question that arises is how is $\mathcal{H}^{\text{eff}}$ for the full system C, formed by (our quintessential example) the union of 2 disconnected clusters A and B, related to the initial $\mathcal{H}^{\text{eff}}$? The answer turns out in many cases to be

$$\mathcal{H}^{\text{eff}}_{A+B} = (\mathcal{H}^{\text{eff}}_A + E_B \mathcal{I}_A) \oplus (\mathcal{H}^{\text{eff}}_B + E_A \mathcal{I}_B). \tag{2.20}$$

Since the ground-state energies are additive over disconnected clusters, this can be rewritten as

$$(\mathcal{H}^{\text{eff}} - E\mathcal{I})_C = (\mathcal{H}^{\text{eff}} - E\mathcal{I})_A \oplus (\mathcal{H}^{\text{eff}} - E\mathcal{I})_B. \tag{2.21}$$

Thus we have our quantity that is manifestly additive over disconnected clusters.

Let us assume that we have N sites in the cluster C and that the excitation is labelled by the site on which it resides. The idea now is to construct the first N columns of the similarity transformation matrix S order by order, which we will consider as a set of state vectors $|\psi^{(1)}\rangle \cdots |\psi^{(N)}\rangle$. With the same recipe as before, we perform the expansion of the state vectors and the $\mathcal{H}^{\text{eff}}$ (which is also constructed order by order, the components of which will finally give the dispersion relations of the excitations):

$$|\psi^{(l)}\rangle = \sum_{k \geq 0} \lambda^k |\psi^{(l)}_k\rangle, \tag{2.22}$$

$$\mathcal{H}^{\text{eff}} = \sum_{k \geq 0} \lambda^k \mathcal{H}^{\text{eff}}_k. \tag{2.23}$$

After some algebra, collecting like powers of λ in $\mathcal{H}S = S\mathcal{H}^{\text{eff}}$, and using a generalised form of the normalization condition encountered in (2.18),

$$\langle l|\psi^{(l)}_k\rangle = \delta_{k,0}\delta_{l,l'}. \tag{2.24}$$

we obtain the following recursion relations

$$\langle l'|\mathcal{H}^{\text{eff}}_k|l\rangle = \langle l'|\mathcal{H}_1|\psi^{(l)}_{k-1}\rangle, \tag{2.25}$$

$$\langle m|\psi^{(l)}_k\rangle = \frac{1}{e_0 - e_k}[\langle m|\mathcal{H}_1|\psi^{(l)}_{k-1}\rangle - \sum_{k'=1}^{k-1}\sum_{l'=1}^{N}\langle m|\psi^{(l')}_{k'}\rangle\langle l'|\mathcal{H}^{\text{eff}}_{k-k'}|l\rangle]. \tag{2.26}$$

where the states $|m\rangle$ are eigenstates of $\mathcal{H}_0$ not in the single-particle manifold.

The only modification required here (from the ground-state properties) would be that we now require a matrix of energies and a number of state vectors to calculate (the number depending on the size of the cluster in consideration).

Once we have constructed these effective Hamiltonians and state vectors for each cluster, we need to associate them with the physical lattice. This was explained in the paragraphs preceding and leading up to (2.8).

Momentum distribution

A quantity of interest in analysing the phases and behaviour of a many-body quantum mechanical system is the momentum distribution or the single-particle density matrix. For field operators $b_{\mathbf{r}}, b_{\mathbf{r}}^{\dagger}$ at coordinate labelled $\mathbf{r}$, the momentum distribution is defined as

$$n(\mathbf{k}) = \sum_{\mathbf{r}} \exp{(i\mathbf{k}.\mathbf{r})} \langle b_{\mathbf{r}}^{\dagger} b_{\mathbf{0}} \rangle, \qquad (2.27)$$

where the sum runs over all available coordinates $\mathbf{r}$, evaluated at a lattice momentum $\mathbf{k}$. The calculation of the expectation value $\langle b_{\mathbf{r}}^{\dagger} b_{\mathbf{0}} \rangle$ proceeds as outlined towards the end of section 2.1.2.

The structure of $n(\mathbf{k})$ across the Brillouin zone in lattice models can often give useful information about the underlying physics of the system. For instance, for free electrons $n(\mathbf{k}) = f(\mathbf{k})$ is just given by the Fermi-Dirac statistics; as very strong interactions are introduced one may analyse the development or otherwise of a Fermi surface as seen for the electronic $t - J$ model on the square lattice [15]. Similarly for hard-core bosons, in addition to discerning the development of quasi off-diagonal long range order in one dimensional systems as indicated by a diverging momentum distribution at $\mathbf{k} = \mathbf{0}$, the properties and transitions of various phases like the charge density waves and Luttinger liquid may be studied [16].

2.3 Exact diagonalization

The weights $W(c)$ of the Hamiltonian for the cluster c may be evaluated by any technique that allows physical observables to be computed on finite segments of the lattice. We employ exact diagonalization as an alternative to the perturbation theory presented in section 2.2 for calculation of finite temperature properties of lattice models in chapter 6; perturbation theory will be used in chapter 4 for zero temperature properties of lattice models. The advantage of using exact diagonalization within series expansion, termed numerical linked cluster expansion [9], is that gapless states may also be handled which perturbation theory cannot handle as seen from the division in (2.17) and (2.26). However within a perturbative analysis, there is more analytic structure that may be gauged from the expansions.

As before, the basis of allowed states is constructed for every given cluster c. The Hamiltonian matrix $H(c)$ is constructed and its eigenvalues are found using the Lapack [17] and Boost numeric bindings libraries [18]. The Lapack function `sytrd` reduces the symmetric matrix $H \equiv H(c)$ to a tridiagonal form T using the similarity transformation

$$H = QTQ^{-1}, \qquad (2.28)$$

where Q is an orthogonal matrix. The similarity transformation (2.28) leaves the eigenvalues of the matrix H unchanged as readily seen in (2.29) by computing the characteristic polynomial.

$$
\begin{aligned}
|H - \lambda \mathbb{1}| &= |Q(T - \lambda \mathbb{1})Q^{-1}| \\
&= |Q||T - \lambda \mathbb{1}||Q^{-1}| \\
&= |T - \lambda \mathbb{1}|, \qquad (2.29)
\end{aligned}
$$

where $\mathbb{1}$ denotes the identity matrix. Transformation to the tridiagonal form generally reduces the computational complexity for eigenvalue computation from $O(m^4)$ to $O(m^3)$ (or better for symmetric matrices), where m is the dimension of the matrix [19]. The Lapack function `syev` may now be used to generate the eigenvalues and eigenvectors.

The eigenvectors will be transformed by the orthogonal matrix Q^{-1} after the transformation (2.28).

For if $\vec{v}$ is an eigenvector of H with an eigenvalue λ, then

$$\left(QTQ^{-1}\right)\vec{v} = \lambda\vec{v}, \tag{2.30}$$

which shows that the corresponding eigenvector of T is $Q^{-1}\vec{v}$.

Therefore once we have computed the eigenvalues and eigenvectors of the cluster c, the weight $W(c)$ corresponding to the observable of interest may in turn be evaluated. For instance, **r** dependent properties on the lattice will require both the eigenvectors and eigenvalues whereas observables diagonal in the original basis of the Hamiltonian matrix $H(c)$ will require only knowledge of the eigenvalues.

2.4 Extrapolation techniques

Oftentimes the measured or measurable data of a system is limited and there is the pressing need to conjecture the - or a - functional dependence of the input to the output in our set. The obtained functional form, almost always an approximation, aids in further analysis by effecting either an interpolation or extrapolation of the data. One main approach we adopt towards this end is rational approximation where the functional relation of our data set is approximated by a rational function

$$\phi^{(M,N)}(x) = \frac{P^{(M)}(x)}{Q^{(N)}(x)} = \frac{a_0 + a_1 x + \cdots + a_M x^M}{b_0 + b_1 x + \cdots + b_N x^N}, \tag{2.31}$$

for integer coefficients a_i, b_i and some order of the polynomials M, N. This can prove a powerful approximation because the behaviour of a polynomial of infinite degree can, in effect, be captured with rational functions. We utilise three such methods: the Padé approximant, Thiele's algorithm and Wynn's algorithm.

2.4.1 Padé approximants

Padé approximants (PA) were first introduced into physics in 1961 [20] in the form of, what is now known as, the Baker-Gammel-Wills conjecture regarding the behaviour of meromorphic functions (a holomorphic function with isolated singularities). In the same year the approximation was utilised in the theory of critical phenomenon [21] to calculate the magnetic susceptibility of the Ising model for the simple planar and cubic lattices. We describe briefly the theory and applicability of the method of Padé approximation [8, 22].

Padé approximation is a method of analytically continuing a finite series beyond its radius of convergence and up to a physical singularity, or beyond. It should be mentioned that there are other methods for asymptotically analysing a series [5], but the main advantage of this method is that multiple singularities anywhere in the complex plane can be analysed simultaneously.

Theory

A PA is a representation of the first N terms of a power series as a ratio of two polynomials. Thus,

$$f(x) = \sum_{n=0}^{N} a_n x^n = P_L(x)/Q_M(x), \tag{2.32}$$

where $P_L(x)$, $Q_M(x)$ are polynomials of degree L, M and $L + M \leq N$. This is denoted as the $\mathrm{PA}_{[L,M]}$. With varying values of L and M, a Padé table can thereby be constructed. A particularly instructive and
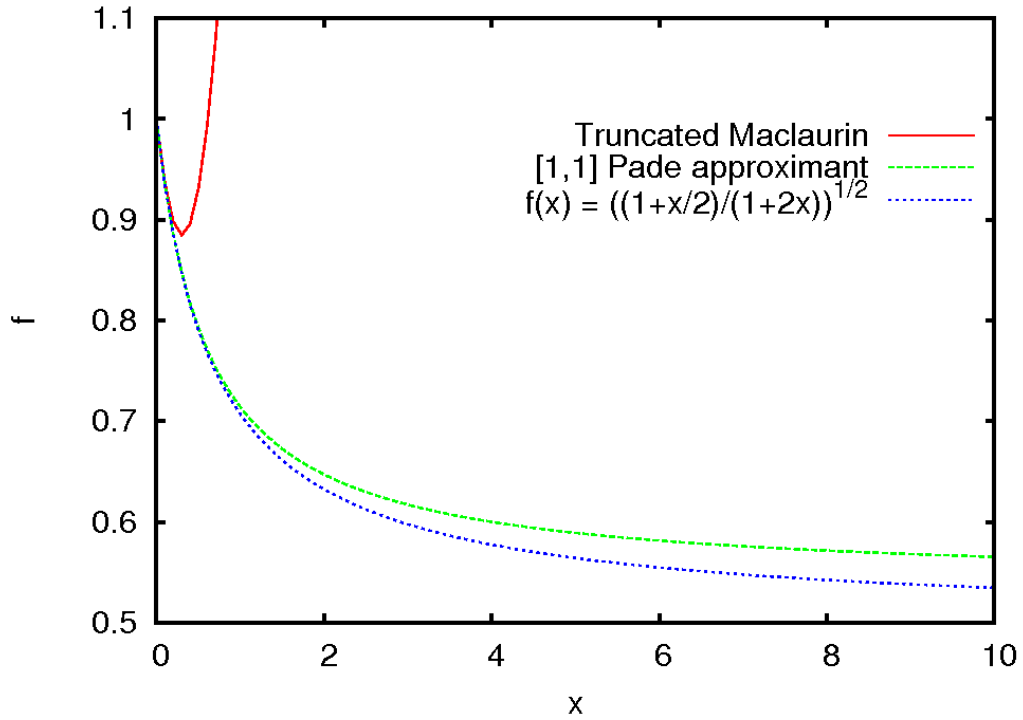
Figure 2.5: Asymptotic analysis of Maclaurin series of function $f(z)$ in (2.33).

simple example picked up from the literature [22] will be illustrated here. Consider the function

$$f(z) = \sqrt{\frac{1 + 0.5z}{1 + 2z}} \tag{2.33}$$

which is defined by its Taylor-Maclaurin series

$$f(z) = 1 - \frac{3}{4}z + \frac{39}{32}z^2 + \cdots . \tag{2.34}$$

In order to evaluate the function at $z = \infty$, so as to give the value $f(\infty) = 1/2$, a direct evaluation of the finite series is not possible, whereas the $PA_{[1,1]}$,

$$PA_{[1,1]} = \frac{1 + \frac{7}{8}z}{1 + \frac{13}{8}z} \tag{2.35}$$

which uses just 2 terms, is accurate to 8% at $z = \infty$, and gives 0.54. The two approaches are plotted against the real function in the Fig. 2.5. In the rest, we utilise Mathematica [23] for calculating Padé approximants.

DLogPadé

A PA can represent functions with simple poles exactly. Thus in the study of critical phenomena it is usual to take the logarithmic derivative of the series, which converts an algebraic singularity into a

simple pole. For example, if $f(x) = A(x)(x_c - x)^{-\theta}$ then

$$D\log f(x) \equiv \frac{f'(x)}{f(x)} = \frac{A'(x)}{A(x)} + \frac{\theta}{x_c - x}. \tag{2.36}$$

Hence, by taking a PA of the above, the positions of the singular points can be estimated from the roots of the denominator polynomial $Q_M(x)$, and exponent θ from the corresponding residues.

2.4.2 Thiele's algorithm

Thiele's algorithm is used to interpolate a given set of support points (x_i, f_i) by a rational function of the form (2.31). As with the construction of Padé approximants, the maximal degree of the numerator and denominator in Thiele's rational function approximation are determined by the number of data points available. We closely follow the discussion in Ref. [24] in this subsection.

Theory

Rational expressions are constructed along the main diagonal of the (M, N)-plane in Thiele's algorithm. The support points (x_i, f_i) are used to generate *inverse differences* ϕ depicted notationally in the table 2.2.

Table 2.2: Generic flow of the Thiele's algorithm in construction of inverse differences from the input data set.

x_i	f_i	Inverse differences		
x_0	f_0			
x_1	f_1	$\phi(x_0, x_1)$		
x_2	f_2	$\phi(x_0, x_2)$	$\phi(x_0, x_1, x_2)$	
x_3	f_3	$\phi(x_0, x_2)$	$\phi(x_0, x_1, x_2)$	$\phi(x_0, x_1, x_2, x_3)$
$\vdots$	$\vdots$	$\vdots$		

The inverse differences are generated by the following recursion relations

$$\phi(x_i, x_j) = \frac{x_i - x_j}{f_i - f_j},$$

$$\phi(x_i, \ldots, x_l, x_m, x_n) = \frac{x_m - x_n}{\phi(x_i, \ldots, x_l, x_m) - \phi(x_i, \ldots, x_l, x_n)}. \tag{2.37}$$

Then Thiele's rational approximation for the $2n + 1$ data points is given by the continued fraction [24]

$$\phi^{(n,n)}(x) = f_0 + \cfrac{x - x_0}{\phi(x_0, x_1) + \cfrac{x - x_1}{\phi(x_0, x_1, x_2) + \ddots + \cfrac{x - x_{2n-1}}{\phi(x_0, x_1, \ldots, 2n)}}}. \tag{2.38}$$

In the event that one or more of the inverse differences in table 2.2 are equal, then the continued fraction expansion must terminate at this column lest the succeeding inverse differences become undefined; this abrupt termination usually indicates that the obtained approximation is in fact an exact functional representation of the input data. For instance, consider the (x_i, f_i) data set in table 2.3 and the inverse differences generated by (2.37). Using $i = 0, 1, 2$, the rational approximation obtained from (2.38)
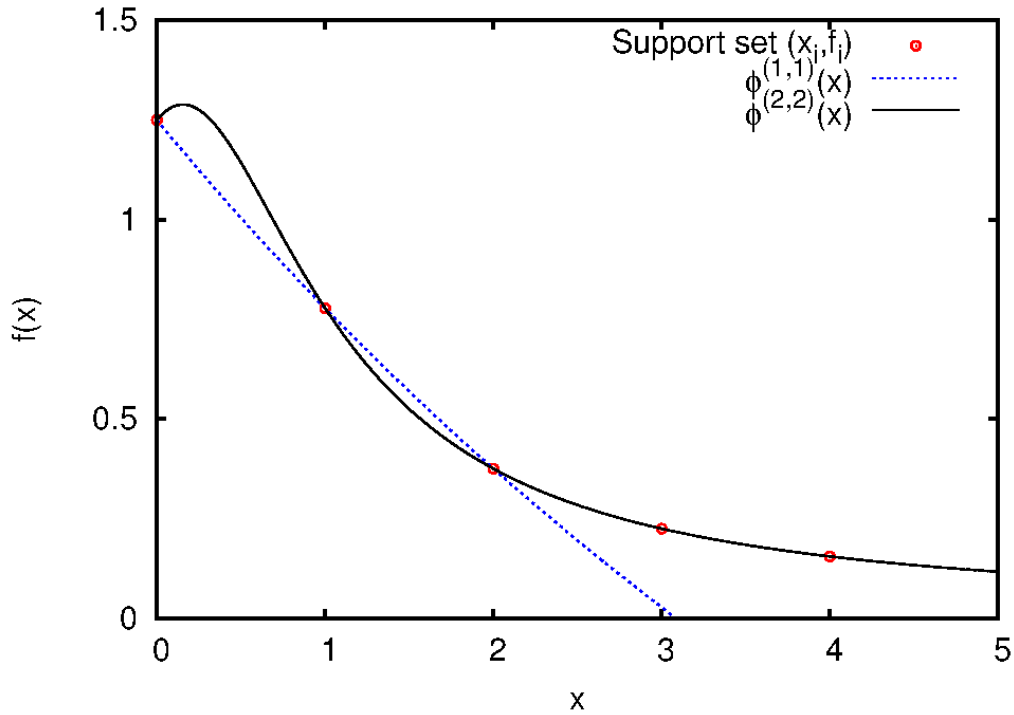
Figure 2.6: Thiele's rational function approximation of the five data points in table 2.3.

Table 2.3: Example data set illustrating Thiele's algorithm.

x_i	f_i	Inverse differences			
0	5/4				
1	7/9	$-36/17$			
2	3/8	$-16/7$	$-119/20$		
3	11/49	$-196/67$	$-1139/460$	230/799	
4	13/84	$-84/23$	$-391/200$	400/799	47/10

is $\phi^{(1,1)}(x) = \dfrac{145 - 47x}{2(178 - 43x)}$. Whereas using all the above data points, we indeed recover the exact and original generating function $\phi^{(2,2)}(x) = f(x) = \dfrac{2x + 5}{5x^2 + 4}$; note that the sum of the numerator and denominator degrees is less than the number of data points, indicating the exactness of $\phi^{(2,2)}(x)$. The two approximations are plotted for comparison in Fig. 2.6 along with the original 5 data points.

2.4.3 Wynn's algorithm

Another typical extrapolation problem may be stated as following: given the finite sequence

$$S = s_0, s_1, s_2, \ldots s_{n-1}, \tag{2.39}$$

find the value $\lim_{n\to\infty} s_n$, where each of the elements is a partial sum

$$s_k = \sum_{i=1}^{k} a_i \tag{2.40}$$

of a series. Such a situation arises in our treatment of hard-core bosons on the kagome lattice in chapter 6 within the context of numerical linked cluster expansions. The general methodology [25] for treating sequences such as (2.39) is to construct a table of values from the original sequence, represented below as a matrix,

$$S^{\text{ext.}} = \begin{pmatrix} s_{-1}^{(0)} & s_{-1}^{(1)} & \cdots & s_{-1}^{(n-1)} \\ s_0^{(0)} & s_0^{(1)} & \cdots & s_0^{(n-1)} \\ s_1^{(0)} & s_1^{(1)} & \cdots & \\ \vdots & \vdots & & \\ s_k^{(0)} & & & \end{pmatrix}, \tag{2.41}$$

with the initialisation that the second row $S^{\text{ext.}}(1,\ldots)$ be assigned to the sequence S of (2.39)

$$S^{\text{ext.}}(1,\ldots) = S. \tag{2.42}$$

At each iteration, the procedure moves down to the next row and the number of available terms in the extrapolated sequence reduce. In this section we describe a versatile non-linear extrapolation technique known as Wynn's algorithm [25, 26], and two of its variants that speed up the calculations while simultaneously avoiding round-off errors [27].

Epsilon algorithm

In the epsilon (ϵ) algorithm, the extrapolated elements $s_k^{(n)}$ in (2.41) are given by the simple recursion formula

$$s_k^{(n)} = s_{k-2}^{(n+1)} + \frac{1}{s_{k-1}^{(n+1)} - s_k^{(n)}}, \tag{2.43}$$

with the initialization (2.42) and $s_{-1}^{(n)} = 0$ for all n. The small differences in the denominator of (2.43) give the procedure its name. Wynn showed that the numbers with even subscripts $s_{k=2m}^{(n)}$ will provide convergence of the desired series [26]. Therefore two terms are lost after every cycle of two iterations.

To illustrate the method, we consider a slightly pathological series [25] with

$$s_k = \sum_{n=0}^{k} (-1)^n n!. \tag{2.44}$$

This sequence has an anti-limit studied extensively by Euler who presented its value using at least five different methods lest the reader be left incredulous. s_k in (2.44) are the coefficients of the asymptotic series for the function

$$f(z) = \int_z^{\infty} \frac{e^{z-x}}{x} dx, \tag{2.45}$$

in negative powers of x, evaluated at $z = 1$ [25]. (2.45) may be numerically calculated at $z = 1$ to obtain the value

$$f(1) = 0.59634736\ldots. \tag{2.46}$$

Using just the first 8 terms of the sequence in (2.44), we obtain the Wynn extrapolated correct within 1% of the value $f(1)$ in (2.46); this may be improved to 0.05% by including 8 more terms in the original series.

This may be seen by explicitly writing down the extrapolation matrix (2.41) corresponding to the sequence (2.44) as

$$
S^{\text{ext.}} = \begin{pmatrix}
0 & 0 & 0 & 0 & 0 & 0 & 0 & 0 \\
1 & 0 & 2 & -4 & 20 & -100 & 620 & -4420 \\
-1 & 0.5 & -0.16667 & 0.04167 & -0.00833 & 0.00139 & -0.00019 & \\
0.66667 & 0.5 & 0.8 & 0 & 2.85714 & -10 & & \\
-5.5 & 3.16667 & -1.20833 & 0.34167 & -0.07639 & & & \\
0.61539 & 0.57143 & 0.64516 & 0.46512 & & & & \\
-19.5833 & 12.3542 & -5.2125 & & & & & \\
0.60274 & 0.60274 & & & & & &
\end{pmatrix}.
$$

(2.47)

As mentioned earlier, we see that every second row corresponds to the extrapolated limit; the odd row numbers are divergent series and merely constitute intermediate steps.

Bordering techniques

In the recursion relation for the ϵ algorithm (2.43) there occurs in the denominator subtraction of almost equal extrapolated quantities. To do away with this potential source of numerical instability, Brezinski formulated two methods [27] to arrive at the extrapolated values s_{2k}^m via the introduction of several auxiliary quantities d_k, λ_k, σ_k as opposed to the simple recursion relation in (2.43). The precise definitions of these quantities are left to the Appendix C where we closely follow the workings in Ref. [27]. The even subscripted $s_{2k}^{(n)}$ are computed without going through the odd subscripted elements and are given by

$$
\frac{1}{s_{2k+2}^{(n)}} = \frac{1}{s_{2k+2}^{(n)}} + \frac{d_k^2}{\lambda_{k+1}},
$$

$$
s_{2k}^{(n)} = \frac{\sigma_k}{d_k}.
$$

(2.48)

Line 1 in (2.48) is termed the first bordering method and line 2 is termed the second bordering method. We have considered the example $s_k = s + \dfrac{1}{k+1}$ in Brezinski's paper [27] and reproduced the table to at least 10 decimal places up to $2k = 12$.

2.5 Conclusions

In this chapter we described the machinery of linked cluster expansions using Rayleigh-Schrödinger perturbation theory and exact diagonalization. We discussed in moderate detail how the method is suitable for investigating the physics of lattice models. Furthermore, to accurately understand the phases and transitions in the model, the behaviour of the full series - with its infinite number of terms - must be captured from the finite number of terms obtainable from the method. This constitutes the need for extrapolation and rational approximation of the finite series, which we exemplified by three such techniques.

Lattice models: potential and kinetic energy

3.1 General considerations

Physical systems come under a variety of internal and external influences which determine its thermo-dynamic behaviour, the time evolution of an initial state and so on. In analysing the physical character of these systems, these influences are usually separated into kinetic energy terms (isolated motion of the body) and potential energy terms (position of the body with respect to the environment or other bodies); it is generally the case that the two sets of terms do not favour a single type of state for the system as a whole. For instance, while the kinetic motion prefers a more disordered phase in terms of the constituent particles' locations, the potential energy tends to freeze out the system in its most stable equilibrium position. This separation is one of convenience, however, because external potentials can also give rise to motion of the body, e.g. the dynamics of a pair of gravitating bodies; on the other hand, the kinetic motion of a single body can also influence the state of another body e.g. the creation of a magnetic field by the motion of a charged particle which in turn influences the motion of another charged particle. We may further augment the contribution of kinetic energy to the system through other forms of energy e.g. by increasing the temperature (adding heat energy); this temperature contribution to kinetic energy is not, however, necessary within a quantum mechanical description as we shall see in chapters 4, 5, and 6.

Nevertheless, the separation between these two energy types affords much pragmatic value in explaining a variety of physical systems. That is to say, at the level of particles or anything with definite characterizable properties obeying certain universal laws, we may effect a phenomenological separation of energy types and their scales. However for a given set of internal and external conditions, the system will end up in a state that best satisfies both energy contributions, often at some compromise to each; in other words, for an actual material at given conditions, the two energy scales will ultimately be linked at a microscopic level.

The competition between kinetic and potential energy influences on the system's behaviour may be seen heuristically via the argument that the Helmholtz free energy given by [28]

$$A = U - TS, \tag{3.1}$$

where U is the internal energy, T the temperature, and S the entropy of the system, be minimized. While the internal energy is generally minimized for an ordered state, the entropy term is generally maximized for disordered states. This fundamental competition may as well be exacerbated by struc-

tural factors such as (a) the system's boundaries i.e. where one chooses to delineate the system from the environment, and (b) its internal arrangement of constituent particles that serves to determine its response to the external environment. These geometric considerations play a major deciding role in the wide range of substances produced by the condensed matter, materials science, optical physics, and engineering communities, where systems with anywhere from 10^{12} to 10^{23} particles per cubic centimetre are investigated, manipulated and created.

In the magnetic and ultra-cold models of systems that we consider in this thesis, we assume that the kinetic and potential energy contributions to the constituent particles of the system arise from influences that may be separated in energy scales and causation agents, and can, oftentimes, even be individually controlled (as in ultra-cold gases in optical lattices). We will exemplify this point for particular models and system geometries to illustrate how interesting physics may arise even with the action of just the kinetic or potential energy terms. In the remaining, our focus will be on lattice models of physical systems at low energies i.e. low compared to the energies required for complete dissociation of the system. [1]

3.2 Non-interacting lattice systems

A topical example of a material favourably amenable to a non-interacting description and one that has received much attention in the past years is graphene [29]. This is a recently manufactured material, synthesized from naturally occurring graphite, consisting of a two dimensional layer of carbon atoms, of atomic thickness arranged in a hexagonal pattern. The electronic correlations are very weak and the hopping energy of electrons is about 2.8 eV. Within the tight-binding (non-interacting) description (3.2), the density of states of graphene may be calculated and is shown in Fig. 3.1a; the upper plots show the electronic density of states (defined precisely in (3.4)) with the inclusion of a small nearest neighbour hopping amplitude while the lower plots show the same with only nearest neighbour hopping of electrons. In the latter, particle-hole symmetry is clearly visible about the Fermi energy $\omega = 0$; this is absent in the lattice models we study and so half-filling need not be the stable density of the tight-binding model in (3.2) in the ground state. Moreover, because of the presence of touching Dirac cones in the two electronic dispersion bands of graphene in the tight-binding description, relativistic field theory of electrons predicts a square root dependence between the charge carrier concentration and the cyclotron mass, which is nicely borne out between experimental data and the theoretical results as shown in Fig. 3.1b [29]. Thus, among other experimental justifications, a non-interacting description is an agreeable description for many electronic properties of graphene.

Indeed there exist other exotic materials like carbon nanotubes that are synthesized from sheets of carbon; due to their structural versatility, tensile strength and diverse electronic properties, they continue to find applications in a vast number of fields such as aerospace engineering, electronics industry, and others. Here too, a non-interacting model is used to describe its unique quantum mechanical properties [30]. Moreover, the addition of small spin-orbit coupling to some of the tight-binding models we study have been shown to support topological insulators e.g. on the kagome lattice [31]. [2]

In this section we consider non-interacting particles on a lattice system describable by the Hamiltonian

$$\mathcal{H} = \frac{1}{2} \sum_{<i,j>} \left(\hat{a}_i^\dagger a_j + \hat{a}_j^\dagger a_i \right), \qquad (3.2)$$

---

[1] Needless to say, we do not simply mean a phase transition by this.

[2] Although a Japanese word, we do not italicize, accent or capitalize the word "kagome" due to its wide usage.
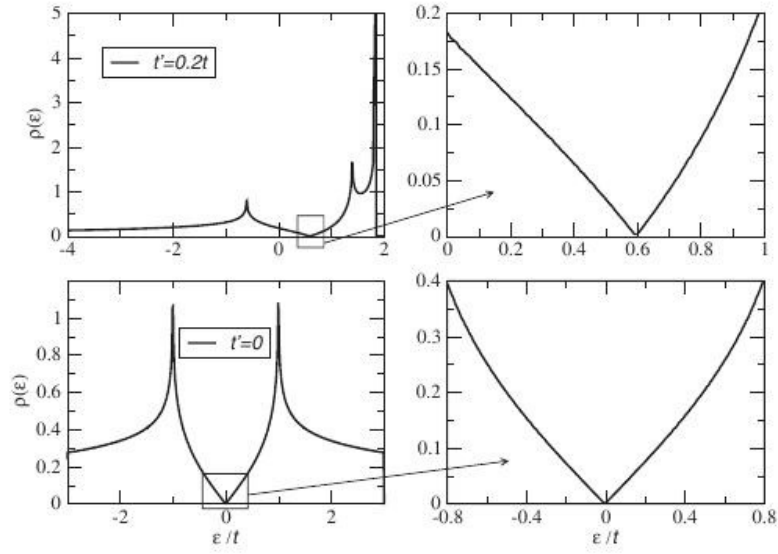
(a)
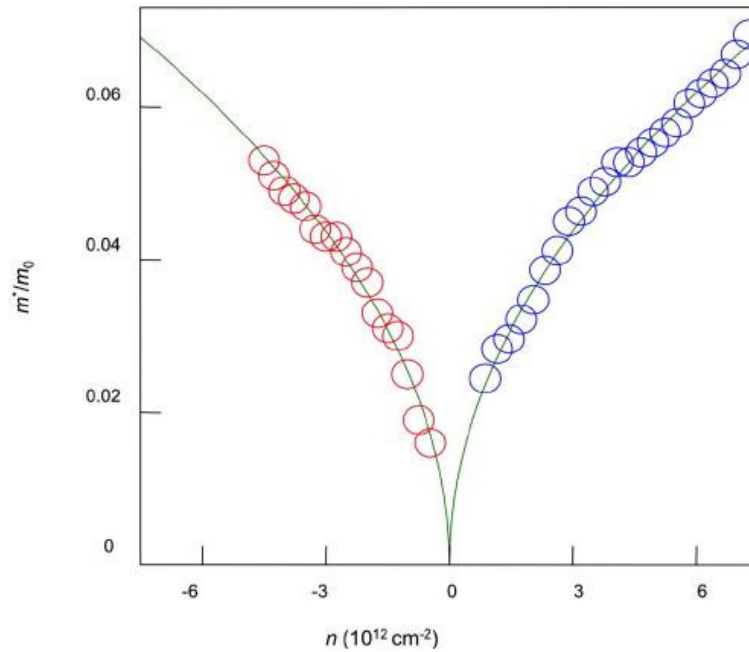
(b)

Figure 3.1: (a) Density of electronic states for next-nearest-neighbour hopping ($t' \neq 0$) and nearest-neighbour hopping ($t' = 0$) of electrons on a graphene sheet. Clearly there is a particle hole symmetry about the Fermi energy, which is absent from the lattices we investigate. (b) Cyclotron mass of electrons (right) and holes (left) as a function of charge carrier concentration. A massless Dirac-like dispersion of the electrons requires a square root dependence which is borne out between experimental data (circles) and a tight-binding description (line). Both figures taken from Ref. [29].

where the field operators $\hat{a}, \hat{a}^\dagger$ on neighbouring sites i, j may have any particle statistics such as the Fermi-Dirac or Bose-Einstein statistics given, respectively, by

$$f_{\text{FD}}(\epsilon_k, \mu, T) = \frac{1}{1 + e^{(\epsilon_k - \mu)/T}},$$

$$f_{\text{BE}}(\epsilon_k, \mu, T) = \frac{1}{-1 + e^{(\epsilon_k - \mu)/T}}, \tag{3.3}$$

where k labels the state with dispersion ϵ_k, μ is the chemical potential, temperature is T in units of the Boltzmann constant.

The density of states $\rho(\epsilon)$ of a system is a pivotal quantity that describes its energy ϵ distribution; the defining equation is

$$\rho(\epsilon) = \int \delta\left(\epsilon - \epsilon_{\vec{k}}\right) d\vec{k}, \tag{3.4}$$

for any energy ϵ associated with the system's state labelled by $\vec{k}$, and $\delta(x)$ is the Dirac delta function. For one-particle states (non-interacting limit), this may, oftentimes, be calculated exactly. Consider, in three dimensional free space, the case of (quantum) particles of mass m and wave-vector $\vec{k}$ with kinetic energy $\epsilon_{\vec{k}} = \hbar^2 |\vec{k}|^2 / 2m$, where $\hbar$ is the reduced Planck's constant. Then using this energy in (3.4), we obtain $\rho(\epsilon) \propto \sqrt{\epsilon}$. But upon the introduction of a lattice and the concomitant breaking of Galilean invariance, the functional form of the density of states will change drastically depending on the actual reduced symmetry - reduced with respect to the original SO(3) symmetry - of the lattice.

We illustrate this for a simple one dimensional chain described by (3.2), emphasizing that for most of what follows the actual statistics of the particles plays no role. The dispersion of the above is given by $\epsilon(k) = \cos(k)$ within the first Brillouin zone i.e. $-\pi \leq k < \pi$. Then the density of states is given by

$$
\begin{aligned}
\rho(\epsilon) &= 2 \int_0^\pi \delta\left(\epsilon - \cos(k)\right) dk \\
&= -2 \int_{-1}^1 \frac{\delta(\epsilon - y)}{\sqrt{1 - y^2}} dy \\
&= \frac{2}{\sqrt{1 - \epsilon^2}}, \qquad\qquad |\epsilon| \leq 1, \tag{3.5}
\end{aligned}
$$

and where the substitution $y = \cos(k)$ was used. Proceeding along similar lines, we may obtain the density of states for the tight-binding model on the square lattice [32] as

$$\rho_{\text{2D}}(\epsilon) = \frac{1}{\pi^2} K(1 - \epsilon^2/4), \tag{3.6}$$

where $K(m)$ is the elliptic function of the first kind [33] with parameter m. For complicated lattice structures, a more refined formalism like the lattice Green's function is required in order to calculate its density of states.

3.2.1 Lattice Green's functions

Lattice Green's functions (LGF) of systems are ubiquitous [32, 34] in solid state physics appearing in problems of lattice vibrations, of spin wave theory of magnetic systems, of localized oscillation modes at lattice defects, in combinatorial problems in lattices [35], and in flux calculations in lattice percolation [36]. The LGF $G(t, \vec{r})$ in the complex energy variable $t = \epsilon - i\kappa$ between the (arbitrary) lattice origin and

the point $\vec{\mathbf{r}}$ is defined as the solution to the inhomogeneous difference equation

$$[2t - H(\vec{\mathbf{r}})]G(t, \vec{\mathbf{r}}) = 2\delta_{\vec{\mathbf{r}}, \vec{\mathbf{0}}} \tag{3.7}$$

corresponding to the linear, Hermitian, time-independent operator $H(\vec{\mathbf{r}})$. This operator is generally taken to be the discrete Laplacian for lattice problems. Its action on an n-variable function $\phi(\vec{\mathbf{r}} \equiv \{r_1, r_2 \cdots r_n\})$ is given by

$$H(\vec{\mathbf{r}})\phi(\vec{\mathbf{r}}) = \sum_{\vec{\Delta} \in \mathcal{N}} \phi(\vec{\mathbf{r}} + \vec{\Delta}) - z\phi(\vec{\mathbf{r}}), \tag{3.8}$$

where $\mathcal{N}$ denotes the set of nearest neighbours of $\vec{\mathbf{r}}$ and $z \equiv |\mathcal{N}|$ is the number of such elements. In subsequent analysis, we will neglect the second term in (3.8) because it merely adds a constant shift to the energy variable t. With that, (3.7) defining the LGF is expressed as

$$\left[2tG(t, \vec{\mathbf{r}}) - \sum_{\vec{\Delta} \in \mathcal{N}} G(t, \vec{\mathbf{r}} + \vec{\Delta}) \right] = 2\delta_{\vec{\mathbf{r}}, \vec{\mathbf{0}}}. \tag{3.9}$$

The above equation may be readily solved by taking its Fourier transform into $\vec{\mathbf{k}}$-space, noting that $G(t, \vec{\mathbf{r}} + \vec{\Delta}) \leftrightarrow e^{i(\vec{\mathbf{k}}.\vec{\Delta})}\tilde{G}(t, \vec{\mathbf{k}})$, where $\tilde{G}$ denotes the Fourier transformed variable. For a simple cubic lattice in d-dimensions with unit lattice distances, this can be written, after inverse Fourier transforming, as

$$G(t, \vec{\mathbf{r}}) = \left(\frac{1}{2\pi} \right)^d \int \cdots \int_{-\pi}^{\pi} \frac{\prod_{i=1}^{d} dk_i e^{\vec{\mathbf{k}}.\vec{\mathbf{r}}}}{t - \omega(\vec{\mathbf{k}})}. \tag{3.10}$$

where $\omega(\vec{\mathbf{k}}) = \sum_{i=1}^{d} \cos(k_i)$. The general form for the LGF for other lattices like body-centred cubic, face-centred cubic remain the same [34]. In many cases such integrals may be exactly solved in terms of the elliptic integrals of the first and second kind. Once a solution for the LGF is obtained, we may obtain information about the eigenvalues and eigenfunctions of the operator $H(\vec{\mathbf{r}})$. And any solution of the inhomogeneous equation may be constructed using $G(t, \vec{\mathbf{r}})$. The density of states (DOS) $\rho(\epsilon)$, introduced in (3.4) and which will be a focus of this section, in terms of the Green's function is given by

$$\rho(\epsilon) = \lim_{\kappa \to +0} \frac{1}{\pi} \Im\left[G(t, \vec{\mathbf{0}}) \right], \tag{3.11}$$

where $\Im$ denotes the imaginary part.

In the remaining, we present results for three related lattices at $\vec{\mathbf{r}} = \vec{\mathbf{0}}$. In the subsection 3.2.2, we derive the LGF and DOS for the kagome lattice, which is shown in Fig. 3.2a. In the next subsection 3.2.3 we perform similar calculations for the diced lattice which is shown in Fig. 3.2b. Some of these results were obtained earlier [37] but we repeat it here to correct a minor error in Ref. [37]. And then in subsection 3.2.4, we attempt to obtain a closed form solution for LGF and DOS for the hyperkagome lattice, which is shown in Fig. 3.3a. We could not solve this exactly in a closed form but numerical evaluation of this integral to obtain the DOS does, however, compare well with a previously published purely numerical evaluation of the DOS.

3.2.2 Kagome lattice

The kagome lattice has 3 atoms per unit cell labelled A, B, C in Fig. 3.2a. The side-length of the simple triangle $a = 1$ and the vertical height $b = \sqrt{3}/2$. We use the general formalism presented in the previous

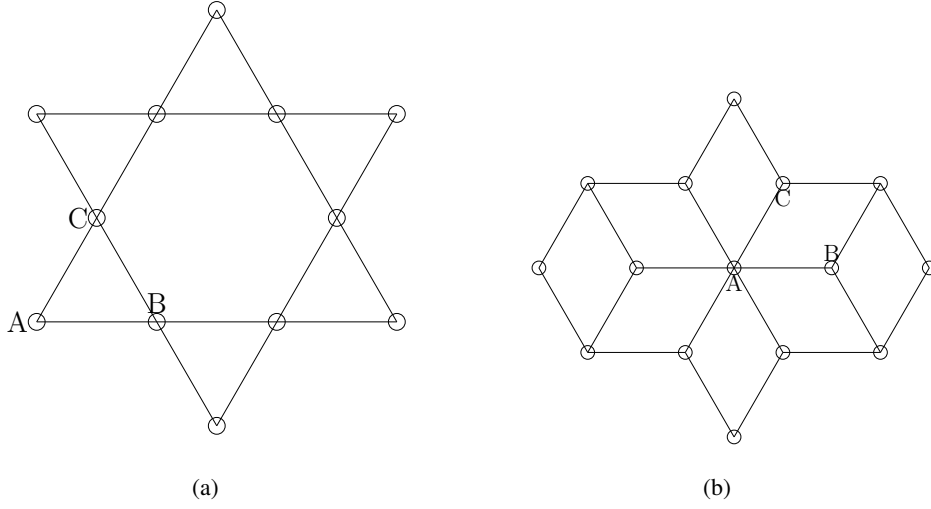(a)   (b)

Figure 3.2: (a) Kagome lattice. (b) Dual to the kagome, diced lattice.

subsection to calculate the LGF at the origin using (3.9) and the DOS from the imaginary part using (3.11). The difference here is that we need to consider LGFs at and between the different sub-lattices α, β denoted as $G^{\alpha\beta}$. Then the right hand side of (3.9) is multiplied by an additional Kronecker delta factor $\delta_{\alpha,\beta}$ and (3.11) is modified to

$$\rho(\epsilon) = \lim_{\kappa \to +0} \frac{1}{N\pi} \Im \left[\sum_\alpha G^{\alpha\alpha}(t, \vec{0}) \right], \tag{3.12}$$

where N denotes the number of sub-lattices.

Taking the Fourier transform of (3.9) with respect to $\vec{r}$, the lattice Green's functions, evaluated at the origin, for the α-sub-lattice with respect to the other 3 sub-lattices may be written as

$$
\begin{aligned}
t\tilde{G}^{A\alpha} - \tilde{G}^{B\alpha} \cos(ak_x + bk_y) - \tilde{G}^{C\alpha} \cos(ak_x - bk_y) &= \delta_{A\alpha}, \\
-\tilde{G}^{A\alpha} \cos(ak_x + bk_y) + t\tilde{G}^{B\alpha} - \tilde{G}^{C\alpha} \cos(2ak_x) &= \delta_{B\alpha} \\
-\tilde{G}^{A\alpha} \cos(ak_x - bk_y) - \tilde{G}^{B\alpha} \cos(2ak_x) + t\tilde{G}^{C\alpha} &= \delta_{C\alpha},
\end{aligned}
\tag{3.13}
$$

where $\alpha = A, B, C$ refers to the sub-lattices. The LGFs $\tilde{G}^{\alpha\beta}$ depend on (t, k_x, k_y) but has been suppressed in the above equation for notational simplicity. It is a straightforward task to solve for $\tilde{G}^{\alpha\beta}$ from the above set of linear equations by setting particular values for α in (3.13). Then we may write the "diagonal" lattice Green functions i.e. $\alpha = \beta$ as

$$
\begin{aligned}
\tilde{G}^{AA} &= [t^2 - \cos^2(2ak_x)]/\mathcal{D}, \\
\tilde{G}^{BB} &= [t^2 - \cos^2(ak_x - bk_y)]/\mathcal{D}, \\
\tilde{G}^{CC} &= [t^2 - \cos^2(ak_x + bk_y)]/\mathcal{D},
\end{aligned}
\tag{3.14}
$$

where $\mathcal{D} \equiv (t+1)\left[t(t-1) - \cos(2ak_x)(\cos(2ak_x) + \cos(2bk_y))\right]$. The "off-diagonal" lattice Green func-

tions may be similarly calculated as well from (3.13).

From the knowledge of the Fourier-space diagonal LGFs $\tilde{G}^{\alpha\alpha}$ in (3.14), the DOS $\rho_{\text{kag.}}(\epsilon)$, as a function of the real energy variable $\epsilon = \Re[t]$ ($\Re$ denoting the real part), for the kagome lattice may be calculated using (3.12)

$$\rho_{\text{kag.}}(\epsilon) = \lim_{\kappa \to +0} \frac{1}{3\pi} \Im \left[\frac{1}{t+1} + \mathcal{F}^{-1} \left(2 \frac{2t-1}{\tau' - \omega'_k} \right) \right], \tag{3.15}$$

where $\tau' \equiv 2\epsilon^2 - 2\epsilon - 1$, $\omega'_k \equiv \cos(4ak_x) + 2\cos(2ak_x)\cos(2bk_y)$ and $\mathcal{F}$ denotes the Fourier transform of the $\vec{\mathbf{k}}$ variable within the limits $\pm\pi/a$, $\pm\pi/b$. That is,

$$\rho_{\text{kag.}}(\epsilon) = \frac{\delta(\epsilon+1)}{3} + \frac{2}{3}|2\epsilon - 1|\rho_{\text{tri}}(\tau'). \tag{3.16}$$

Here the DOS for the triangular lattice $\rho_{\text{tri}}(\epsilon)$ derived and expressed [38] in terms of the complete elliptic functions of the first kind $K(m)$, with m being the parameter, may be rewritten, in the whole range $-1.5 < \tau < 3$, as

$$\rho_{\text{tri}}(\tau) = \frac{\Re[K(1 - 1/k(\tau)^2)]}{\pi^2(2\tau+3)^{\frac{1}{4}}},$$

where $k(x)^{-2} = \dfrac{[\sqrt{(2x+3)} - 1]^3[\sqrt{(2x+3)} + 3]}{16\sqrt{(2x+3)}}$. It may be checked that the spectral density integrates to one i.e. $\int_{-1}^{2} \rho_{\text{kag.}}(\epsilon)\,d\epsilon = 1$. The expression in (3.16) checks with an earlier result [39] wherein no derivation of the result was provided. We additionally have obtained the diagonal LGFs, in Fourier space, for the kagome lattice in (3.13).

3.2.3 Diced lattice

The diced lattice is the dual to the kagome lattice and is shown in Fig. 3.2b with its three sub-lattices again labelled as A, B, C. The length of segment AB is taken to be one. Here we merely recapitulate the work of Ref. [37] in slightly different form, to correct a minor error in the density of states. The calculations proceed as in the previous section and the missing details may readily be worked out or obtained from Ref. [37]. The LGF at the origin $\tilde{G}^{\alpha,\alpha}(t, k_x, k_y)$ - where $\alpha = (A, B, C)$, (k_x, k_y) are the Fourier space components as in section 3.2.2 - for the 3 sub-lattices A, B, C are given by

$$\tilde{G}^{AA}(t, k_x, k_y) = \frac{4t}{4t^2 - (1 + \gamma^2)\omega_k},$$

$$\tilde{G}^{BB}(t, k_x, k_y) = \frac{4t^2 - \gamma^2\omega_k}{t[4t^2 - (1 + \gamma^2)\omega_k]},$$

$$\tilde{G}^{CC}(t, k_x, k_y) = \frac{4t^2 - \omega_k}{t[4t^2 - (1 + \gamma^2)\omega_k]}, \tag{3.17}$$

where $\omega_k \equiv 2\cos(2ak_y) + 4\cos(ak_y)\cos(bk_x)$, γ is the $A \leftrightarrow C$ hopping amplitude in units of the $A \leftrightarrow B$ hopping amplitude, which is taken to be 1. $a = \sqrt{3}/2$ and $b = 1/2$ are lattice distances in units of the inter-atomic distance. Transforming to real space i.e. $\tilde{G} \to G$, the DOS as a function of the real energy

variable $\epsilon = \Re[t]$ is given by

$$
\begin{aligned}
\rho_{\text{diced}}(\epsilon) &= \lim_{\kappa \to +0} \frac{1}{3\pi} \Im \left[\sum_\alpha G^{\alpha\alpha} \right] \\
&= \frac{\delta(\epsilon)}{3} + \frac{4\epsilon}{3\pi(1 + \gamma^2)} \Im[G_{\text{tri}}(\tau, 0, 0)],
\end{aligned}
\tag{3.18}
$$

where $\tau \equiv \dfrac{4\epsilon^2 - 3(1 + \gamma^2)}{2(1 + \gamma^2)}$ and $G_{\text{tri}}(t, x, y)$ is the LGF for the triangular lattice; the latter is known from other work [38]. Then (3.18) simplifies to

$$
\rho_{\text{diced}}(\epsilon) = \frac{\delta(\epsilon)}{3} + \frac{4\epsilon}{3(1 + \gamma^2)} \rho_{\text{tri}}(\tau).
\tag{3.19}
$$

Here too, it may be checked, say for a particular value of $\gamma = 1$, that $\int_{\frac{-3}{\sqrt{2}}}^{\frac{3}{\sqrt{2}}} \rho_{\text{diced}}(\epsilon)\,d\epsilon = 1$. In Ref. [37], the Dirac-delta term was not taken into account and the spectral density did not integrate to 1; it is clear that the flat band in the diced lattice must give rise to such a term.

3.2.4 Hyperkagome lattice

The hyperkagome lattice can be considered to be a three dimensional version of the kagome lattice. Here, there are corner-sharing tetrahedra with one of the atoms in each tetrahedron removed. The unit cell, with 12 atoms, is cubic and is shown in Fig. 3.3a. Each side of the cube is taken to have unit length. For example, the lattice point labelled 3 has (x, y, z) coordinates $(3/4, 1/4, 1/2)$, with respect to the origin O, with the nearest neighbours labelled 1, 2, 4, 5. There currently is hardly any exactly

Table 3.1: Coordinates of the neighbours of site 1 in the hyperkagome lattice as labelled in Fig. 3.3a.

| Site number	Coordinate (x, y, z)
2	$(1/2, 0, 1/2)$
3	$(3/4, 1/4, 1/2)$
6	$(0, 0, 0)$
12	$(0, 3/4, 3/4)$

known result for this lattice, even for non-interacting models. However it was conjectured [42] that lattices with cubic cells should have a lattice Green's functions expressible in a "canonical" integral form, which, in general, can be exactly evaluated; a rationale for this proposition was later given [43]. Glasser's canonical form for the Green's function is

$$
G = \frac{1}{\pi^3} \iiint_0^\pi \frac{dx\,dy\,dz}{t - F(\cos x, \cos y, \cos z)},
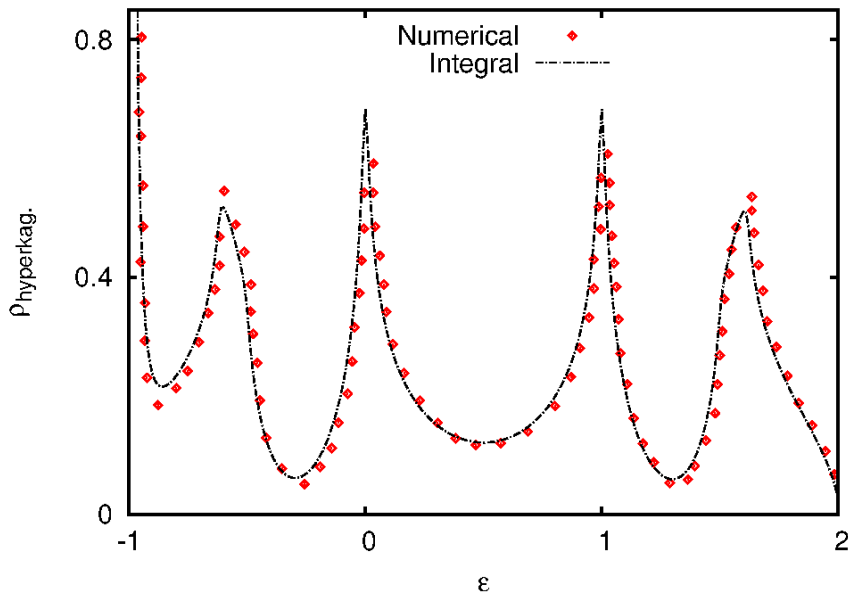\tag{3.20}
$$

where

$$
F(x, y, z) = a_1 x + a_2 y + a_3 z + a_4 xy + a_5 yz + a_6 xz + a_7 xyz.
$$

Here, based on calculations for the hyperkagome's LGF and DOS, we obtain a form that resembles the canonical form of Glasser. This we solve numerically and compare with other purely numerical results.
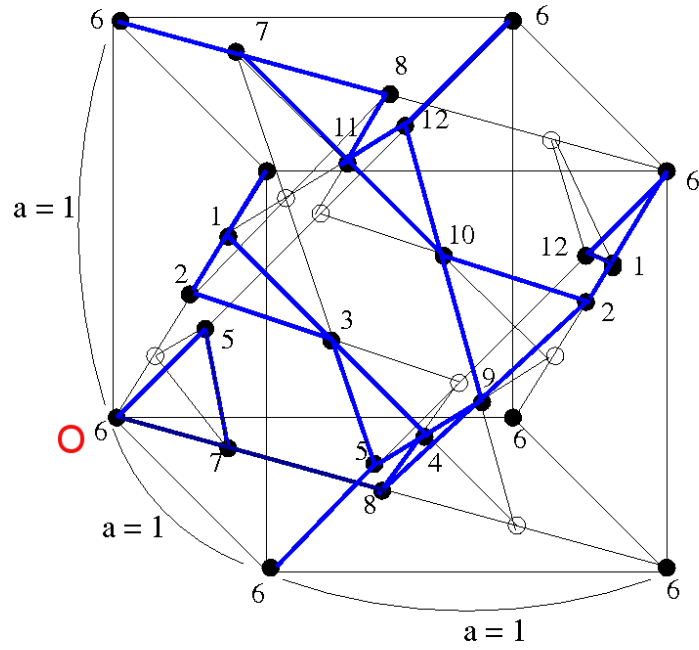
(a)

(b)

Figure 3.3: (a) Unit cell, from Ref. [40] with authors' permission, of the hyperkagome lattice with blue lines and filled circles; the origin is marked with a red O. The additional empty circles indicate the underlying pyrochlore lattice. (b) Density of states for the hyperkagome, from evaluating (3.24), compared with numerical results from Ref. [41]. Note that the latter had to be multiplied by a factor of 2 to account for their doubling of the energy scales compared to ours.

Corresponding to each of the 12 lattice points, each of which has four nearest neighbours, there will be one LGF equation. These may be obtained in the same way that led (3.9) to (3.13). Consider the site labelled 1 in Fig. 3.3a which has coordinates $(3/4, 0, 3/4)$ and, for its translated version, $(3/4, 1, 3/4)$; this has lattice sites numbered $2, 3, 6, 12$ as its neighbours, with relative displacements indicated as in table 3.1. Using this, the Green's function equation in (3.12) may be written, with respect to the site 1, as

$$2t\tilde{G}^{1\alpha} - \mathrm{e}^{-i(k_x/4+k_z/4)}\tilde{G}^{2\alpha} - \mathrm{e}^{i(k_y/4-k_z/4)}\tilde{G}^{3\alpha} - \mathrm{e}^{i(k_x/4+k_z/4)}\tilde{G}^{6\alpha} - \mathrm{e}^{i(k_x/4-k_y/4)}\tilde{G}^{12\alpha} = 2\delta_{1\alpha}. \qquad (3.21)$$

Therefore, upon tabulating every vertex and its neighbours, we may generalize the above analysis that led to (3.21) for the site 1 to the entire unit cell. The system of equations for any α sub-lattice, using the corresponding LGF column vector $\tilde{\mathcal{G}}^{\alpha}_{12\mathrm{x}1} \equiv \left[\tilde{G}^{1,\alpha} \cdots \tilde{G}^{12,\alpha}\right]^T$, is given by

$$C\tilde{\mathcal{G}}^{\alpha} = 2\left[\delta_{1,\alpha} \cdots \delta_{12,\alpha}\right]^T_{12\mathrm{x}1}, \qquad (3.22)$$

where the 12x12 coefficient matrix C is given by

$$C = \begin{pmatrix} 2t & \xi_{-x-z} & \xi_{y-z} & 0 & 0 & \xi_{x+z} & 0 & 0 & 0 & 0 & 0 & \xi_{x-y} \\ \xi_{x+z} & 2t & \xi_{x+y} & 0 & 0 & 0 & 0 & 0 & \xi_{-y-z} & \xi_{-x-y} & 0 & 0 \\ \xi_{-y+z} & \xi_{-x-y} & 2t & \xi_{y-z} & \xi_{x-z} & 0 & 0 & 0 & 0 & 0 & 0 & 0 \\ 0 & 0 & \xi_{-y+z} & 2t & \xi_{x-y} & 0 & 0 & \xi_{-x-z} & \xi_{-x+y} & 0 & 0 & 0 \\ 0 & 0 & \xi_{-x+z} & \xi_{-x+y} & 2t & \xi_{-y-z} & \xi_{x-z} & 0 & 0 & 0 & 0 & 0 \\ \xi_{-x-z} & 0 & 0 & 0 & \xi_{y+z} & 2t & \xi_{x+y} & 0 & 0 & 0 & 0 & \xi_{-y-z} \\ 0 & 0 & 0 & 0 & \xi_{-x+z} & \xi_{-x-y} & 2t & \xi_{x+y} & 0 & 0 & \xi_{y-z} & 0 \\ 0 & 0 & 0 & \xi_{x+z} & 0 & 0 & \xi_{-x-y} & 2t & \xi_{y+z} & 0 & \xi_{-x-z} & 0 \\ 0 & \xi_{y+z} & 0 & \xi_{x-y} & 0 & 0 & 0 & \xi_{-y-z} & 2t & \xi_{-x+z} & 0 & 0 \\ 0 & \xi_{x+y} & 0 & 0 & 0 & 0 & 0 & 0 & \xi_{x-z} & 2t & \xi_{-y+z} & \xi_{-x+z} \\ 0 & 0 & 0 & 0 & 0 & 0 & \xi_{-y+z} & \xi_{x+z} & 0 & \xi_{y-z} & 2t & \xi_{-x+y} \\ \xi_{-x+y} & 0 & 0 & 0 & 0 & \xi_{y+z} & 0 & 0 & 0 & \xi_{x-z} & \xi_{x-y} & 2t \end{pmatrix}, \qquad (3.23)$$

and the symbol $\xi_{\pm\mu\pm\nu} \equiv \exp\left[i/4\left(\pm k_\mu \pm k_\nu\right)\right]$. Now there are 12 systems (for each value of α) of 12 linear equations, which is cumbersome to solve by hand as done in previous two subsections for smaller systems. To obtain the diagonal LGFs, we use Mathematica [23] to obtain each $\tilde{G}^{\alpha\alpha}$. With these solutions we can use (3.13) to express the DOS $\rho_{\text{hyperkag.}}$ for the hyperkagome as

$$\rho_{\text{hyperkag.}}(\epsilon) = \lim_{\kappa \to +0} \frac{1}{3\pi} \Im\left[\mathcal{F}^{-1}\left(\frac{P(a_0, a_1, a_2, a_3)}{P(b_0, b_1, b_2, b_3)}\right)\frac{1}{t+1}\right]. \qquad (3.24)$$

Here the inverse Fourier transform $\mathcal{F}^{-1}$, at $\vec{\mathbf{r}} = \vec{\mathbf{0}}$, of a function g is given by $\mathcal{F}^{-1}g = \frac{1}{\pi^3}\iiint_0^\pi g(\vec{\mathbf{k}})d\vec{\mathbf{k}}$. The a_i and b_i parameters are only functions of t with no dependence on the lattice momenta i.e.

$$
\begin{aligned}
a_0 &= 3(-1 + 12t + 72t^2 - 144t^3 - 256t^4 + 448t^5 + 128t^6 - 384t^7 + 128t^8), \\
a_1 &= -4(1 + 7t - 6t^2 - 20t^3 + 16t^4), \\
a_2 &= 4(1 + 3t - 6t^2), \\
a_3 &= 12t(1 - 2t), \qquad\qquad\qquad\qquad\qquad\qquad\qquad\qquad\qquad\qquad\qquad (3.25)
\end{aligned}
$$

and the b_i parameters are given by

$$b_0 = 1 - 16t + 112t^2 + 64t^3 - 544t^4 + 256t^5 + 512t^6 - 512t^7 + 128t^8,$$
$$b_1 = -16t(1 + t - 4t^2 + 2t^3),$$
$$b_2 = -16t(t - 1),$$
$$b_3 = 4(-1 + 4t - 4t^2). \tag{3.26}$$

The P function is given by

$$P(a, b, c, d) = a + b \sum_{i=1}^{3} \cos(x_i) + c \sum_{i=1}^{3} \cos(x_i) \cos(x_{i+1}) + d \prod_{i=1}^{3} \cos(x_i) + \sum_{i=1}^{3} \cos(2x_i),$$

Numerical evaluation of the hyperkagome's DOS [41] is compared with a numerical evaluation of the integral in (3.24) and is shown in Fig. 3.3b. Note that (3.24) correctly shows the appearance of a flat band at $t = -1$ as indicated by the simple pole. And as noted from numerical calculations [41], there is a drop to zero in the kagome lattice's DOS for the non-interacting Hubbard model (which is merely the second-quantized form of the operator $H(\vec{r})$) but a continuum of energy states in the hyperkagome. We may see this explicitly from (3.16) with the appearance of a zero at $2t - 1 = 0$; no such apparent zero occurs for the case of the hyperkagome in (3.24), verified by numerical integration of the same as shown in Fig. 3.3b. A continuum of states is, of course, indicative of conductive behaviour.

Many similar integrals - which can be exactly solved - appear in the literature [42, 44] for the lattices with a cubic unit cell but not with all the sums and products of H appearing together. In particular, the last summations of $\cos 2x$ in the P-function do not appear in the canonical form in (3.20). It is unclear if these terms might suggest a generalization of the canonical form or if integrability is destroyed by their presence. We have currently found no way to exactly solve (3.24).

3.2.5 Fermionic systems

As remarked at the beginning in section 3.2, the preceding analysis holds for any kind of particle on the lattices concerned. The particle's statistics may be incorporated by using the appropriate distribution from (3.3). For instance, the particle density of fermions on a system with density of states $g(\epsilon)$ is given by

$$n = \int g(\epsilon) f_{\text{FD}}(\epsilon, \mu, T) \mathrm{d}\epsilon, \tag{3.27}$$

with the chemical potential determining the density at a given temperature. At $T = 0$ the Fermi-Dirac statistics is non-zero only when $\epsilon < \mu = \epsilon_F$, the Fermi energy. Therefore the lowest μ when a finite density sets in is at the lowest band edge. For instance, these values for the kagome, square and triangular lattices are $\mu = -1, -2, -1.5$ respectively.

However for the kagome lattice, due to the presence of a Dirac delta term of weight $1/3$ in its density of states as seen in (3.16), there will be an abrupt jump in the particle density at the lowest band edge. For the square and triangular lattices, on the other hand, the transition to finite densities is a smooth one due to the absence of such a term. For the electronic tight-binding model (3.2), the particle densities are solved using (3.27) and plotted in Fig. 3.4a at a low temperature of $T = 0.005$. Here the abrupt jump in fermionic density for a given spin species may be seen on the kagome lattice and the emergence of an almost incompressible phase close to the filling $2/3$; the smooth touching of the two dispersive bands (indicated by a zero in the density of states in (3.16)) precludes the existence of a true incompressible phase in the system. Moreover, we see that for the original Hamiltonian in (3.2) with $\mu = 0$, only
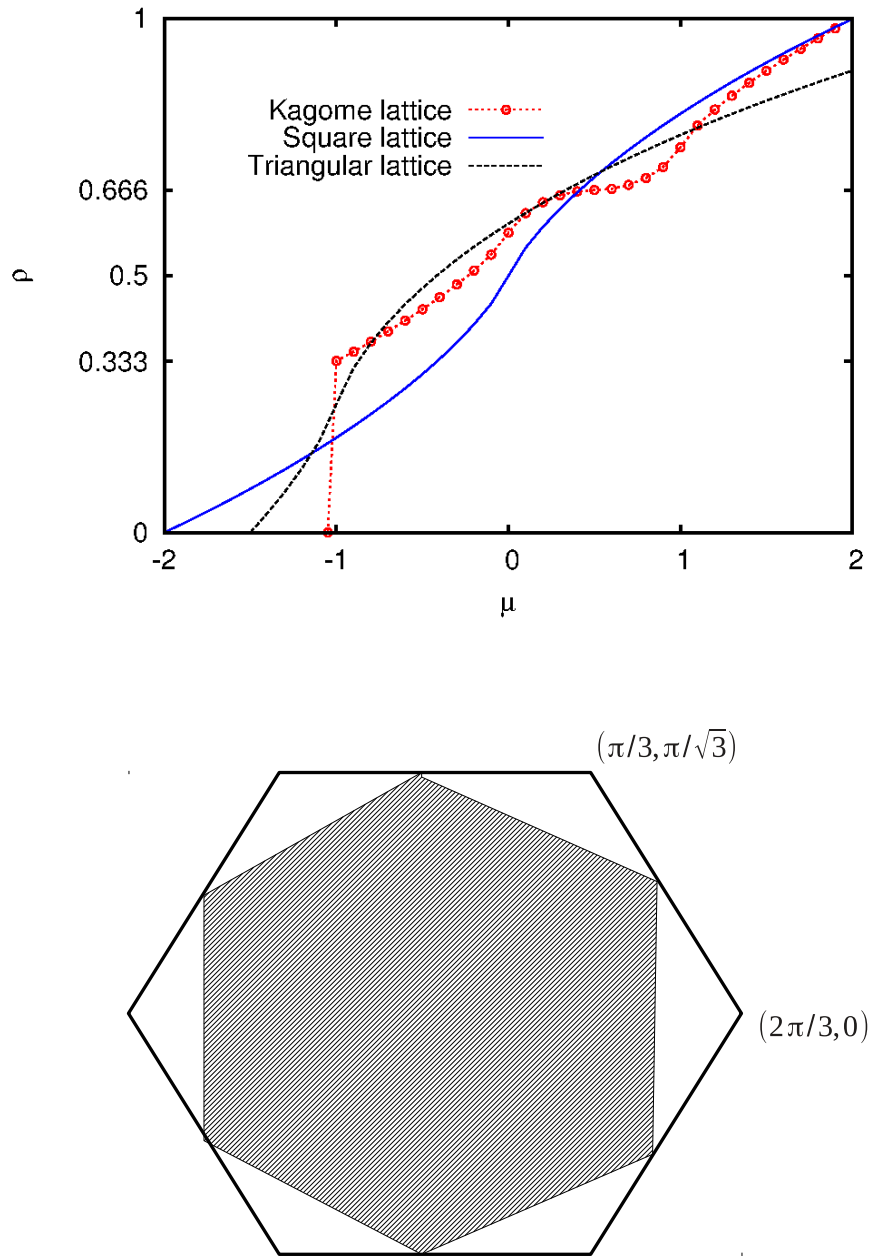
Figure 3.4: (a) Density of spin σ fermions versus chemical potential for the tight binding model (3.2) on the square, triangular and kagome lattices at temperature $T = 0.005$. The presence of an almost incompressible phase $\left(\dfrac{\partial \rho}{\partial \mu} \approx 0\right)$ is seen close to the filling 2/3 for the kagome lattice, which is absent for the other two lattices. (b) The boundary of the shaded region in the first Brillouin zone determines the Fermi surface for the tight binding kagome lattice with density $\rho = 7/12$.

the square lattice is half-filled at zero temperature; for the kagome and triangular lattices, the stable ground state particle densities at $\mu = 0$ are $\frac{7}{12} = 0.583\ldots$ and $0.601\ldots$ respectively. The corresponding occupied states in the first Brillouin zone of the kagome lattice may be constructed by noting that the lower dispersive band

$$\epsilon_2\left(\vec{\mathbf{k}}\right) = \frac{1}{2}\left(1 - \sqrt{3 + 2\cos\left(2k_x\right) + 4\cos\left(k_x\right)\cos\left(\sqrt{3}k_y\right)}\right) \tag{3.28}$$

equal zero to determine the region of filling within the first Brillouin zone. Thus we may determine the Fermi surface as the boundary of the shaded region in Fig. 3.4b. The two dispersive bands also possess low-energy excitations that resemble those of graphene close to the Brillouin zone edges due to the presence of a Dirac cone structure. This may be seen from (3.28) at, say, the phase point $\vec{\mathbf{k}} \approx \left(\frac{2\pi}{3}, 0\right)$. Then the dispersion in (3.28), retaining up to second order terms, may be approximated by

$$\epsilon_2(\vec{\mathbf{k}}) \approx \frac{1}{2}(1 - \sqrt{3}|\delta\vec{\mathbf{k}}|), \tag{3.29}$$

where $|\delta\vec{\mathbf{k}}|$ is the deviation from the Brillouin zone's corner. The linear dependence in (3.29) for the lower band is reminiscent of the relativistic dispersion of Dirac fermions seen in graphene; a similar conclusion holds for the upper band. It was shown in Ref. [31] that upon the addition of spin-orbit coupling to the tight-binding Hamiltonian for filling $\rho = 1/3$, a gap opens at these Dirac points and a topological insulator emerges. Due to the protected nature of edge states and the lack of their susceptibility to external perturbations, today there is much work on the prospect of topological insulators as a route towards quantum computation [45].

3.3 Classical limit

In the classical limit the terms that determine the hopping of particles, which comprise the field operators determining the quantum nature of the particles, are ignored. This may be viewed as a purely interaction driven model. This limit is opposite to that considered in the previous section and the analysis will therefore be considerably different. A paradigmatic fruit-fly example of a classical model in statistical physics is the Ising model [46] in an external longitudinal field given by the Hamiltonian

$$\mathcal{H} = J\sum_{<i,j>}\sigma_i^z\sigma_j^z - h\sum_i\sigma_i^z, \tag{3.30}$$

where σ_i^z is the usual Pauli matrix and takes the values ± 1 on each site i, h is the magnitude of the field, and the angular brackets denote nearest neighbour interactions with strength J. An additional transverse field $\Gamma\sigma_i^x$ adds quantum fluctuations to the above model.

Although (3.30) represents the simplest possible statistical model, it provides room for rich physics; many rare earth compounds (lanthanide series) have been found to realize such an interaction. This is because the tripositive ion is usually the most stable configuration for the lanthanides [47], leaving one unpaired electron. For instance, the dysprosium ion Dy^{3+} has the electronic configuration $[Xe]4f^9$ leaving one unpaired electron which acts as an Ising spin. In metallic halides such as $NdCl_3$ and $NdBr_3$, Prinz [48] showed that specific structures in the absorption spectra might be explained by positing a nearest-neighbour and next-nearest-neighbour S^z interaction between the neodymium ions.
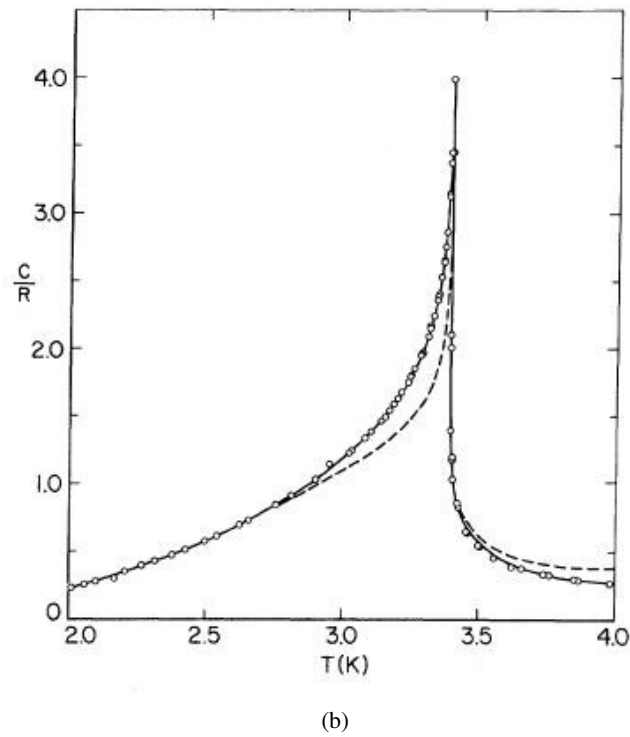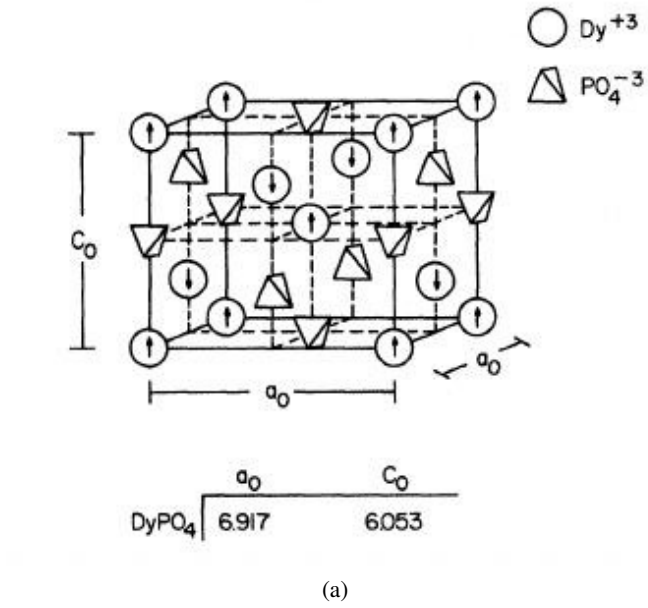
(a)

(b)

Figure 3.5: (a) Unit cell of DyPO$_4$ with arrows indicating the ordered magnetic state of the compound; the lattice parameters $a_0, c_0 \approx 6 - 7$Å. (b) Measured heat capacity (circles) of DyPO$_4$ compared to series expansion results (solid line) for the Ising model on the diamond lattice in the transition region to Néel ordering; dashed lines indicate calculations from magnetic susceptibility. Both figures are from Ref. [49].

Another such lanthanide compound investigated was $DyPO_4$ (Fig. 3.5a), which was argued to realize a three dimensional Ising antiferromagnet on a diamond lattice. Indeed, series expansion results of the Ising model on the diamond lattice were compared with heat capacity measurements of the compound and were found to be in good agreement [49] close to the Néel transition as shown in Fig. 3.5b.

3.3.1 Introduction

In this subsection we describe some of the known theoretical results for the Ising model on two lattices in order to motivate the specific problem we take up in the next section. Consider first a one dimensional chain modelled by (3.30); this may be readily solved following the work of Ising [46] to give the magnetization per site as

$$m = \frac{\sinh{(h\beta)}}{\sqrt{e^{J\beta} + \sinh^2{(h\beta)}}},$$ (3.31)

at inverse temperature β. As noted by Ising [46], there is no finite temperature phase transition in this
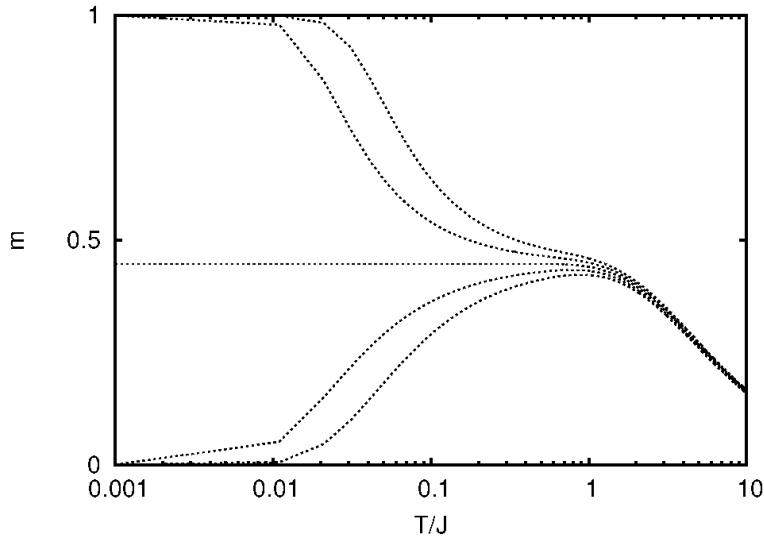

Figure 3.6: Magnetization per site in the one dimensional Ising model close to the saturation field. This field value separates a zero magnetization and a polarized state, with a value of $1/\sqrt{5}$ right at the saturation field.

model and hence no non-trivial critical point; it was thereby erroneously concluded that none would exist in any dimension. However, in the one dimensional system, there is a field induced transition as plotted in Fig. 3.6 close to the saturation field $h = h_c = |2|$ beyond which ordering sets in. Clearly the transition is a first order transition as seen from the jump in the magnetization. Moreover, at this phase point, there exists a finite residual entropy per site (in units of the Boltzmann's constant k_B) of $\log\left(\dfrac{1 + \sqrt{5}}{2}\right)$ [50].

Upon the addition of quantum dynamics through a transverse field Γ, a disordered phase sets in only after a critical value [53, 54]; at zero longitudinal field, this is in the universality class of the two dimensional square Ising model, which is again an exactly soluble model. A generic phase point with $h \neq 0, \Gamma \neq 0$ has to be numerically analyzed. A transverse field model has been used to describe the properties of many materials beginning with the work of de Gennes [55], who used it to describe
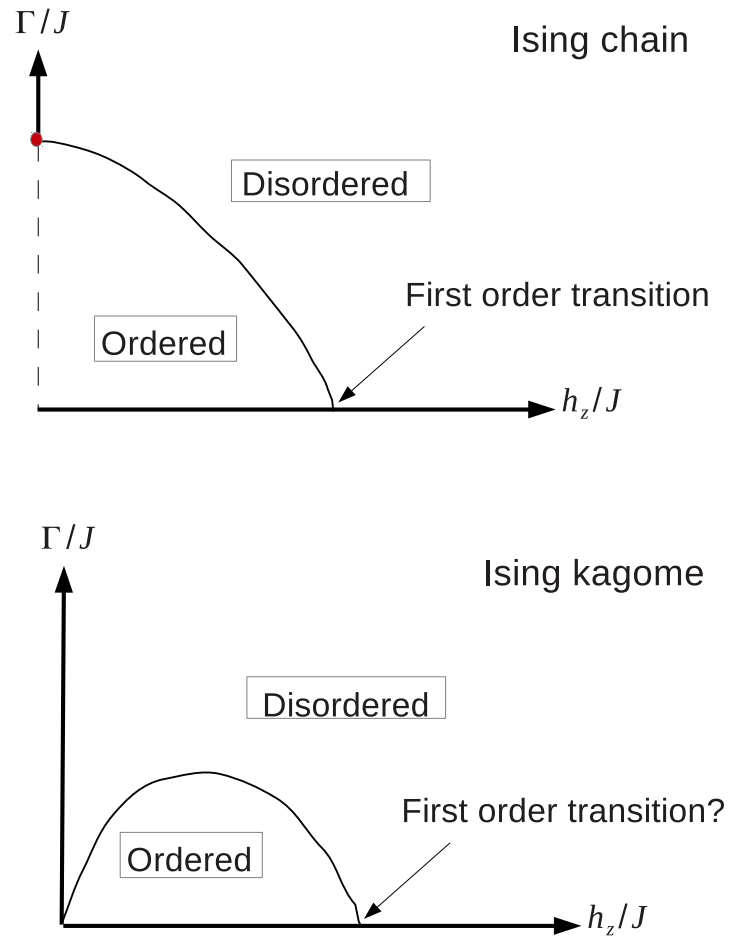
Figure 3.7: Qualitative phase diagram of the Ising model in combined longitudinal $h_z \equiv h$ and transverse Γ fields for the Ising model on the chain and kagome lattices. For the chain lattice, the following 2 segments are exactly soluble: (i) segment $h_z = 0$ (dotted line indicating universality class of 2D square lattice Ising model) ending in a quantum critical point (red circle) and (ii) segment $\Gamma = 0$. For the kagome lattice there is no ordering for zero longitudinal field [51], and the only integrable point is at the origin [52].

the transition from an ordered phase (small Γ) to a disordered phase (large Γ) in ferroelectrics such as KH_2PO_4.

For the kagome lattice, the situation is slightly different [51, 52]. At finite temperatures and zero external fields, the Ising model is disordered with an extensive ground state degeneracy. At zero temperature an additional longitudinal field lifts the ground state degeneracy slightly into an ordered state (finite ferromagnetic moment) with an extensive entropy; an infinitesimal transverse field will drive the system towards a disordered phase in the absence of a longitudinal field. Qualitative sketches of the ground state phase diagram for the one dimensional chain and the kagome lattice are shown in Fig. 3.7.

3.3.2 Saturation entropy

As we have seen in Figs. 3.6 and 3.7, there are certain longitudinal field values where the system transits to a different phase at zero (or low) temperature. Indeed, it was argued by Isakov et al. [56] that for the spin ice compound $Dy_2Ti_2O_4$ (dysprosium titanium oxide) the physics close to the saturation field is governed by decoupled planes of (pseudospin) Ising kagome lattices. Moreover, they provide a qualitative sketch of entropy variation as a function of the external [111] field for the spin-ice compound, which we reproduce in Fig. 3.8a. In fact, we remark that such a dependence seems to be a generic one for Ising lattice models. Experimental measurements of low temperature entropy of the compound as a function of the field clearly show a peaking structure close to the transition field; we show such a measurement in $Dy_2Ti_2O_4$ in Fig. 3.8b from Ref. [57]. However, the values of the peak obtained in Ref. [56] and by us in section 3.3.4 are slightly larger. This either indicates the need for more than Ising physics close to the saturation field or, as suggested in Ref. [56], more data points in the measurements to resolve the peak.

Antiferromagnetic Ising models can harbour a macroscopic number of degenerate ground states at zero external field on frustrated lattices like the triangular lattice [58], kagome lattice [52], pyrochlore lattice [59, 60], to name a few. An extensive entropy may survive, albeit with different values, even for infinitesimal fields [56, 61, 62] on certain lattices; as the field is varied, a strongly enhanced peak in the entropy develops just before the field-induced spin-ordering sets in [56, 63, 64]; this substantial peak occurs because, at this field strength, a large number of non-neighbouring spins may be flipped against the field without a cost in energy [64]. In fact, such residual saturation entropies $S^{sat.}$ persist in quantum spin models (anisotropic Heisenberg models), although with different values from the Ising limits, and for different reasons [65, 66] pertaining to the existence of localized magnons.

Our results are summarized in table 3.3. In section 3.3.3, residual saturation entropies of related quasi one-dimensional lattices or ladders are exactly computed; of which, one of the ladders will be used to build up the kagome lattice (Fig. 3.2a). For the kagome lattice, we deduce approximate values of $S^{sat.}$ from calculations for spin ice on the pyrochlore lattice in a [111] field [56]; results of Monte Carlo simulations, series expansion techniques [67] and the Bethe approximation were found to be comparable [56] for the saturation entropy.

In section 3.3.4, we elucidate a procedure for obtaining a more accurate estimate of this value through (a) transfer matrix methods, and equivalently (b) the solution of appropriate difference equations that generate the partition function. We finally provide a considerably improved estimate of $S^{sat.}$ for the kagome lattice using Binder's algorithm. With which we may exactly calculate the partition function of a system of over, in our case, 1300 Ising spins at the saturation field with the expenditure of modest computational resources. We point out that it is only for the Ising kagome lattice, among other two dimensional lattices, that the zero field entropy exceeds the saturation field entropy.

The antiferromagnetic Ising models we investigate are described by the Hamiltonian

$$\mathcal{H} = \sum_{<i,j>} \sigma_i \sigma_j - h_c \sum_i \sigma_i, \tag{3.32}$$

on an N site lattice with $|h_c| = z$, the nearest number of neighbours. This is the saturation field beyond which ordering sets in. The variables $\sigma_i = \pm 1$ which we represent by up and down spins, and the interaction between nearest neighbours is denoted by the angular brackets, setting the energy scale of the problem. The boundary conditions are chosen to be either free or periodic. Although the number of allowed states for a given finite system will differ depending on the boundary conditions, the dominant multiplicative degeneracy of the system as $N \to \infty$ will reflect the bulk property. It will then be a question of computational convenience whether free or periodic boundary conditions be chosen.
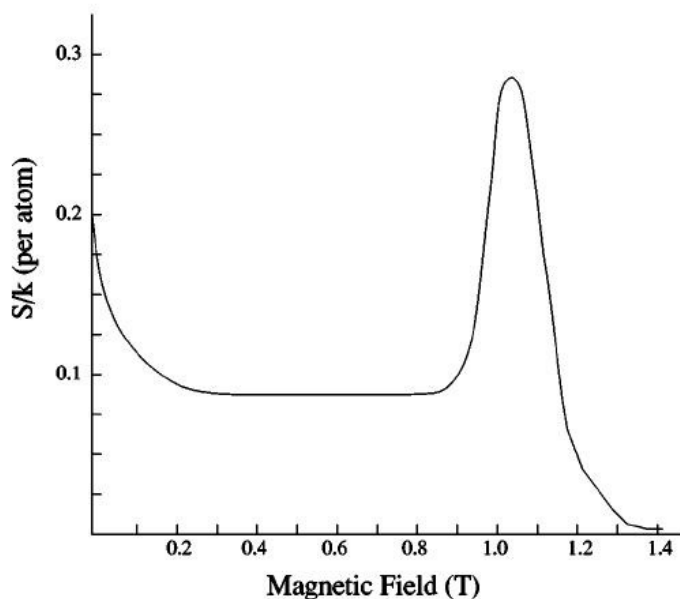
(a)
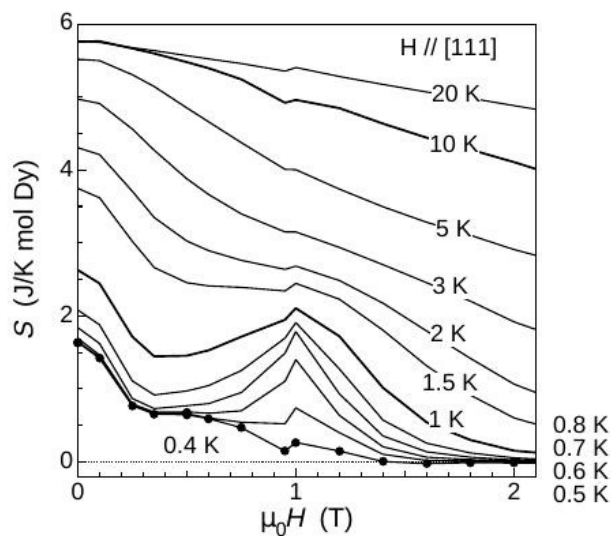
(b)

Figure 3.8: (a) Qualitative sketch of entropy in a spin-ice compound as a function of the [111] field. Taken from Ref. [56]. The pronounced peak corresponds to the saturation entropy. (b) Experimental measurements of entropy in $Dy_2Ti_2O_4$ close to the transition temperature and field. Taken from Ref. [57].

Pauling's ice entropy

Before we move onto the calculations of concern, we briefly describe an early and noteworthy measurement of the zero point entropy of a material, a technique adopted for which we will employ later: that for ordinary ice. In the determination of thermodynamic properties of water, two methods of calculating its entropy were found to be in discrepancy by about 0.82 calories/deg./mole at standard pressure. The

first value was determined from spectroscopic data [68]; this may in principle be calculated by spectroscopically determining the energy spectrum of the molecule and expressing the partition function at inverse temperature β as [69]

$$\mathcal{Z} = \sum_j \exp(-\beta \epsilon^T - \beta \epsilon^R - \beta \epsilon^V - \beta \epsilon^E), \qquad (3.33)$$

where the superscripts stand for translational, rotational, vibrational and electronic contribution to the energy spectrum of the molecule. This gave an entropy value, at 298.1 Kelvin, of 45.1 calories/deg./mole. Later calorimetric measurements [70] gave a corresponding value of 44.28 ± 0.05 calor-
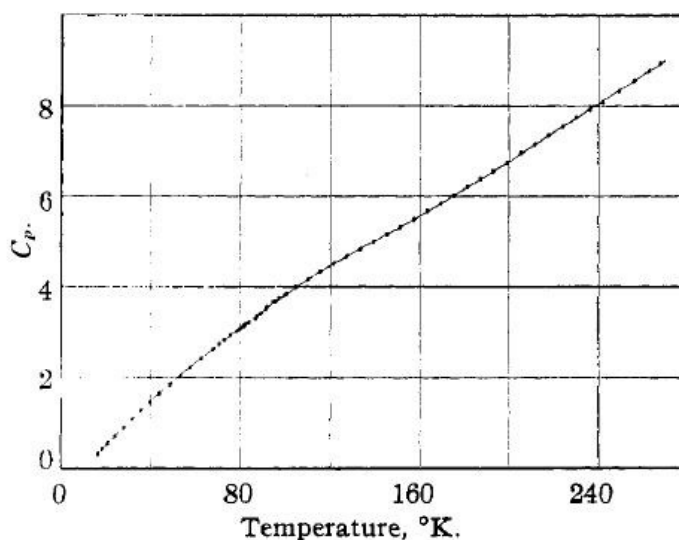

Figure 3.9: Calorimetric measurement of heat capacity of water to determine the entropy at 298.1 Kelvin, from the work of Giauque and Stout [70].

ies/deg./mole by integrating the measured specific heat (Fig. 3.9). But such a measurement would only give the value with respect to the $T = 0$ entropy i.e.

$$\int_0^T \frac{C}{T'} dT' = S(T) - S(0), \qquad (3.34)$$

so that the zero point contribution would not appear in such an evaluation.

Pauling was able to account for this difference in values by a simple counting procedure [71]; he demonstrated that because there are two hydrogen-oxygen bond distances in ice i.e. the hydrogen-bond distance (1.81 Å) and the covalent-bond distance (0.95 Å), when ionic hydrogen-oxygen configurations are disallowed, there is a zero point entropic contribution of $S = R \log(3/2) = 0.806$ calories/deg./mole, where R is the gas constant. This value is quite close to the discrepancy between the two measured values; thus a disordered ground state in ice accounts for the discrepancy between the spectroscopic and calorimetric measurements.

Indeed by employing Pauling's counting procedure for the Ising model on the kagome lattice [60], we may obtain a value very close to that of the exactly known zero point entropy. On the kagome lattice there are 2/3 triangles per site; and because every triangle can support 8 configurations corresponding to the 2 Ising spin values per site, we must exclude the 2 ferromagnetic configurations in the

antiferromagnetic model, leaving $6/8 = 3/4$ valid configurations. Hence for N lattice sites with 2^N total configurations, the allowed number of configurations $W = 2^N \left(\frac{3}{4}\right)^{2N/3}$ gives an entropy, in units of the Boltzmann constant k_B, of

$$S = \log W = \log (9/2)/3 = 0.50136\ldots \tag{3.35}$$

This is to be compared with the exact value of $0.5018\ldots$ [52]. At the saturation field, however, we will see in section 3.3.4 that the Pauling estimate is not as good as in the zero field case.

3.3.3 Ladders

In this subsection we describe the transfer matrix procedure to calculate the partition function Ω_m of a ladder with m unit cells, such that no up spin may neighbour another; the space of such configurations is denoted as C_m which comprise the degenerate ground states at h_c for L_1 and L_2 shown in Fig. 3.10. Examples of such configurations for L_1 are indicated in Fig. 3.11 at its saturation field $B_c/J = 3$. We illustrate the procedure with the case of ladder L_3 of Fig. 3.10 where a unit cell is taken to be a simple triangle; this will be relevant while building up the kagome lattice from this ladder. We emphasize that,
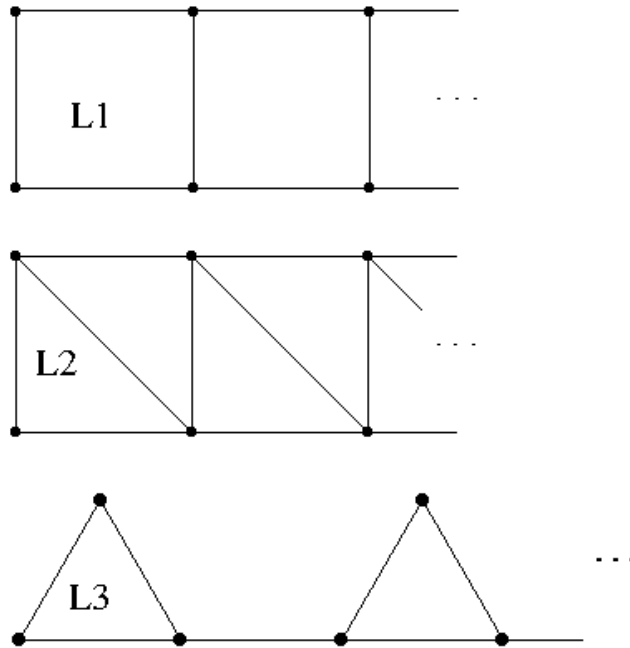

Figure 3.10: Quasi one-dimensional lattices (ladders) L_1, L_2, L_3. L_3 in a triangular lattice pattern reproduces the kagome lattice.

for this particular ladder L_3, the configurations in C_m do not constitute the degenerate space of states at the critical field because the number of nearest neighbours for sites along the base and for those on the apices are not the same. But the same procedure may be adopted for $S^{\text{sat.}}$ calculations for L_1 and L_2. L_3 may thus be thought of as a simple linear chain, with the provisos that (a) now 4 states are permitted on each 'site' i.e. $C_1 = \left[\text{\tiny{△}}, \text{\tiny{△}}, \text{\tiny{△}}, \text{\tiny{△}} \right]$, and (b) the third of these states may not follow the second of these states on the chain. Following Metcalf and Yang [64], the transfer matrix for the present

Table 3.2: Partition function in configuration space C_m for m−site (cell) Ising chain (ladder L_3) with periodic and free boundary conditions; values for $m = 1, 2, 3$ (which exclude the boundary spins/cells for free boundaries) are indicated.

Boundary	Ising chain	Ladder L_3
Periodic	$\left(\dfrac{1 + \sqrt{5}}{2}\right)^m + \left(\dfrac{1 - \sqrt{5}}{2}\right)^m = 1, 3, 4, \ldots$	$\left(2 + \sqrt{3}\right)^m + \left(2 - \sqrt{3}\right)^m = 4, 14, 52, \ldots$
Free	$\dfrac{1}{\sqrt{5}}\left[\left(\dfrac{1+\sqrt{5}}{2}\right)^{m+2} - \left(\dfrac{1-\sqrt{5}}{2}\right)^{m+2}\right] = 2, 3, 5, \ldots$	$\dfrac{1}{2\sqrt{3}}\left[\left(2 + \sqrt{3}\right)^{m+1} - \left(2 - \sqrt{3}\right)^{m+1}\right] = 4, 15, 56, \ldots$

case may be defined as

$$M_{L_3} = \begin{pmatrix} 1 & 1 & 1 & 1 \\ 1 & 1 & 0 & 1 \\ 1 & 1 & 1 & 1 \\ 1 & 1 & 1 & 1 \end{pmatrix},$$

where a zero entry indicates the aforementioned disallowed sequence of states. Under periodic boundary conditions, the total number of states is given by the trace of the transfer matrix over the m cells [64]. That is

$$\Omega_m^{\text{PBC}} = \text{Tr}\left[(M_{L_3})^m\right] = \left(2 + \sqrt{3}\right)^m + \left(2 - \sqrt{3}\right)^m. \tag{3.36}$$

Note that the trace automatically disallows the reverse of condition (b) i.e. $C_1(2)$ not following $C_1(3)$ through the chain ends; thus the non-Hermiticity of M_{L_3} poses no issues. We treat the boundary

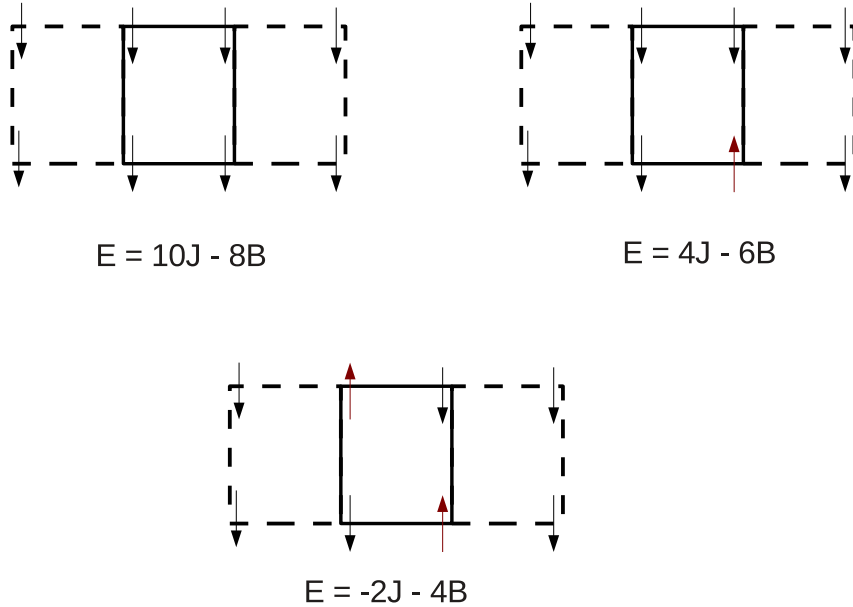$$E = 10J - 8B \qquad\qquad E = 4J - 6B$$

$$E = -2J - 4B$$

Figure 3.11: Degenerate configurations of ladder L_1 at the saturation field $B = h_c = 3J$; at this point, the energy equals $E = -14J$. Dotted lines indicate the boundary cells where no spin has been flipped and flipped spins are shown in red pointing upwards.

conditions on a more general footing by solving for the characteristic polynomial of M_{L_3} to give $\lambda^2(\lambda^2 - 4\lambda + 1) = 0$, from which the difference equation relating the partition function Ω_m of $m-$cell ladders may be readily read off as

$$\Omega_m = 4\Omega_{m-1} - \Omega_{m-2}, \tag{3.37}$$

for both periodic and free boundary conditions, for each of which we merely have to set different initial conditions in (3.37). The partition functions of C_m with both boundary conditions are compared with that of the Ising linear chain at saturation in table 3.2.

The entropy per cell is then given by the logarithm of the dominant contribution to Ω_m. With this, we may obtain the saturation entropies of all the illustrated ladders in Fig. 3.10. The values and the generating difference equations are tabulated in table 3.3. For ladders L_1 and L_2, the computed values are indeed the saturation field entropies. The addition of diagonal bonds, in proceeding from the former to the latter, clearly reduces the residual entropy associated per lattice site.

3.3.4 Kagome lattice

The kagome lattice, a section of which is illustrated in Fig. 3.2a, may be thought of as ladder L_3 repeated in a two dimensional triangular lattice pattern, with a 'site' now being a simple triangle labelled A, B, C in the figure. Here too, as with the ladders, the C_m space of configurations will comprise all degenerate states such that no two up spins (with the saturation field pointing downwards) may neighbour one another. Before proceeding with the calculations, we can provide upper and lower bounds for the kagome lattice's entropy at the very outset. For the lower bound, following the arguments in Ref. [64], there must be more entropy per site than the triangular lattice because the increased connectivity of the latter serves to restrict the configuration space; we have already drawn attention to table 3.3 where the reduction in entropy, while constructing L_2 from L_1, may be seen due to the addition of diagonal bonds. As regard an upper bound, following similar reasoning, clearly the kagome lattice cannot support more configurations than the ladder L_3 from which it is built. Therefore we get the inequality

$$0.3332427\ldots < S_{\text{kag.}}^{\text{sat.}}/k_B < 0.4389859\ldots \tag{3.38}$$

where the lower bound, the saturation entropy for the Ising triangular lattice, is known exactly through the solution of the hard-hexagon model [72]. Additionally, if we use Pauling's procedure as in section 3.3.2, we see that the number of allowed configurations is given by $W^{\text{sat.}} = 2^N (1/2)^{N/3}$, because only four out of eight configurations are allowed on each triangle, and we must consider only one of two triangles per unit cell. This gives

$$S_{\text{Pauling}}^{\text{sat.}}/k_B = \frac{2}{3}\log 2 = 0.46209\ldots \tag{3.39}$$

This estimate is clearly not as good as the upper bound in (3.38). The higher value indicates that there are more correlations between the triangles in this case than in the zero field case in (3.35), where the agreement with the exact value was quite good.

We adopt two approaches for estimating the convergence of the saturation entropy as a function of system size. The first follows the transfer matrix and linear scaling method of Metcalf and Yang [64], for which we also provide an alternative reformulation; and the second is the ratios method of Milošević et al. [73].

In Fig. 3.13a, we illustrate how free and periodic boundary conditions are effected for an $m \times n = 2 \times 2$ kagome system. The black (dark) bonds indicate the underlying equivalent triangular lattice; this transformation to a triangular lattice makes the remainder of the analysis tractable. The construction of

all allowed states on the 2×2 kagome system with periodic boundary conditions is shown in Fig. 3.14.

Transfer matrix: linear scaling

For a two dimensional lattice the transfer matrices are constructed as follows from the one dimensional building chains [64], which in our case are the L_3 ladders. The matrix element $M_{i,j}$ is set to 0 if the state j of an m-cell ladder cannot follow state i on an adjacent m-cell ladder; otherwise the matrix element is 1. Clearly the matrix is of size $\Omega_m \times \Omega_m$, which already for $m = 6$ gives a little over 7 million matrix elements in M. The partition function is then given as before by $\Omega_{m,n} = \text{Tr}\,[M^n]$ for the $m \times n$ system, with n being the number of m-cell ladders; as we will see, typically $n = 100$ gives a good estimate up to three to four decimal places for the entropy. To obtain the entropy per m-cells, it is assumed that every
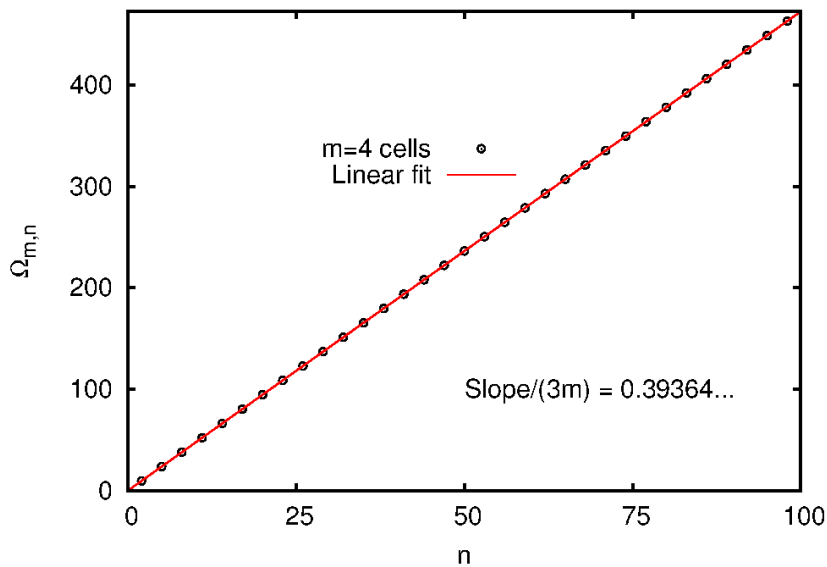

Figure 3.12: Scaling of logarithm of partition function (3.40) as a function of number of ladders n for $m = 4$ triangles per ladder. The slope gives the entropy per m triangles.

new ladder added to the finite system multiplies the system's degeneracy by a constant factor of α, so that

$$\log \Omega_{m,n} = n \log \alpha + C_{m,n}, \tag{3.40}$$

gives the entropy per m cells as $\log \alpha$, where the $C_{m,n}$ denote the correction terms. Such a linear scaling for $m = 4$ is shown in Fig. 3.12 as a function of the number of ladders n. The slope of the linear fit gives the entropy per m cells. It is expected that these terms decrease for increasing m, n values. Thus the procedure is to calculate $\Omega_{m,n}$ and use the linear fit against n to extract the entropy as per (3.40). We show in Fig. 3.13b with full and dashed red lines the convergence of the entropy as the number of triangles m is varied for periodic and free boundary conditions, keeping $n = 100$. Note that the trace operation automatically imposes periodic boundary conditions along the n-direction. Moreover we have checked for a system with free boundary conditions along the n-direction as well (using Binder's algorithm in section 3.3.4) that the values obtained, and hence the convergence trends, are essentially the same. And as observed in Ref. [73] for other lattices, free boundary conditions does not give rapid convergence using (3.40).

As noted in the previous section (see (3.37) or table 3.2 for instance), the degeneracies may also

Table 3.3: Residual entropies per site, in units of k_B, in the configuration space C_m for the lattices in Fig. 3.10 and Fig. 3.2a. The difference equations for the ladders are independent of the boundary conditions but the total number of states changes for each *finite* segment.

Lattice	Difference equation	Entropy
L_1	$x_n = 7x_{n-1} - 7x_{n-2} + x_{n-3}$	$\frac{1}{4}\log(3 + 2\sqrt{2}) = 0.440686\ldots$
L_2	$x_n = 5x_{n-1} - 2x_{n-2} + x_{n-3}$ $\quad \frac{1}{4}\log\left[5 + \left(\frac{187-9\sqrt{93}}{2}\right)^{1/3} + \left(\frac{187+9\sqrt{93}}{2}\right)^{1/3}\right] - \frac{1}{4}\log 3 = 0.382245\ldots$	
L_3	$x_n = 4x_{n-1} - x_{n-2}$	$\frac{1}{3}\log(2 + \sqrt{3}) = 0.438985\ldots$
Kagome	-	0.393589(6)

be generated by solving difference equations on the lattice subject to appropriate initial values. For the kagome lattice, a difference equation for each m is obtained and solved to obtain identical results as in Fig. 3.13b. However this alternative and equivalent approach to Metcalf and Yang's procedure of matrix multiplication followed by the trace operation retains, at the present time, no computational gain because determining the characteristic polynomial of a matrix (which determines the difference equation) is about as hard as matrix multiplication with today's algorithms [74].

Transfer matrix: ratios

In the ratio method, the correction terms $C_{m,n}$ are substantially reduced by using a sequence of estimators for the entropy as [73]

$$S_{m,n} = \log\left[\left(\frac{\Omega_{m+1,n+1}}{\Omega_{m+1,n}}\right)\left(\frac{\Omega_{m,n}}{\Omega_{m,n+1}}\right)\right]. \tag{3.41}$$

For relatively large m and n values each added chain will multiply the system's degeneracy by a factor of $\alpha = \beta^{3m}$, where β is the factor associated with each site. Then (3.41) may be seen to give the residual entropy per cell with considerable diminution of the correction terms [73].

As plotted in Fig. 3.13b with the dotted and dashed-dotted black lines, the use of (3.41) provides faster convergence for the entropy compared to (3.40); in contrast to (3.40), (3.41) seems better suited for free boundary conditions. Also shown in the figure is the value of the estimator $S_{5,100}/k_B = 0.39360$ obtained from (3.41) with free boundary conditions (using Binder's algorithm in section 3.3.4), which differs from the $(\log\alpha)_{5,100}$ value obtained from (3.40) with periodic boundary conditions by approximately 0.00001, thus giving three certain decimal places with an uncertainty in the fourth.

Binder's algorithm

We have seen in the preceding section that free boundary conditions along with (3.41) provide a rapidly convergent sequence for the entropy. The main limitation was however the calculation of $\Omega_{m,n}$ for large $\{m, n\}$ values. This may be achieved by employing Binder's algorithm towards an exact evaluation of the partition function of finite lattice systems [75]. To briefly recapitulate the procedure, the partition function of a system of size $\{m, n\}$ is expressed in terms of the degeneracies $\gamma_{m,n}(i)$ of the nth ladder in its ith state. Then clearly

$$\Omega_{m,n} = \sum_i \gamma_{m,n}(i). \tag{3.42}$$

$\Omega_{2,2} = 186$
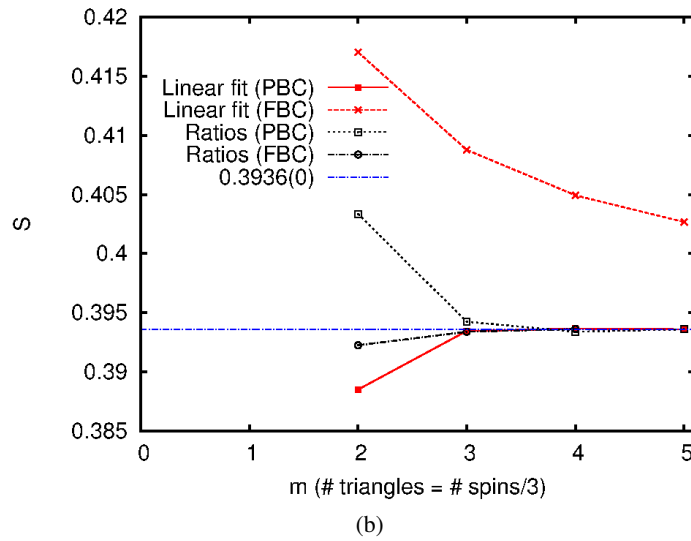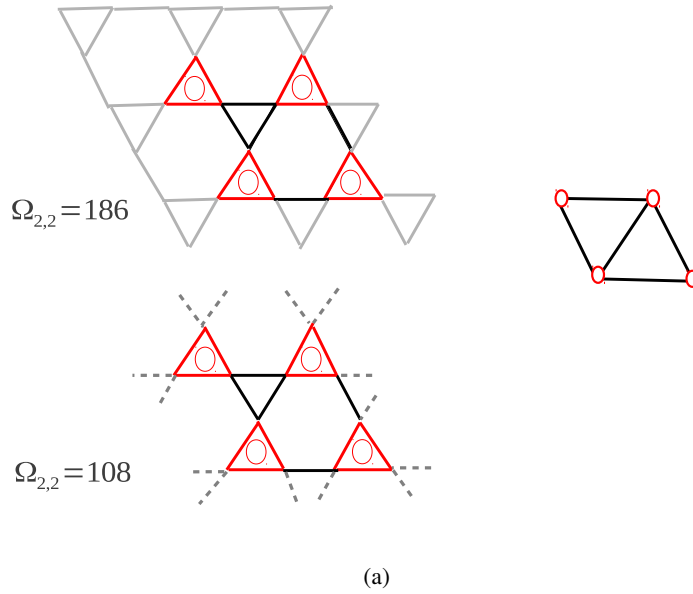
$\Omega_{2,2} = 108$

(a)

(b)

Figure 3.13: (a) Free and periodic boundary conditions (FBC, PBC) for the kagome lattice using an $m \times n = 2 \times 2$ system. Upper figure shows FBC: grey (light) triangles indicate spins aligned with the field, red (circled) triangles have finite degeneracies, black (dark) lines indicate the bonds constituting the triangular lattice. Bottom figure shows PBC with grey (dashed) lines indicating the imposition of periodicity. The partition function for each case and the equivalent triangular lattice are also indicated. (b) Scaling of residual saturation entropy, in units of k_B, on the Ising kagome lattice as function of number of triangles for two different scaling and boundary conditions. m denotes the number of unit cell triangles on each ladder, and the number of such ladders $n = 100$.

Now the degeneracies of an added ladder for the $\{n, m + 1\}$ system may be recursively computed by

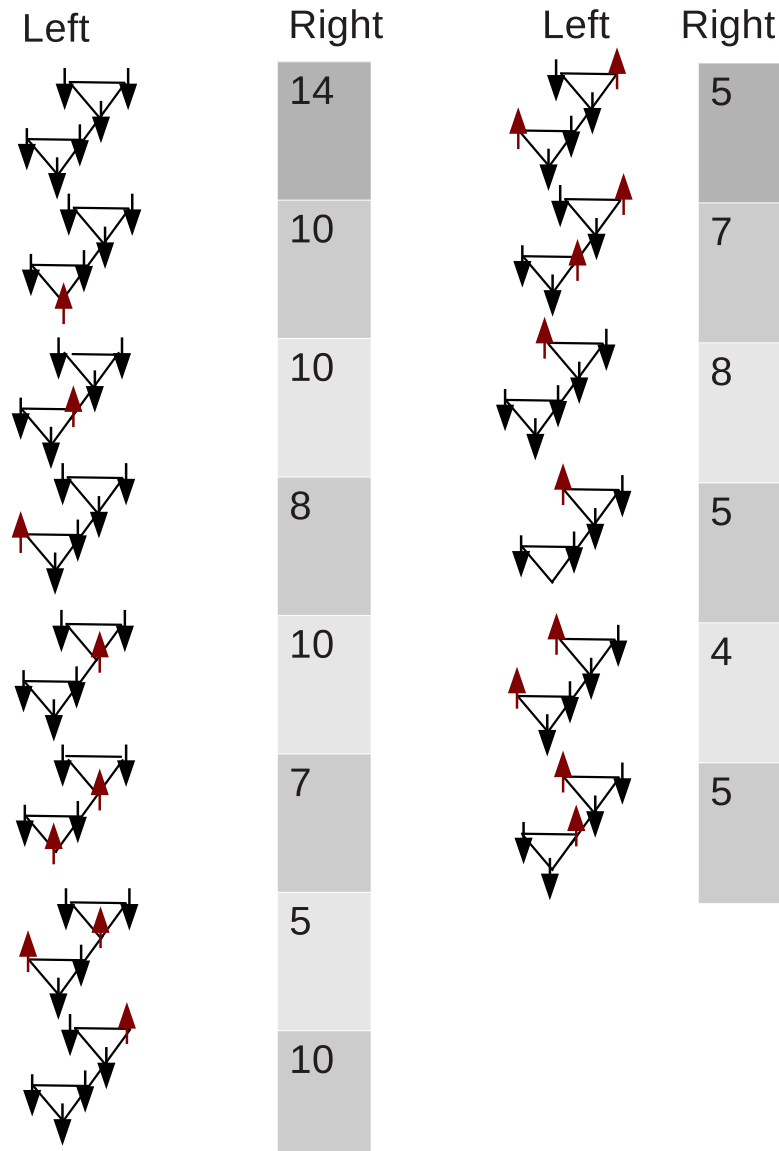$$\gamma_{m,n+1}(i) = \sum_{i'} \gamma_{m,n}(i'), \tag{3.43}$$

Figure 3.14: Number of allowed configurations on the right ladder for each configurations on the left ladder for a 2x2 kagome system with periodic boundary conditions.

with the summation running over only those values of i' such that state i may be adjacent to it. With this, we have computed the partition function of over 1300 spins with modest computational effort. For instance, we are able to reproduce up to 10 digits in the residual saturation field entropy value for the square lattice [73] using twenty 10-rung L_1 ladders.

Using (3.41), (3.42) and (3.43) we compute $S_{6,50}$, $S_{7,50}$ and $S_{8,50}$ to give six stable digits for the kagome lattice saturation field entropy

$$S_{\text{kag}}/k_B = 0.393589(6). \tag{3.44}$$

We compare this with low temperature Monte Carlo simulation results and the Bethe approximation for pyrochlore spin ice which, at the saturation field, may be described by a two-dimensional network of Ising pseudo-spin kagome lattice [56]. Scaling the saturation field results of Isakov et al. by a factor of 4/3 (because the corner spin in the pyrochlore tetrahedron is considered frozen giving a high temperature entropy per site of only $\frac{3}{4}k_B \log 2$), we obtain the relevant results, in units of k_B, to be

$$S_{\text{kag.}}^{\text{MC}}(T/J = 0.15) \approx 0.397,$$
$$S_{\text{kag.}}^{\text{Bethe}} \approx 0.38772.$$

Converting the entropy in (3.44) to that of spin ice close to the saturation field (multiplying by $3R/4$, where R is the gas constant), we get the saturation entropy in the spin-ice compound to be approximately 2.4544 Joules/deg./mole Dy, which is larger than the value of approximately 2.1 Joules/deg./mole Dy from the experimental data shown in Fig. 3.8b for the first prominent peak appearing at 1 K. The difference between this value and the result in (3.44) is then approximately 0.08 calories/deg./mole Dy. We expect that experimental data with measurement errors or, as suggested in Ref. [56], more data points in the measurements providing greater resolution of the peak close to the transition will afford even better comparison with our value. If not, we repeat our remarks made in this context in section 3.3.2 that this indicates the need for more than two dimensional Ising physics close to the compound's saturation field.

3.4 Conclusions

We have examined exactly the spectral properties of non-interacting lattice models through the formalism of lattice Green's functions. We computed the density of states of three related lattices: the kagome, diced (dual of the kagome) and the three dimensional hyperkagome. For the hyperkagome lattice, however, we are able to reduce the obtained integral to a form approximately like Glasser's canonical form for Green's functions of other standard lattices but with some additional terms that appear to destroy integrability. Due to the relatively succinct functional form obtained for the said integral and the numerical correspondence of this result with other purely numerical evaluations for the density of states, we believe that it might be plausible to obtain a closed form solution. Exact expressions for lattice density of states ought to be useful in dynamical mean field theory calculations [40] and for understanding the non-interacting or weakly interacting limits better. Using the density of states of the kagome lattice we are able to show an abrupt jump in the density setting in at the transition from an empty lattice to a 1/3 filling, possibly signalling a first order transition; the corresponding transition is a smooth one for the square and triangular lattices.

In the opposite limit of no hopping, we considered the degenerate space of states of a few Ising ladders and the Ising kagome lattice at the saturation external field. For the ladders, by a simple redefinition of a site, the residual entropy was exactly computed using a transfer matrix method. We treated the generation of states for periodic and free boundary conditions on a general footing by the use of difference equations.

For the kagome lattice, we were able to provide six stable digits for the residual entropy by calculating the exact partition function of over 1300 spins using Binder's algorithm implemented on a standard computer. Our accurate result compares reasonably with approximate results from low temperature Monte Carlo simulations and the Bethe approximation for an equivalent system. The difference from experimental measurements of the entropy of the spin-ice compound $Dy_2Ti_2O_4$ close to its saturation field,

where Ising physics on kagome planes was argued to hold [56], is approximately 0.08 calories/deg./mole Dy. The independent triangle approximation of Pauling's gives an overestimate for the saturation field entropy for the Ising kagome, indicating that inter-triangle correlations are indeed significant at this transition point. We suggest that by constructing appropriate ladders, in conjuction with Binder's algorithm, exact partition functions of similar physical models on geometrically complex lattices may be accurately computed with more ease after their transformation to standard lattice structures.

Acknowledgements

Lattice soft-core bosons

4.1 Bose-Hubbard and cold atoms: a perspective

The proposal of describing the dynamics of an ultra-cold dilute gas of bosonic atoms by the Bose-Hubbard Hamiltonian (4.1) was put forward about 15 years ago [76]. In addition, the zero-temperature quantum phase transition from the Mott-insulating phase to the superfluid phase (identified by the breaking of U(1) symmetry or the presence of off-diagonal-long-range-order) was analysed in terms of varying the potential depths of the optical lattice. A few years later this was followed by an experimental demonstration of this transition [77] in a three-dimensional optical lattice at temperatures very close to absolute zero. The long-range phase coherence in the condensed phase and the localization of particles in the insulating phase were two of the smoking guns that demonstrated the ability to switch controllably between the two ground states. The Bose-Hubbard Hamiltonian (BHH) is described by

$$H = -t \sum_{<i,j>} (b_i^\dagger b_j + \text{h.c.}) + \frac{U}{2} \sum_i \hat{n}_i(\hat{n}_i - 1) - \mu \sum_i \hat{n}_i. \tag{4.1}$$

where h.c. refers to Hermition conjugate and the $b_i^\dagger$ and b_i are bosonic creation and annihilation operators satisfying the commutation relations

$$\begin{aligned}
\left[b_i, b_j\right] &= \left[b_i^\dagger, b_j^\dagger\right] = 0, \\
\left[b_i, b_j^\dagger\right] &= \delta_{i,j}, \tag{4.2}
\end{aligned}$$

and δ is the Kronecker delta function. $\hat{n}_i = b_i^\dagger b_i$ is the number operator, the hopping terms with amplitude t are between nearest neighbours, and the system consists of a single species of soft-core bosons satisfying (4.2). The local energy term U contributes to a repulsive on-site interaction between bosons.

The phase diagram and phase transitions of the BHH were initially investigated [78] using a mean-field approach; in the pure system, the authors identified two ground state phases, and the multicritical point between the phases where particle-hole symmetry (originally absent in (4.1)) was restored. At which phase point, the system was argued to be in the same universality class as the $(d+1)$ dimensional *XY* model (see figure 4.1). For $d = 1$, the transition is of a special nature known as the Berezinskii-Kosterlitz-Thouless transition [79, 80] and is realized in diverse experimental situations [81]: dielectric
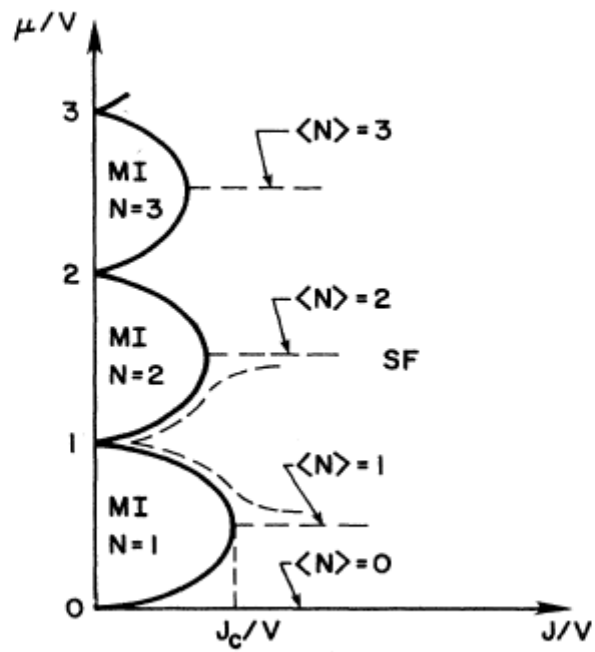
Figure 4.1: Zero-temperature mean field phase diagram as investigated with $J = t$ and $V = U$ in equation (4.1). Figure taken from Ref. [78].

plasma transition of the classical Coulomb gas, transition between the normal fluid and He^4 superfluid, the transition from a flat to rough interface in the solid on solid model, and so on. The phase diagram basically consists of a series of Mott-insulating lobes separated from the condensed phase; each lobe is a measure of the commensurability (integer-filling factor) of the system. Many of these arguments were set on a much firmer footing by density matrix renormalization group techniques and strong coupling expansions in t/U [82–84].

The two phases

The superfluid transition at the tip of each lobe (the multicritical point) is fundamentally different compared to a transition across a generic point. At a generic point, the transition is driven by density-fluctuations with a continuous change in the particle (hole) density. But at the multicritical point, the physics is quite different: here the density does not change, but a sufficiently large t value enables the bosons to overcome the on-site repulsion and hop throughout the system anyhow, thereby forming phase coherence. The closing of the gap δ_g (not to be confused with the Kronecker delta function of (4.2)) across the Mott boundary can be expressed as,

$$\delta_g \sim (t_c - t)^{z\nu}. \tag{4.3}$$

We will see that $z\nu < 1$ at this special point. At a general point on the lobe, the action reduces to the path-integral representation of a fluid of interacting bosons in the continuum, with the fluid roughly corresponding to the gas of excess quasiparticles (or quasiholes) which are present when the density deviates slightly from the commensurate values [85]. As the phase boundary at a general point in the lobe is approached, the gap will vanish linearly in $t_c - t$.

The lobe structure

We will now give physical arguments [78, 83] as to why the $\mu - t$ phase diagram should produce the above structure. Starting from the atomic limit ($t = 0$), we see that the on-site energy is minimized if each site has n (integer) number of bosons per site

$$E_{\text{Mott}}^{(0)}/N = \frac{U}{2}n(n - 1) - \mu n. \tag{4.4}$$

When $n - 1 < \mu/U < n$ (for $n > 0$), there are exactly n bosons per site. This can be seen if we consider adding a single particle or hole to the system; the costs in energy, respectively, are

$$E_{\text{particle}}^{(0)} = Un - \mu, \tag{4.5}$$

$$E_{\text{hole}}^{(0)} = -U(n - 1) + \mu. \tag{4.6}$$

When we go away from the atomic limit and consider single particle (hole) excitations, due to the finite hopping, these excitations will generate a spectrum of dispersion depending on the quasimomentum vector; the respective costs (gaps) in energy will be, analogous to the above,

$$E_{\text{particle}}(\mathbf{k}; t, \mu) = \epsilon_{particle}(\mathbf{k}; t) - \mu, \tag{4.7}$$

$$E_{\text{hole}}(\mathbf{k}; t, \mu) = -\epsilon_{hole}(\mathbf{k}; t) + \mu. \tag{4.8}$$

The particle (hole) sector has the lowest (highest) eigenvalue at $\mathbf{k} = 0$; these would give the minimum

gaps. And setting the left-hand sides to 0, these give us the boundaries in the $\mu - t$ plane. To expatiate on this: consider we start at any one point $X(\mu, t)$ within the incompressible Mott phase at a given density. This is a gapped phase with finite energy required to create an extra particle or hole. From this point, let us start increasing μ keeping t constant. At one point, say $Y(\mu', t)$, we can imagine that the energy gained by the hopping will exactly compensate the cost in creating the particle; thus the bosons can achieve hopping with no energy expenditure, which naturally leads to superfluidity. Y will then be a point on the upper contour, corresponding to the point X, of the Mott-phase for the given boson density. Now we increase the hopping strength which thereby increases the kinetic energies of the bosons; this will in turn aid in reaching the said compensation quicker, thereby decreasing the width of the Mott lobe. Similar arguments hold for the lower contour.

By following the above arguments we see that at some value of the hopping parameter, the two contours must meet, signalling the complete disappearance of the Mott phase. This occurs at the tip of the lobe (where particle-hole symmetry is restored). Here the transition into the compressible superfluid phase occurs at a fixed commensurate density; for one dimensional systems, this is a Luttinger liquid.

4.1.1 Quantum-classical mapping

We mentioned in the previous section that there exist special multicritical points in the transition from the insulator to the superfluid i.e. at the tip of the Mott lobes. Arguments from scaling theory [78] and conclusive demonstrations from strong coupling expansions [83, 84] indicated that these phase space points are in the universality class of the *XY* model in one dimension higher. This general principle of mapping between a quantum critical model and a classical system in higher dimension will be briefly described here; the case in point, that of the Berezeinski-Kosterlitz-Thouless (BKT) [79, 80] transition, will be connected in context.
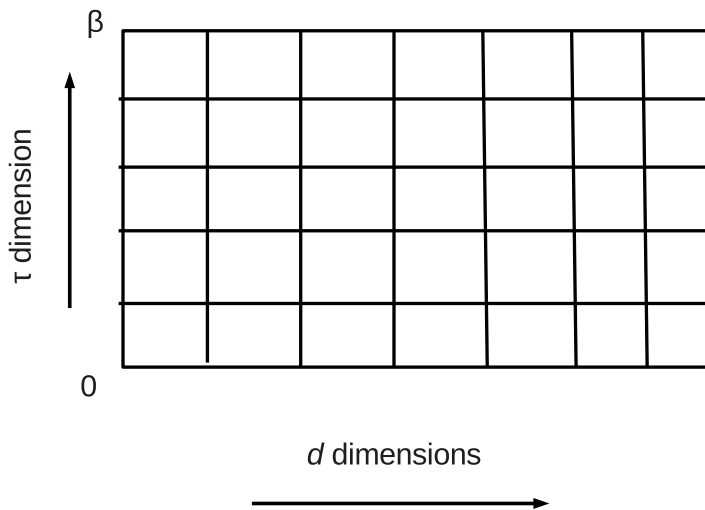

Figure 4.2: Schematic depiction of an imaginary time axis arising from strong quantum fluctuations in d dimensions at inverse temperature β. The resulting system may be analysed classically [86].

A quantum system in d dimensions will have fluctuations induced by the non-commutativity of the operators in the potential and kinetic energy terms; this effectively adds an extra dimension τ (imaginary time) to the system whose extent in this added dimension will be inversely determined by the temperature of the quantum system [86]; see Fig. 4.2. Therefore at zero temperature, the $(d + 1)^{\text{th}}$ dimension in the classical model is infinite in extent.

Consider the one dimensional ($d = 1$) quantum case for the Bose-Hubbard model; at the tip of the lobe, the universality class is that of the *XY* model in $D = d + z$ dimensions, where z is the dynamical critical exponent that quantifies the asymmetry between time and space coordinates. At the multicritical point $z = 1$ [78] and so the critical behaviour is governed by that of the $D = 2$ *XY* model, which has a continuous $O(2)$ symmetry. This system is known to possess a vortex binding-unbinding infinite order BKT transition [79, 80], therefore such a transition is also expected in the $d = 1$ Bose Hubbard system.

However it must be noted that d-dimensional quantum models can still possess d-dimensional classical physics in the vicinity of the $T > 0$ phase transitions if they are driven by *thermal* fluctuations. For instance the BKT transition of a two dimensional classical *XY* model at finite temperatures also governs the finite temperature phase transition of the normal liquid state (high temperature) to a superfluid state (low temperature) of two dimensional bosonic systems, which are inherently quantum mechanical. Such a transition has indeed been observed in a trapped gas of ultra-cold, degenerate rubidium atoms [87].

4.1.2 Mean-field analysis

In this section we investigate the mean-field equations governing the physics of the Bose-Hubbard Hamiltonian following the prescription in Ref. [78, 86]; we concentrate on the $\rho = 1$ Mott lobe and employ second order perturbation theory to expand the ground state energy density E_0 of the Mott insulator as a Landau-type functional in an order parameter ϕ_{B}.

With the introduction of the complex field ϕ_{B}, the $U(1)$ symmetry of the Hamiltonian (4.1) is explicitly broken; the different sites are then decoupled and the mean-field Hamiltonian may be written as

$$H = \sum_i \left(-\phi_{\text{B}} b_i^{\dagger} - \phi_{\text{B}}^* b_i\right) + \frac{U}{2} \sum_i \hat{n}_i(\hat{n}_i - 1) - \mu \sum_i \hat{n}_i. \tag{4.9}$$

Subtracting and adding (4.9) to (4.1), and taking expectation values with respect to the mean field ground state wave function, the energy density is given by

$$E_0 = E_{\text{MF}}(\phi_{\text{B}}) - tz\langle b^{\dagger}\rangle\langle b\rangle + \langle b\rangle\phi_{\text{B}}^* + \langle b^{\dagger}\rangle\phi_{\text{B}}, \tag{4.10}$$

for a lattice with z nearest neighbours. Minimizing this with respect to $\langle b \rangle$ gives the optimal value for the order parameter as $\phi_{\text{B}} = zt\langle b\rangle$. Because a second order transition occurs between the Mott insulator and superfluid [78], we use an expansion of the energy density in a Landau functional with even powers of the modulus of the order parameter as

$$E_0 = E_{00} + \alpha|\phi_{\text{B}}|^2 + O(|\phi_{\text{B}}|^4). \tag{4.11}$$

The coefficient α may be evaluated for the first Mott lobe within second order perturbation theory to be

$$\alpha = -\frac{1}{\mu} + \frac{2}{\mu - U} + \frac{1}{zt}. \tag{4.12}$$

Within Landau's theory of second order transitions, the transition may be located by setting $\alpha = 0$ in
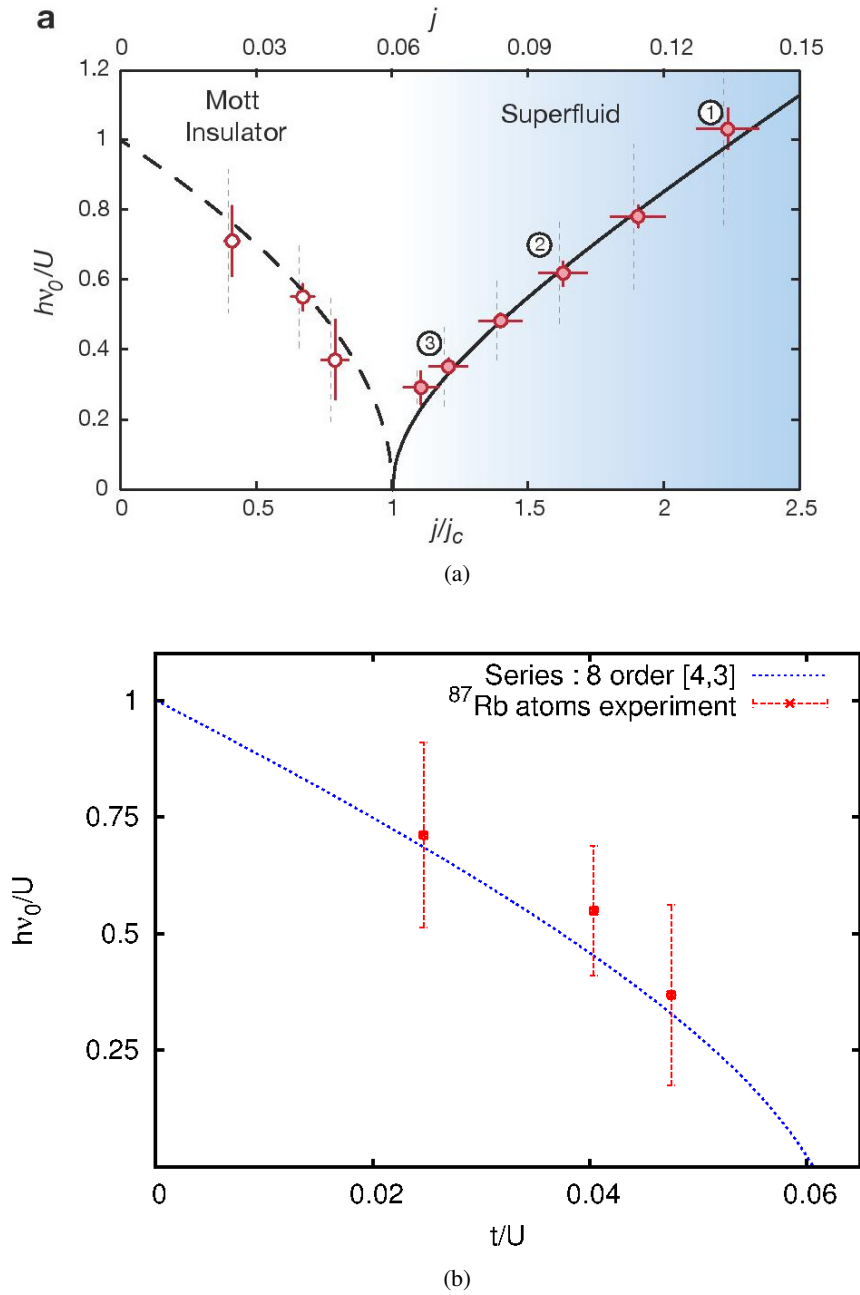
(a)

(b)

Figure 4.3: (a) Scaling of Mott gap (left circles) and the Higgs gap (right circles) as a function of the tunnelling parameter $j = t$ in (4.1). Dashed lines indicate prediction from mean field (4.14), and the vertical lines indicate full width of error function that determines the onset of spectral response. Figure taken from Ref. [88]. (b) Mott gap calculated using 8th order series expansions [7, 83] and a 4x3 Padé approximant compared with experimental data, and its maximum error, taken from Fig. 4.3a.

(4.12). Therefore the critical contours separating the Mott insulator and superfluid phase are given by

$$\mu_c^{\pm} = \frac{1}{2}\left(1 - zt \pm \sqrt{1 + z^2t^2 - 2zt - 4Uzt}\right), \tag{4.13}$$

with the ± corresponding to particles and holes respectively. At the tip of the lobe $\mu_c^+ = \mu_c^-$; this condition on a square lattice may be solved to give the critical lobe tip as $t_c^{\mathrm{MF}}/U = \dfrac{3\sqrt{2}-4}{4\sqrt{2}}$, which is approximately 28% away from the actual value obtained in Ref. [83].

The gap in the Mott phase within mean-field may be calculated from (4.13) as $\Delta^{\mathrm{MF}}(t) = \sqrt{16t^2 - 24t + 1}$, in units of U. Normalizing with respect to the mean-field critical lobe tip value, the gap may be written as

$$\Delta^{\mathrm{MF}}(t) = \sqrt{\left(1 - \frac{t}{t_c^{\mathrm{MF}}}\right)\left(1 - (17 - 12\sqrt{2})\frac{t}{t_c^{\mathrm{MF}}}\right)} \approx \sqrt{\left(1 - \frac{t}{t_c^{\mathrm{MF}}}\right)\left(1 - 0.03\frac{t}{t_c^{\mathrm{MF}}}\right)}. \qquad (4.14)$$

This gap equation was used to check against recent experimental observations of the Mott gap in an optical lattice of Rubidium-87 atoms cooled to temperatures sufficiently below the onset of melting of the Mott phase [88]. Although the location of the lobe tip within mean field is quite different from the true value, the normalized dependence of the gap as a function of the tunnelling in (4.14) gives a reasonable fit to the observed data points as seen in Fig. 4.3a taken from Ref. [88]. We have also indicated a Padé approximant of the gap calculated within an 8th order series expansion [7, 83] to compare with the experimental data in Fig. 4.3b; the comparison is again quite reasonable.

However we are certain that closer to the tip of the lobe, the series expansion result for the gap will provide much better comparison to the experimental situation than the mean field gap equation. As a quick way to see this, it is known that the gap closes near the tip with the critical exponent $z\nu \approx 0.69$ [78, 83] whereas within mean field, (4.14) can give only a square root exponent for the closing of the gap. The correct critical exponents may be verified with our high order strong coupling expansions [7, 84]; one of our goals, among others, in the next section will be to determine whether these exponents will be modified by the inclusion of higher body interactions in (4.1).

4.2 Higher body interactions

We calculate thermodynamic properties of soft-core lattice bosons with on-site n-body interactions using up to twelfth and tenth order strong coupling expansion in one and two dimensional cubic lattices at zero temperature. Using linked cluster techniques described in chapter 2, we show that it is possible to exactly renormalize the two-body interactions for quasiparticle excitations and ground-state energy by re-summing the three and four body terms in the system, which suggests that all higher-body on-site interactions may be exactly and perturbatively re-summed into the two-body terms with this procedure. Such a procedure is applicable to a broad range of systems analysable by linked cluster expansions, ranging from perturbative quantum chromodynamics to spin models. Universality at various three-body interaction strengths for the two dimensional Bose-Hubbard model is checked numerically.

The first calculation of the effect of three-body interactions in lattice bosons [89] for liquid He^4 and solid He revealed its negligible effect on its ground state energy. However, it was recently suggested [90] that, firstly, three-body interactions in cold polar molecules could be naturally modelled by Hubbard Hamiltonians with nearest-neighbour three-body terms and, secondly, there might arise plausible new phases in experimental setups of degenerate quantum molecular gases. The authors of Ref. [90] showed that for polar molecules, such as LiCs with a permanent dipole moment of 6.3 Debye, such an inter-site interaction was indeed significant. Moreover many experiments have produced a gas of ultra-cold polar molecules e.g. in Ref. [91], polar RbCs molecules were reported to be produced via photoassociation of the individual rubidium and caesium atoms.

Shortly thereafter, a decoupling mean-field (MF) approximation was used to investigate the critical

properties of a Bose-Hubbard model with *on-site* three-body interactions [92]. That such on-site terms could effectively arise in two-body collisions of atoms confined to optical lattices was only subsequently justified [93]. Given the already present controllability of *n*-body interactions in experiments of ultracold gases, we anticipate that rapid progress in tuning on-site *n*-body interactions in these systems to be achieved considerably soon. Therefore, we will use a strong coupling expansion - with no finite size effects in the thermodynamic limit - of the on-site three and four body interacting Bose-Hubbard model, in addition to checking the universality hypothesis at *XY* critical points for various three-body strengths. A procedure for incorporating higher body interactions by renormalizing the two-body problem will also be described in this chapter.

Consider a system of two-body and higher-body interacting bosons on the one dimensional chain and two dimensional square lattices described by the Bose-Hubbard Hamiltonian

$$H = -t \sum_{<i,j>} (b_i^\dagger b_j + \text{h.c}) + \frac{U}{2} \sum_i \hat{n}_i(\hat{n}_i - 1) + \sum_{k=3} \frac{U_k}{k!} \sum_i \prod_{l=0}^{k-1} (\hat{n}_i - l) - \mu \sum_i \hat{n}_i. \qquad (4.15)$$

where the operators have the same meaning as in (4.1) and $U_k > 0$ is the strength of *k*-body on-site interaction terms and μ is the chemical potential. The on-site term U will be the energy scale of choice in the rest.

The Hamiltonian in (4.15), when represented in the form $\mathcal{H} = \mathcal{H}_0 - \lambda \mathcal{H}_1$ with $\mathcal{H}_1$ being the hopping terms of strength $\lambda = t/U$ and $\mathcal{H}_0$ being the rest of (4.15), is amenable to linked cluster expansions [6, 83] in the parameter λ. Evaluation of physical properties, like energy, are performed via Rayleigh-Schrödinger perturbation theory [13] and the linked cluster expansion. Excited states can be obtained using a similar procedure through Gelfand's similarity transformation [6] explained in section 2.2.2.

4.3 3-body interactions

4.3.1 One dimensional systems

Consider first the $\rho = 1$ Mott insulating lobe in the one dimensional chain. For a twelfth order bond-expansion, there are 13 distinct topological graphs (clusters) that can be embedded on the infinite chain: approximately 2.5 million states contribute to the full Hilbert space with a maximum of 13 states in the lowest degenerate manifold. From MF calculations [92, 94], it was predicted that the first Mott lobe should not change in structure, which may readily be seen by our mean field analysis in section 4.1.2; this conclusion was later systematically corrected by density matrix renormalization group (DMRG) calculations [95, 96] and exact diagonalization [97]. Using Gelfand's similarity transformations to construct the particle and hole excitations, we identify the disappearance of the excitation gap as defining the second-order transition contours of the lobe [83].

For instance, consider the creation of a hole excitation in the simplest case $U_3 = 0$ on each of the first 4 clusters for the one dimensional case. We begin with the ground state having a single boson per site $|\psi\rangle = |1, 1, 1, \ldots 1\rangle$ and evaluate the states in higher orders of perturbation theory to calculate the ground state energies. The single hole excitations for each cluster are created by removing a single boson from any of the *n* vertices of the cluster; thus there are *n* degenerate states. Then we employ degenerate perturbation theory and Gelfand's transformation [14], as described in section 2.2.2, to construct the effective Hamiltonian in this quasiparticle sector.

Following Ref. [83], the general procedure is schematically depicted in Fig. 4.4; on the left, we depict the uncoupled limit $\lambda = 0$ and the energies for particle and hole creation with respect to the ground state
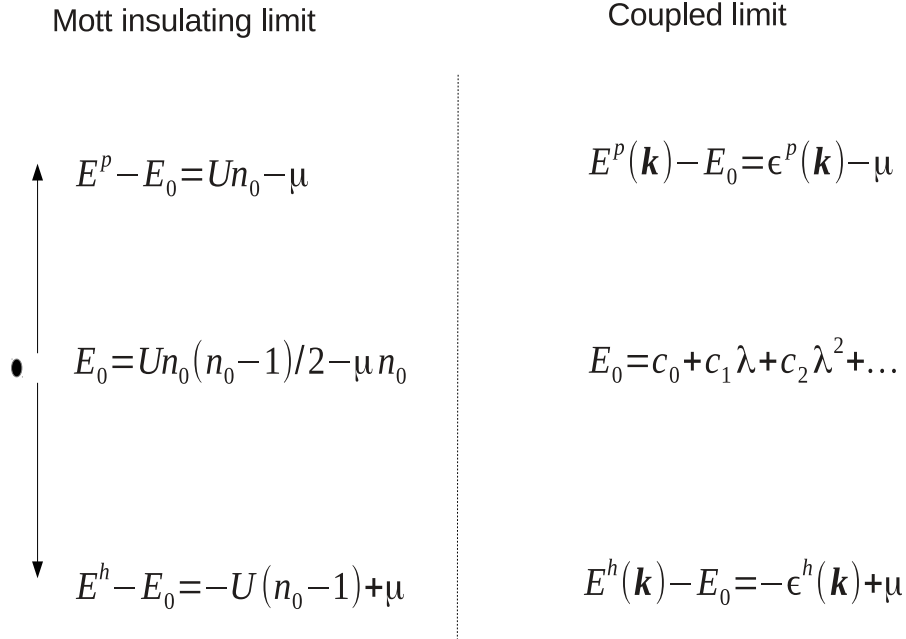
Mott insulating limit   Coupled limit

$$E^p - E_0 = U n_0 - \mu$$ $$E^p(\boldsymbol{k}) - E_0 = \epsilon^p(\boldsymbol{k}) - \mu$$

$$E_0 = U n_0 (n_0 - 1)/2 - \mu n_0$$ $$E_0 = c_0 + c_1 \lambda + c_2 \lambda^2 + \dots$$

$$E^h - E_0 = -U(n_0 - 1) + \mu$$ $$E^h(\boldsymbol{k}) - E_0 = -\epsilon^h(\boldsymbol{k}) + \mu$$

Figure 4.4: Energies of particle (p) and hole (h) excitations in the Mott insulating limit and the coupled limit ($\lambda \neq 0$) of the Bose Hubbard model. In the coupled limit, the excitation spectrum is computed via linked cluster expansion, and the critical particle-hole contours are given by $\mu_c^{p,h} = \epsilon^{p,h}(\mathbf{k} = \mathbf{0})$.

having n_0 bosons per site. Analogously, in the coupled limit with $\lambda \neq 0$, the quasiparticle/quasihole (p, h) excitation energies $\epsilon^{p,h}$ are constructed with the Gelfand transformation to a given order. The particle-hole contours of the initial state i.e. the Mott insulating state, will then be given by the condition $E^{p,h} = E_0$, or equivalently $\mu_c^{p,h} = \epsilon^{p,h}(\mathbf{k} = \mathbf{0})$. Following this prescription, the effective Hamiltonians after subcluster subtraction for hole excitations in the first four clusters on the one dimensional system are shown in Fig. 4.5.

Then we embed the clusters on the lattice points $\vec{\mathbf{r}}$ to get the following transition amplitudes on the lattice:

$$\Delta^h(0) = 8\lambda^2,$$
$$\Delta^h(1) = -2\lambda - 12\lambda^3,$$
$$\Delta^h(2) = -4\lambda^2,$$
$$\Delta^h(3) = -12\lambda^3. \tag{4.16}$$

This gives the gap to hole excitations as

$$\Delta^h(\mathbf{k} = \mathbf{0}) = \sum_{\mathbf{r}} \Delta(\mathbf{r}) = -2\lambda + 4\lambda^2. \tag{4.17}$$

Note that we have included both $\pm\mathbf{r}$ into (4.16); the energy lost by the system is then given by $-\Delta^h(\mathbf{k} = \mathbf{0})$. Similarly single particle excitations are created by adding an extra boson to the strongly interacting limit and analysing the states that contribute in higher orders of perturbation theory within the degenerate

$$1$$
$$\bullet \qquad\qquad\qquad W^{(1)} = \begin{bmatrix} 0 \end{bmatrix}$$

$$
\begin{array}{cc}
1 & 2 \\
\bullet\!\!-\!\!\!-\!\!\!-\!\!\bullet
\end{array}
\qquad\qquad
W^{(2)} = \begin{bmatrix} 4\lambda^2 & -\lambda \\ -\lambda & 4\lambda^2 \end{bmatrix}
$$

$$
\begin{array}{ccc}
1 & 2 & 3 \\
\bullet\!\!-\!\!\!-\!\!\bullet\!\!-\!\!\!-\!\!\bullet
\end{array}
\qquad
W^{(3)} = \begin{bmatrix} 0 & 6\lambda^3 & -2\lambda^2 \\ 0 & 0 & 0 \\ -2\lambda^2 & 6\lambda^3 & 0 \end{bmatrix}
$$

$$
\begin{array}{cccc}
1 & 2 & 3 & 4 \\
\bullet\!\!-\!\!\bullet\!\!-\!\!\bullet\!\!-\!\!\bullet
\end{array}
\quad
W^{(4)} = \begin{bmatrix} 0 & 0 & 0 & -6\lambda^3 \\ 0 & 0 & 0 & 0 \\ 0 & 0 & 0 & 0 \\ -6\lambda^3 & 0 & 0 & 0 \end{bmatrix}
$$

Figure 4.5: First four clusters on the one dimensional chain and the corresponding effective Hamiltonians matrices in the single hole sector for the Bose Hubbard Hamiltonian.

subspace of quasiparticle excitations. This gives the energy added to the system, denoted as $\Delta^{\mathrm{p}}(\mathbf{k} = \mathbf{0})$. We identify the complete disappearance of the Mott lobe as when the energy gained by the system equals the energy lost from the single particle excitations i.e. the onset of gapless excitations being signalled by the condition $\Delta^h + \Delta^p = 0$.

We have thus evaluated a finite series for the gap at finite U_3 values up to twelfth order. To illustrate, for $r_3 \equiv \dfrac{U_3}{U} = 1$, the Mott gap $\delta_1^{\mathrm{1D}}(\lambda, \mathbf{k} = \mathbf{0})$, listing the first eight terms, is given by

$$
\begin{aligned}
\delta_1^{\mathrm{1D}}(\lambda, \mathbf{k} = \mathbf{0}) \;=\; & 1 - 6\lambda + 6\lambda^2 + \frac{20}{3}\lambda^3 - \frac{46}{27}\lambda^4 + \frac{30751}{243}\lambda^5 \\
& - \frac{185083}{324}\lambda^6 + \frac{464023295}{157464}\lambda^7 - \frac{68401014192209}{3769688160}\lambda^8,
\end{aligned}
\tag{4.18}
$$

where $\mathbf{k}$ is the lattice momentum and the subscript indicating the r_3 value. In order to get the particle-hole contours of the Mott lobe, the gap δ^{1D} close to the BKT transition is fitted by [84]

$$
\delta^{\mathrm{1D}} \propto \exp\left(\frac{1}{\sqrt{t_c - t}} \right), \qquad |t - t_c| \ll 1,
\tag{4.19}
$$

where t_c is the critical t value at the tip of the Mott insulating lobe.

In Fig. 4.6 we show particle and hole contours obtained by multiple precision Padé approximation
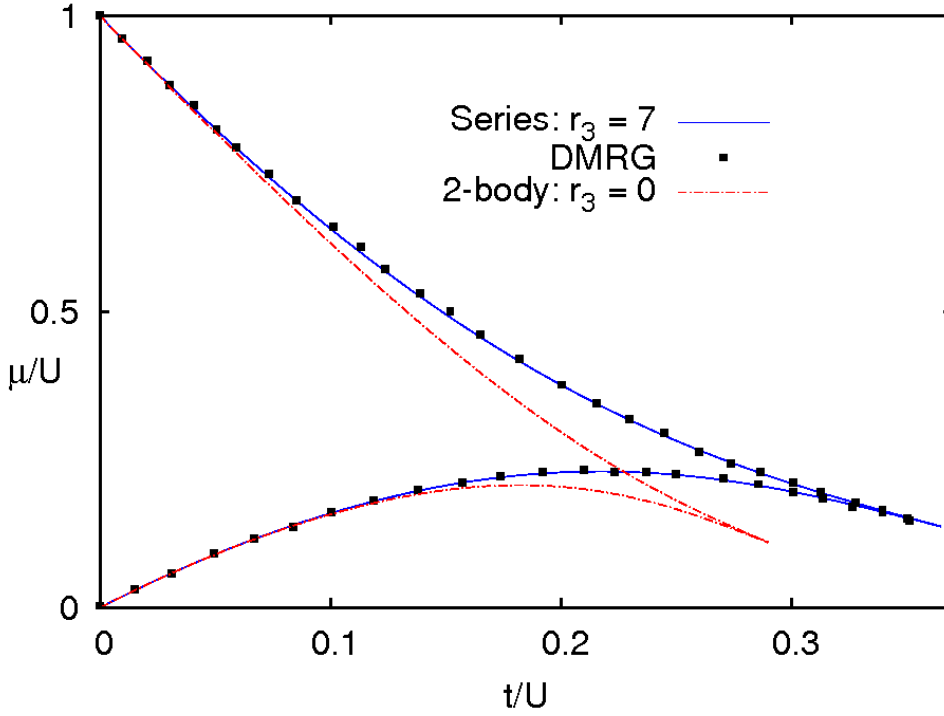
Figure 4.6: First Mott lobe in the ground state phase diagram of the one dimensional Bose-Hubbard model with $r_3 \equiv \dfrac{U_3}{U} = 0,7$; the last Padé approximant [6/6] or [5/5] of the twelfth order gap series for $r_3 = 7$ is compared with a DMRG solution [95]. [m/n] denotes an mth order numerator and an nth order denominator.

of twelfth order series and compared to a previously published DMRG solution [95] for $r_3 = 7$. The location of the critical point (BKT transition) shifts upwards and rightwards in the phase diagram, indicating an increase in the size of the first lobe and a partial restoration of particle-hole symmetry, as r_3 is increased and the semi-hardcore condition ($r_3 = \infty$) is reached. We have verified this tendency with $r_3 = 0, 1, 7, 100$. For the hardcore condition, the critical μ/U (U now being the nearest neighbour repulsion) equals exactly 1 [98], with the particle-hole symmetry completely restored.

We note that in an n-th order bond expansion for the linear chain, we need calculate the n-th order particle and hole contributions only up to graphs with $n - 1$ bonds: the effective Hamiltonian for the last cluster may be calculated with very little effort because, within the degenerate subspace of this graph, the only contributing process will be the one which transfers the excitation from one end of the chain to the other. These matrix elements will simply be given by the negative of the Schroeder numbers $S = \{1, 2, 6, 22, 90 \cdots\}$ with the generating function [99]

$$G(x) = \frac{1 - x - \sqrt{1 - 6x + x^2}}{2x}. \tag{4.20}$$

That is, for a cluster with n-bonds the nth order effective Hamiltonian has its non-zero elements given by $H(0, n) = -S_{n-1}$, for $l \geq 2$. This is independent of r_3 and the type of excitation.

4.3.2 Two dimensional systems

In two dimensions there are 680 topologically distinct clusters contributing at tenth order for a bond-expansion. Here the Mott gap δ^{2D} closes as [78]

$$\delta \propto (t_c - t)^{z\nu}, \qquad |t - t_c| \ll 1, \tag{4.21}$$

assuming the universality of the *XY* model: t_c is the value of the hopping element at the multicritical point where particle-hole symmetry is restored (here $z = 1$), z and ν are the dynamical and coherence length critical exponents respectively. To investigate the effect of three-body terms in 2D, we have calculated tenth order series for the $\rho = 1$ Mott gaps for $r_3 = 1, 10, 100$. For instance, the gap for particle-hole excitations for $r_3 = 1$ is given by

$$
\begin{aligned}
\delta_1^{2D}(\lambda, \mathbf{k} = 0) \;=\; & 1 - 12\lambda - 20\lambda^2 - \frac{760}{3}\lambda^3 - \frac{13292}{9}\lambda^4 - \frac{1984952}{81}\lambda^5 - \frac{17531713847}{83106}\lambda^6 \\
& - \frac{865220249311001}{236852100}\lambda^7 - \frac{2490980522841535381633}{72295550743500}\lambda^8 \\
& - \frac{3120130219242234405759938683}{4903807206931605000}\lambda^9 \\
& - \frac{546869669805017706229129075047268927}{83023260614404223480640000}\lambda^{10}.
\end{aligned}
\tag{4.22}
$$

From these series', t_c and $z\nu$ may be extracted by proceeding, *mutatis mutandis*, as outlined in previous scaling analysis [83]: (a) by linearly extrapolating the roots of the truncated gap series' from, say, fourth to tenth order and (b) by Padé approximating the gap series' to mimic the expected δ behaviour in (4.21); see the method of DLogPadé approximation in section 2.4.1 for details.

The results of the higher approximants ([4/4], [4/5], [4/6], [5/4], [5/5]) and linear extrapolation are tabulated in table 4.1 for four r_3 values: it must be noted that large r_3 values may be attained, as suggested in Ref. [93], using Feshbach resonances and tuning the lattice potential. As can be noted from the table that the change in t_c upon increasing r_3, and hence the structure of the first lobe, is not as substantial for the square lattice as was seen for the one dimensional case. From the ν values for the four three-body interaction strengths, we see that universality does indeed seem to hold at the *XY* point; moreover, we note that the error values will become more conservative when all the Padé approximants are considered. The corresponding classical critical coefficient for the three dimensional *XY* model is $\nu = 0.67155 \pm 0.00027$ [100].

Table 4.1: Critical points and exponents for the two dimensional square lattice boson Hubbard model at various three-body interactions r_3 using roots extrapolation (E) and Padé approximations (P). See text and Ref. [83] for the exact procedure. At $t = t_c$, $z = 1$ [78].

r_3	$t_c^E(10^{-4})$	$t_c^P(10^{-4})$	$\nu(10^{-3})$
0	597.4 ± 0.4	599	690
1	603.8 ± 0.8	604.69 ± 0.06	692.3 ± 0.6
10	616.7 ± 0.8	617.39 ± 0.05	695.4 ± 0.4
100	621.4 ± 0.8	621.98 ± 0.06	696.5 ± 0.5

4.4 Re-summation procedure

In general, to incorporate a second variable (like U_3) into a Hamiltonian within linked cluster expansions requires a double-expansion: the first in t/U, the second in U_3/U. Note that for a fixed value of U_3, the atomic limit energies are easily modified by U_3 and the perturbation analysis can proceed as before without the need for a two-variable perturbative treatment. However our investigations will be concerned with fully including the effects of higher body interactions for a *variable* U_3. This cannot be done easily within a linked cluster expansion as the unperturbed energies are required to be known as numeric constants to systematically compute higher order linked cluster expansions. In contrast via our re-summation procedure, higher order expansions may be generated for any U_3 value. We suggest that the procedure may also be used in a general Hamiltonian to check if a perturbing parameter may in fact exactly renormalize another; if found not to be the case, we may at least obtain an approximation, akin to the Padé approximation, of the second variable's perturbative effects.

For instance, the double-expansion of a quantity P in perturbing variables λ and r to order M and N respectively may be symbolically written as

$$P = \sum_{i}^{M} c_{1i}^{(N)} \lambda^i,$$

$$c_{1i}^{(N)} = \sum_{j}^{N} c_{2j} r^j. \tag{4.23}$$

Now M and N are finite integers but can one do better? The prescription we adopt is to re-sum the second series and evaluate $\lim_{N\to\infty} c_{1i}^{(N)}$ for every i, keeping M finite, and is implemented as follows: we first calculate the series coefficients for a given observable (like in Eq. 4.18) for a finite number of r_3 values. And because the coefficients are always rational numbers - by virtue of the perturbation theory - it only remains to find a rational function approximation to the obtained coefficients. The latter step may be easily implemented with Thiele's algorithm for continued fraction representation [24]; this was already explicated in section 2.4.2.

To summarize, the functional dependence of a coefficient at a given order on r_3 is to be captured by a rational approximation. For example, a single-expansion coefficient c_{1i}, for a given i, for some 24 values of r_3 from $0 \to 100$ were evaluated. Thiele's algorithm to find an approximating rational function $f_i(r_3) = c_{1i}(r_3)$ would generally require as many steps as there are points (here 24) to terminate and find the best fit; however, we find that in each of the evaluated coefficients, the algorithm stops exactly after a few steps because the continued fraction expansions stop. This ensures the exactness of the obtained $f_i(r_3)$. With this, the c_1's in (4.23) get fully renormalized by the re-summed c_2's.

The above procedure has been applied to renormalizing the series coefficients of the particle and hole contours in the two-body interacting one dimensional chain and two dimensional square lattice with respect to the three body terms. Let the particle and hole contours, for any r_3, be represented as

$$\pm \mu_{\pm}^c(r_3) = \sum_{i=0} c_i^{\pm}(r_3) \lambda^i. \tag{4.24}$$

For illustrating our method, we consider the $[M/N]$ rational function approximation to $c_4^-(r_3)$ in the one dimensional chain obtained from the 24 different values of r_3; these are listed in table 4.2 and are

Table 4.2: Fourth order coefficients for critical hole excitations (4.24) in the one dimensional Bose-Hubbard chain with various strengths of three body interactions r_3. Lower order coefficients are independent of r_3.

r_3	c_4^-	r_3	c_4^-
0	20	3	8
$\frac{1}{10}$	$\frac{596}{31}$	4	$\frac{44}{7}$
$\frac{1}{5}$	$\frac{37}{2}$	5	5
$\frac{3}{10}$	$\frac{196}{11}$	6	4
$\frac{2}{5}$	$\frac{292}{17}$	7	$\frac{16}{5}$
$\frac{1}{2}$	$\frac{116}{7}$	8	$\frac{28}{11}$
$\frac{3}{5}$	$\frac{16}{1}$	9	2
$\frac{7}{10}$	$\frac{572}{37}$	10	$\frac{20}{13}$
$\frac{4}{5}$	$\frac{284}{19}$	15	0
$\frac{9}{10}$	$\frac{188}{13}$	25	$-\frac{10}{7}$
1	$\frac{14}{1}$	50	$-\frac{140}{53}$
2	$\frac{52}{5}$	100	$-\frac{340}{103}$

seen to be exactly fit by the simple rational function

$$c_4^- = \frac{60 - 4r_3}{3 + r_3}, \tag{4.25}$$

as illustrated in Fig. 4.7.

Table 4.3: Re-summed series coefficients for the particle and hole contours in the one dimensional chain and two dimensional square lattice. Coefficients of lower order that are not listed are independent of r_3.

Coefficient	1D	2D
c_4^-	$\dfrac{60 - 4r_3}{3 + r_3}$	$-8\dfrac{231 + 71r_3}{3 + r_3}$
c_2^+	$2\dfrac{1 + 2r_3}{2 + r_3}$	$-4\dfrac{7 + 2r_3}{2 + r_3}$
c_3^+	$12\dfrac{2 + 2r_3 + r_3^2}{(2 + r_3)^2}$	$-24\dfrac{20 + 18r_3 + 3r_3^2}{(2 + r_3)^2}$
c_4^+	$-2\dfrac{339 + 1631r_3 + 2818r_3^2 + 2088r_3^3 + 676r_3^4 + 80r_3^5}{(2 + r_3)^3(3 + r_3)(5 + 4r_3)}$	$-4\dfrac{28497 + 71317r_3 + 70166r_3^2 + 33672r_3^3 + 7772r_3^4 + 688r_3^5}{(2 + r_3)^3(3 + r_3)(5 + 4r_3)}$

with Lattice spanning the two data columns (1D, 2D).

The same analyses were performed for the particle coefficients as well and similar conclusions hold; the re-summed coefficients are listed in table 4.3 up to fourth order. For example, in the one dimen-

sional case, $c_4^-(r_3 = 1) + c_4^+(r_3 = 1) = -\dfrac{46}{27}$, the fourth coefficient in (4.18). It is worth noting that even with coefficients for particle-hole series only up to third order, quantitatively reasonable estimates (within 10% compared to more accurate results [83]) for critical properties can be obtained as shown systematically in Ref. [84].

Ground state example

To low order, we may fully incorporate a variable three body term U_3 by hand. As emphasized, our re-summation procedure finds particular utility in carrying these calculations to higher order via a computerized procedure. To illustrate a low order calculation, consider a 3-site chain modelled by the Bose-Hubbard Hamiltonian (4.15) with $U_3 \neq 0$, carried through to fourth order in λ. We aim to calculate the ground state energy per site $\langle \psi | \mathcal{H} | \psi \rangle$, where $|\psi\rangle$ is the ground state wavefunction constructed order by order for the first Mott insulating lobe. The ground state wave function in the $\rho = 1$ Mott insulating phase may be calculated in second order to be

$$|\psi\rangle^{(2)} = \frac{\sqrt{24}\lambda^2}{3 + r_3}|030\rangle + 3\sqrt{2}\lambda^2(|210\rangle + |012\rangle), \qquad (4.26)$$
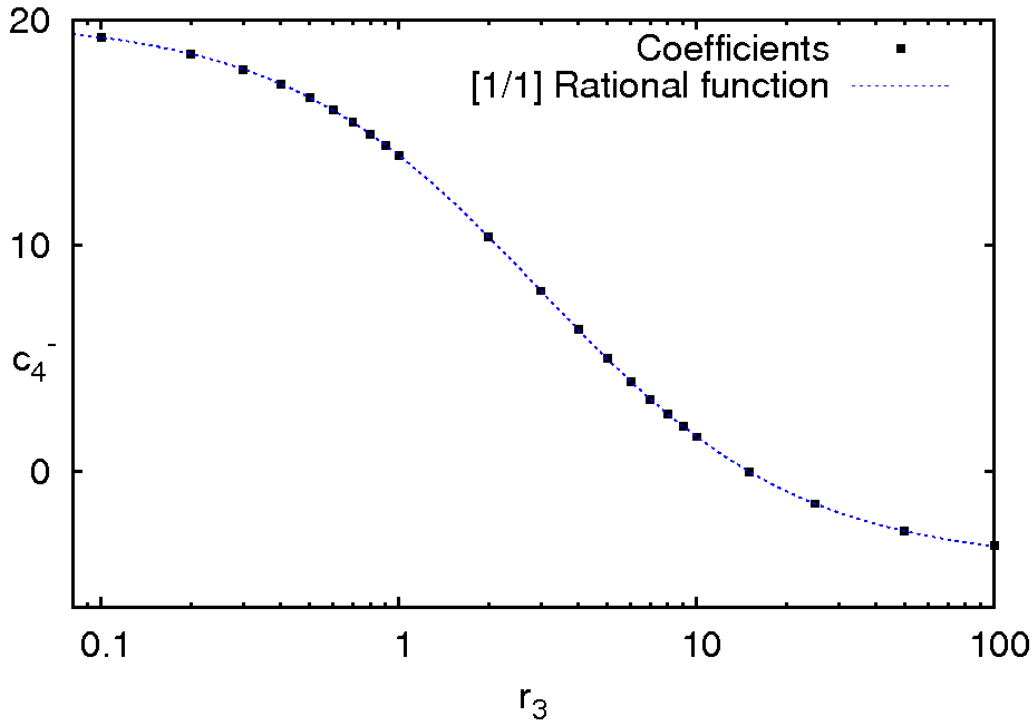
Figure 4.7: Fourth order coefficient for the hole contour in the one dimensional chain as a function of the three-body interacting strength r_3 in a log plot. The coefficient at $r_3 = 0$ passes through the function as well. The [1/1] function for c_4^- is $\dfrac{60 - 4r_3}{3 + r_3}$.

and in third order as

$$|\psi\rangle^{(3)} = -\frac{2\sqrt{2}r_3\lambda^3}{3+r_3}(|021\rangle + |120\rangle) + \frac{3\sqrt{6}\lambda^3}{3+r_3}(|300\rangle + |003\rangle) - 5\sqrt{2}\lambda^3(|201\rangle + |102\rangle), \quad (4.27)$$

where the ket notation $|n_0n_1n_2\rangle$ denotes a state with n_0, n_1, n_2 bosons on the three sites of the cluster.

The wavefunctions for its subgraphs remain unchanged and may be obtained from earlier work [7, 83]. Then using the linked cluster technique for all the graphs [6, 83] up to this order, we obtain the ground state energy per site to be

$$E_0^{1D}/U = -4\lambda^2 + 12\frac{1+r_3}{3+r_3}\lambda^4. \quad (4.28)$$

Instead if we had employed a two-variable perturbation theory, we might have obtained, with U_3 as the second perturbation, the ground state energy to be

$$E_0^{1D} = -4\frac{t^2}{U} + 4\frac{t^4}{U^3} + \frac{8t^4 U_3}{U^4} + \dots \quad (4.29)$$

At first sight, it might seem that any interactions that are diagonalized with the same basis as the two-body interaction could be re-summed into the two-body interactions. For instance, inter-site interaction terms $\sum_{<i,j>} V\hat{n}_i\hat{n}_j$ between nearest neighbours can also be diagonalized by the Fock basis. For which, we may explicitly construct the wavefunctions as in (4.30) and (4.27) to give

$$|\psi\rangle^{(v,2)} = \frac{\sqrt{24}\lambda^2}{3+r_3-v}|030\rangle + 3\sqrt{2}\lambda^2(|210\rangle + |012\rangle), \quad (4.30)$$

and in third order as

$$|\psi\rangle^{(v,3)} = \frac{2\sqrt{2}r_3\lambda^3(4v^2 - 10v - 2r_3v - r_3)}{(3+r_3-v)(1-2v)}(|021\rangle + |120\rangle) + \frac{3\sqrt{6}\lambda^3}{3+r_3-v}(|300\rangle + |003\rangle) - \frac{\sqrt{2}(12v^2 - 4v - 5)\lambda^3}{(1-2v)^3}(|201\rangle + |102\rangle), \quad (4.31)$$

where $v \equiv \frac{V}{U}$. It may be checked that the second order contribution in λ to the ground state energy evaluated from (4.31) does not vanish after subcluster subtraction of the energy of the 2-site cluster with $v \neq 0$. Therefore, being unsure how a linked cluster expansion will proceed with $v \neq 0$, we do not expect such a re-summation scheme as outlined above to hold in the case with *inter-site* interactions.

We see from table 4.3 and (4.28) that for certain values of attractive interactions i.e. $r_3 < 0$ there is a perturbative instability of the $\rho = 1$ Mott phase coming from the divergence of the denominators. This might signal the disappearance of the first lobe altogether or the appearance of a higher-density and energetically more favourable lobe in that region of phase space: quite naturally, for attractive bosons, higher density Mott phases should stabilize the system and one should expand thermodynamic variables perturbatively about this more favourable phase. Similar conclusions were in fact reached by recent MF and quantum Monte Carlo calculations [101]. In the present work, however, the value of the attractive three-body strength that leads to an instability at a given perturbative order can be readily read off from the re-summed coefficients.

4.5 4-body interactions

Using the above procedure for the Hamiltonian with four body interactions i.e. $r_4 \equiv \dfrac{U_4}{U}$, we find that the two-body interactions for the ground state energy densities of the linear chain and the square lattice may also be perturbatively renormalized by the four-body terms using the procedure described. The linked cluster expansion is employed for calculating the ground state energy of the Bose-Hubbard Hamiltonian on the one dimensional chain and the two dimensional square lattice for many different values of the interaction r_4. The rational number coefficients of the expansion in λ are computed and the rational approximation found as in section 2.4.2. We have tabulated in appendix D the 8th and 10th order coefficients for the ground state energy in the one dimensional case; upon application of Thiele's algorithm, it may be seen that the coefficients are exactly expressible as simple rational approximations. As a case in point, the coefficient c_8 is given by

$$c_8 = \frac{4(85x - 7602)}{81(x + 6)}. \tag{4.32}$$

In like manner we continue the procedure for higher order coefficients and for the two dimensional system. Then the energies per site are then be given by the expansions,

$$
\begin{aligned}
E_0^{1D}/U \;=\; & -4\lambda^2 + 4\lambda^4 + \frac{272}{9}\lambda^6 + \frac{4(85r_4 - 7602)}{81(r_4 + 6)}\lambda^8 \\
& - \frac{2(252109r_4^3 + 2870730r_4^2 + 6509628r_4 - 9540936)}{729(r_4 + 6)^3}\lambda^{10} + \dots
\end{aligned} \tag{4.33}
$$

for the one dimensional chain, and

$$
E_0^{2D}/U \;=\; -8\lambda^2 - 24\frac{7r_4 + 27}{r_4 + 3}\lambda^4 - 32\frac{514r_4^4 + 6333r_4^3 + 28167r_4^2 + 53160r_4 + 35217}{(r_4 + 3)^3(2r_4 + 3)}\lambda^6 + \dots \tag{4.34}
$$

for the two dimensional square lattice.

Therefore it seems very likely that two-body terms in the Bose-Hubbard model, irrespective of dimension, may be perturbatively renormalized by *all* higher-body on-site terms for its thermodynamic and excited properties via the described procedure to higher orders. An interesting question is if such re-summability might also exist for dynamical properties and for bosonic models with inter-site interactions; we commented on the prospect for the latter already.

4.6 Conclusions

We have considered critical and thermodynamical properties of lattice bosons described by the Bose-Hubbard Hamiltonian on one and two dimensional lattices. The Mott insulating to superfluid transition was investigated at zero temperature in these systems using a linked cluster expansion technique. With the addition of higher (> 2) body on-site interactions, the Mott lobes were found to increase substantially in the one dimensional case and only marginally in the two dimensional system. The Berezinskii-Kosterlitz-Thouless transition in the one dimensional system was captured accurately by our technique. Additionally, in the two dimensional Bose-Hubbard model, the correlation length critical exponent for the quantum phase transition from the tip of the Mott insulator to the superfluid phase has been found to

correspond to that of the three dimensional *XY* model. This provides evidence for the *XY* universality hypothesis of the system at the multicritical point on the Mott lobe and that the three body terms are irrelevant operators for this transition. It was recently suggested that other transitions [102] in the one dimensional attractive model have universality violated by the introduction of a three body repulsive term.

A procedure for re-summing the effect of a second perturbing variable to infinite order, thereby effectively renormalizing the series coefficients of the single variable expansions, has been presented; in the case of lattice bosons with on-site *n*-body interactions, our systematic procedure was used to find the exactly re-summed coefficients in perturbative expansions of ground and excited state properties for $n = 3, 4$. The procedure is quite general and may be applied to renormalize, exactly or approximately, the second interaction term in the Hamiltonian in the series expansion representation of any thermodynamic quantity to higher orders in a systematic manner. Our results will aid experiments on ultra-cold atoms in optical lattices better understand the physics and Mott lobe stability of lattice bosons with three and four body interactions.

The applicability of the procedure is, of course, not restricted to lattice bosons but can be extended to other systems that are treated using series expansion techniques, ranging from spin models to perturbative quantum chromodynamics where the analytic continuation of strong coupling expansions is still fraught with problems [8].

Acknowlegdgements

Lattice hard-core bosons: spin-wave theory

5.1 Introduction

Bosons on a lattice appear as a natural model for several physical systems. Such a model was used to elucidate the λ-transition in liquid helium II [103] which, at the time, was still lacking a microscopic basis. Furthermore, the authors in Ref. [103] showed that the partition function of a suitably approximated model - which later came to be variously described as the interacting hard-core boson Hubbard model (HCB) - is equal to the partition function of a system of vector spins - the Heisenberg model in a longitudinal magnetic field - as defined on an *infinite* lattice, when a suitable identification of constants and operators between the two models is made.

The authors of Ref. [103] considered the total Hamiltonian of liquid helium on a lattice as

$$\mathcal{H}_L = \frac{\hbar^2}{2md^2} \sum_{<i,j>} (\hat{a}_i^\dagger - \hat{a}_j^\dagger)(\hat{a}_i - \hat{a}_j) - v_o \sum_{<i,j>} \hat{a}_i^\dagger \hat{a}_i \hat{a}_j^\dagger \hat{a}_j, \tag{5.1}$$

where the first term represents the kinetic energy and the second term the potential energy of the system in a lattice of spacing d and nearest neighbour interatomic potential of strength v_o between atoms of mass m. The Bose particles satisfy the commutation relations

$$\left[\hat{a}_i, \hat{a}_j^\dagger\right] = \left[\hat{a}_i, \hat{a}_j\right] = \left[\hat{a}_i^\dagger, \hat{a}_j^\dagger\right] = 0, \qquad (i \neq j), \tag{5.2}$$

and the hard-core condition

$$\hat{a}_i^\dagger \hat{a}_i + \hat{a}_i \hat{a}_i^\dagger = 1,$$
$$\hat{a}_i \hat{a}_i = \hat{a}_i^\dagger \hat{a}_i^\dagger = 0. \tag{5.3}$$

The spinless hard-core bosons were then mapped to an anisotropic Heisenberg spin-1/2 model with the following equivalence relations:

$$\hat{a}_i^\dagger \leftrightarrow S_i^+,$$
$$\hat{a}_i \leftrightarrow S_i^-,$$
$$\hat{a}_i^\dagger \hat{a}_i \leftrightarrow S_i^z + 1/2, \tag{5.4}$$
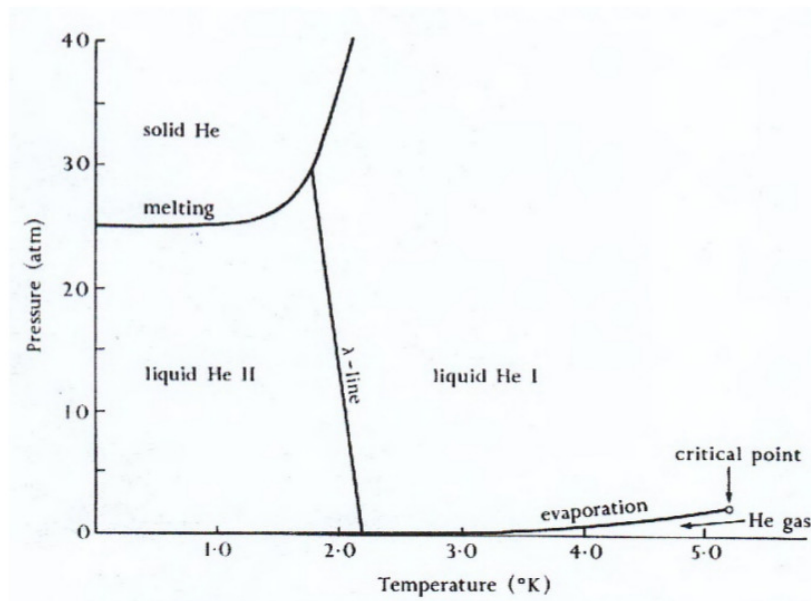
Figure 5.1: Phase diagram of He-4 in pressure and temperature plane showing the 4 different phases. Taken from Ref. [104].
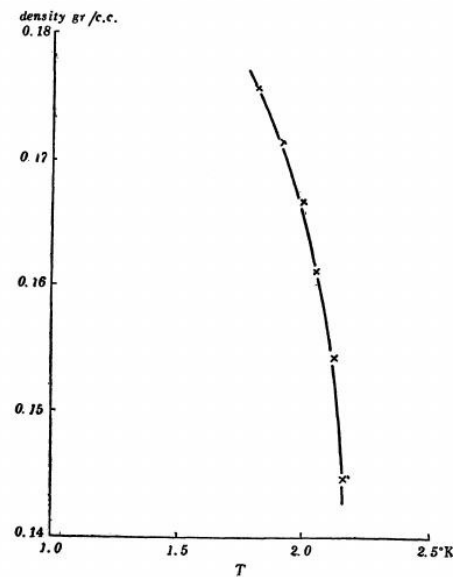
Figure 5.2: The λ-line of liquid helium calculated using a lattice model of hard-core bosons (crosses) compared with experimental measurements of the transition. Taken from Ref. [103].

68

for any lattice site i. With this equivalence, the authors showed that the λ-transition in Helium-4 corresponded to the spin-system, and phonons were proved to correspond to spin-waves in the spin system. The phase diagram of He-4 is shown in Fig. 5.1 including the λ line. Indeed setting the lattice spacing as $d = 3.1$Å and the inter-site potential $v_0 = 0$, the authors [103] were able to obtain remarkable correspondence of (5.1) to the experimental λ line separating the normal fluid and superfluid regions in the helium phase diagram; we show the agreement of the HCB model to experimental measurements in Fig. 5.2.

Within the spin representation, thermodynamical and critical properties of the system could be calculated by an approximation scheme like spin-wave analysis. Employing this approximation, several studies at zero and finite temperatures [105–107] were undertaken. For instance, the question of the existence of supersolid phases in He-4 addressed in these studies on lattice Hamiltonians - although deficient in some aspects with respect to the continuum versions - continue to gather much experimental interest [108]. Differing experimental results and, consequently, opinions regarding the existence of a supersolid phase close to the melting curve, which was the theoretical prediction from spin-wave analysis in Ref. [106], continue to be produced.

5.2 Motivation

With the subsequent development of sophisticated Quantum Monte Carlo (QMC) techniques, spin wave theory (SWT) has been seen to provide a surprisingly adequate description for many physical observables in the HCB model like particle density, ground state energy and suchlike for (a) the non-interacting case [109] and (b) superlattice systems [110]. Indeed, as the authors of Ref. [109, 110] showed, the discrepancies, if any, between the results of the two approaches - QMC and SWT - are extremely small for many thermodynamical properties; recently a system of non-interacting bosons in a transverse field was analysed with a similar semiclassical methodology [111]. This provides further incentive to revisit the corresponding nearest neighbour (NN) interacting problem for a general hypercubic lattice using SWT and QMC. In this chapter, we will focus on calculating thermodynamic quantities using a collinear SWT in the interacting HCB model and compare the results with those of other methods.

Thus motivated by excellent comparisons of SWT with QMC calculations of non-interacting hardcore bosons [109] and superlattices [110], we develop an SWT for interacting hardcore bosons on a d-dimensional (focussing on $d \geq 2$) hypercubic lattice at zero temperature and compare thermodynamical properties with results of Stochastic Series Expansions (SSE): there is good comparison between SWT and SSE results for the square and simple cubic lattice at small repulsive strengths but differences arise between the results of the two approaches for the square lattice at strong repulsions. The boundaries of the three phases - polarized Mott insulating (MI), superfluid (SF) and Néel solid (NS) - can be readily estimated from calculations of particle density, signalling either a first order (SF $\leftrightarrow$ NS) or second order transition (MI $\leftrightarrow$ SF). Comparison is made with results of the Bethe ansatz in one dimension and QMC in two dimensions. Moreover, it was suggested [109] that SWT should be sufficiently accurate even in the interacting case; we find that, starting from a collinear phase, the comparison between SWT and results of SSE is reasonable but not as good as for the non-interacting model on the square lattice with strong repulsions V. For the simple cubic lattice, there is good agreement between the two approaches at a lower V value.

The hard-core boson model with nearest neighbour interactions on a d-dimensional hypercubic lattice is represented by the Hamiltonian

$$\mathcal{H} = -t \sum_{<ij>} (\hat{a}_i^\dagger \hat{a}_j + \text{h.c.}) + V \sum_{<ij>} \hat{n}_i \hat{n}_j - \mu \sum_i \hat{n}_i, \qquad (5.5)$$

where h.c. is the Hermitian conjugate. The $\hat{a}, \hat{a}^\dagger$ annihilation and creation field operators satisfy the bosonic commutation relations for different sites and fermionic anticommutation relations for the same site, thereby preventing double occupancy, as described in (5.2) and (5.3); $\hat{n} = \hat{a}^\dagger \hat{a}$ is the boson number operator. The interaction V and hopping t are between NN sites, and the chemical potential μ controls the particle density.

5.3 Spin wave analysis

Although we present a self-contained description of our work, more applications and details may be found in the standard treatment of mean field and spin wave theory in Refs. [112, 113]. In the subsequent formulation, we closely follow the notation of Ref. [109].
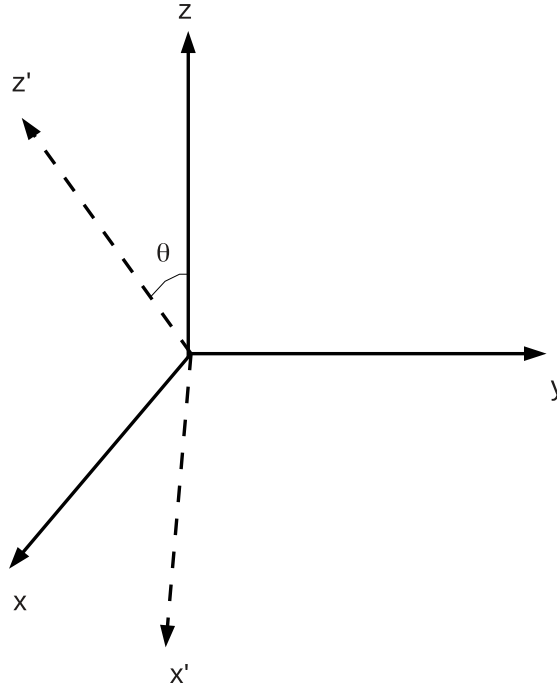
Figure 5.3: Spin wave corrections to the mean field solution (5.7) are introduced by rotation of the coordinate axes.

Upon changing to the spin representation using (5.4), the Hamiltonian in (5.5) becomes

$$\mathcal{H} = -t \sum_{<ij>} (\hat{S}_i^+ \hat{S}_j^- + \text{h.c.}) + V \sum_{<ij>} \hat{S}_i^z \hat{S}_j^z - \left(\mu - \frac{zV}{2}\right) \sum_i \hat{S}_i^z - \frac{1}{2}\left(\mu - zV/4\right) N, \qquad (5.6)$$

where z is the number of nearest neighbours and N the number of lattice points. For hypercubic lattices in d-dimensions, $z = 2d$.

Consider the mean-field (MF) ground state $|\psi\rangle = \prod_{i=1}^{N}(\sin(\theta/2) + \cos(\theta/2)\hat{a}_i^\dagger)|0\rangle$, where θ is the angle

made by the (pseudo)spins with respect to the z-axis. We choose, without loss of generality, an ordering such that the xz plane contains all the spins. Minimizing the grand canonical potential per site $\Omega = \langle \psi | \mathcal{H} | \psi \rangle$ with respect to the angle θ, we obtain, for the mean field values,

$$\Omega_{MF} = \rho_{MF} \left(\frac{z}{2} V \rho_{MF} - \mu + zt\rho_{MF} - zt \right), \tag{5.7}$$

where the mean field particle density

$$\rho_{MF} \equiv \cos^2 (\theta/2) = \frac{\mu + zt}{z(2t + V)}. \tag{5.8}$$

The energy density is given by $E_{MF} = \Omega_{MF} + \mu \rho_{MF}$.

Spin wave corrections can be included by twisting the z-axis to align with the direction of MF magnetization as shown in Fig. 5.3:

$$\begin{aligned}
\hat{S}_i^x &= \tilde{S}_i^x \cos (\theta) + \tilde{S}_i^z \sin (\theta) \\
\hat{S}_i^y &= \tilde{S}_i^y \\
\hat{S}_i^z &= -\tilde{S}_i^x \sin (\theta) + \tilde{S}_i^z \cos (\theta).
\end{aligned}$$

$$\tag{5.9}$$

In this rotated frame, the excitations are bosonic in nature because the spin-flips change the $\tilde{S}^z$ projected spin values by ± 1. This requires a bosonic representation using the Holstein-Primakoff transformations for hard-core bosons

$$\begin{aligned}
\tilde{S}_i^x &= \frac{1}{2} \left(b_i^\dagger + b_i \right) \\
\tilde{S}_i^y &= \frac{1}{2i} \left(b_i^\dagger - b_i \right) \\
\tilde{S}_i^z &= \frac{1}{2} - b_i^\dagger b_i,
\end{aligned}$$

$$\tag{5.10}$$

where the $b, b^\dagger$ describe the usual lattice bosons (4.2) without a hard-core constraint.

Then the Hamiltonian with spin-wave (SW) corrections is given by

$$\begin{aligned}
\mathcal{H}_{\text{SW}} &= \sum_{<i,j>} [\tilde{S}_i^x \tilde{S}_j^x \left(V \sin^2 (\theta) - 2t \cos^2 (\theta) \right) + \tilde{S}_i^z \tilde{S}_j^z \left(V \cos^2 (\theta) - 2t \sin^2 (\theta) \right) - 2t \tilde{S}_i^y \tilde{S}_j^y - \\
&\quad 2\tilde{S}_i^x \tilde{S}_j^z (2t + V)] - \left(\mu - \frac{zV}{2} \right) \sum_i \left(-\tilde{S}^x \sin (\theta) + -\tilde{S}^z \cos (\theta) \right) + \frac{N}{2} \left(\frac{zV}{4} - \mu \right).
\end{aligned} \tag{5.11}$$

The individual terms in (5.11) when transformed according to (5.10), discarding cubic terms and beyond, are given by

$$\begin{aligned}
\sum_{<i,j>} \tilde{S}_i^x \tilde{S}_j^x &\rightarrow \frac{1}{4} \sum_{<i,j>} \left(b_i^\dagger b_j^\dagger + b_i^\dagger b_j + b_i b_j^\dagger + b_i b_j \right), \\
\sum_{<i,j>} \tilde{S}_i^y \tilde{S}_j^y &\rightarrow \frac{1}{4} \sum_{<i,j>} \left(-b_i^\dagger b_j^\dagger + b_i^\dagger b_j + b_i b_j^\dagger - b_i b_j \right),
\end{aligned} \tag{5.12}$$

for the transformed terms not invariant under the group $U(1)$, and

$$2 \sum_{<i,j>} \tilde{S}_i^x \tilde{S}_j^z \quad \rightarrow \quad \frac{z}{4} \sum_{<i,j>} (b_i^\dagger + b_i) + \dots,$$

$$\sum_{<i,j>} \tilde{S}_i^z \tilde{S}_j^z \quad \rightarrow \quad \sum_i \frac{z}{4} - \frac{z}{2} \sum_i b_i^\dagger b_i + \dots,$$

$$\sum_i \tilde{S}_i^x \quad \rightarrow \quad \frac{1}{2} \sum_i (b_i^\dagger + b_i),$$

$$\sum_i \tilde{S}_i^z \quad \rightarrow \quad \sum_i \left(\frac{1}{2} - b_i^\dagger b_i \right). \tag{5.13}$$

for the rest. Substituting (5.12), (5.13) in (5.11), we get the following bosonic representation of the spin wave Hamiltonian up to quadratic order:

$$\begin{aligned}
\mathcal{H}_{SW} \quad = \quad & \sum_{<ij>} \left\{ (b_i^\dagger b_j^\dagger + b_i b_i) \left(\frac{t}{2} + \frac{V}{4} \right) \sin^2(\theta) + (b_i^\dagger b_j + b_i b_j^\dagger)(-\frac{t}{2}(1 + \cos^2(\theta)) + \frac{V}{4} \sin^2(\theta)) \right\} + \\
& \sum_i b_i^\dagger b_i \left[zt \sin^2(\theta) - \frac{zV}{2} \cos^2(\theta) + \left(\mu - \frac{zV}{2} \right) \cos(\theta) \right] + \\
& N \left[\left(\frac{zV}{4} - \frac{\mu}{2} \right) \cos(\theta) + \frac{z}{4} \left(\frac{V}{2} \cos^2(\theta) - t \sin^2(\theta) \right) + \frac{zV/4 - \mu}{2} \right] + \\
& \sum_i \left[\frac{\mu - zV/2}{2} \sin(\theta) - \frac{z}{4}(2t + V) \cos(\theta) \sin(\theta) \right] (b_i^\dagger + b_i). \tag{5.14}
\end{aligned}$$

So that the particle number is conserved in the new bosonic system, we require that each of the last summands in the last line of (5.14) disappear. This gives the spin-wave condition for θ to be

$$\cos(\theta) = \frac{2\mu - zV}{z(2t + V)}. \tag{5.15}$$

This was also the same condition previously obtained without the spin waves corrections in (5.8), noted as well in the non-interacting case [109]. We mention that we can, from the above, obtain a *d*-dimensional analogue of the Pokrovsky-Talapov line [114] separating the massless and the ferromagnetic phases in the one-dimensional anisotropic Heisenberg model in a longitudinal field by equating $\cos(\theta) = 1$. This gives the second order phase separating line between the polarized MI and SF phases to be

$$(\mu)_c^{PT} = z(t + V). \tag{5.16}$$

In order to diagonalize (5.14), we first take the Fourier transform of the field operators to momentum $\vec{\mathbf{k}}$-space

$$b_i^\dagger = \frac{1}{\sqrt{N}} \sum_{\vec{\mathbf{k}}} e^{-i\vec{\mathbf{k}}.\vec{\mathbf{r}}_i} b_{\vec{\mathbf{k}}}^\dagger,$$

$$b_i = \frac{1}{\sqrt{N}} \sum_{\vec{\mathbf{k}}} e^{-i\vec{\mathbf{k}}.\vec{\mathbf{r}}_i} b_{\vec{\mathbf{k}}}. \tag{5.17}$$

Using (5.17), the individual terms in (5.14) are transformed as

$$
\begin{aligned}
\sum_{<i,j>} b_i^\dagger b_j^\dagger &\rightarrow \frac{1}{N} \sum_{\vec{\mathbf{k}}} \gamma_{\vec{\mathbf{k}}} b_{\vec{\mathbf{k}}}^\dagger b_{-\vec{\mathbf{k}}}^\dagger, \\
\sum_{<i,j>} b_i b_j &\rightarrow \frac{1}{N} \sum_{\vec{\mathbf{k}}} \gamma_{\vec{\mathbf{k}}} b_{\vec{\mathbf{k}}} b_{-\vec{\mathbf{k}}}, \\
\sum_{<i,j>} b_i^\dagger b_j &\rightarrow \frac{1}{N} \sum_{\vec{\mathbf{k}}} \gamma_{\vec{\mathbf{k}}} b_{\vec{\mathbf{k}}}^\dagger b_{\vec{\mathbf{k}}}, \\
\sum_{<i,j>} b_i b_j^\dagger &\rightarrow \frac{1}{N} \sum_{\vec{\mathbf{k}}} \gamma_{\vec{\mathbf{k}}} b_{-\vec{\mathbf{k}}} b_{-\vec{\mathbf{k}}}^\dagger, \\
\sum_{i} b_i^\dagger b_i &\rightarrow \frac{1}{2} \sum_{k} \left(b_{\vec{\mathbf{k}}}^\dagger b_{\vec{\mathbf{k}}} + b_{-\vec{\mathbf{k}}}^\dagger b_{-\vec{\mathbf{k}}} \right),
\end{aligned}
\tag{5.18}
$$

where the scaled dispersion $\gamma_{\vec{\mathbf{k}}}$ is given by

$$
\gamma_{\vec{\mathbf{k}}} = \sum_{i=1}^{\frac{z}{2}} \cos\left(k_i\right).
\tag{5.19}
$$

Substituting (5.18) in (5.14), we get the Hamiltonian in Fourier space as

$$
\mathcal{H}_{\mathrm{SW}} = \mathcal{H}_{\mathrm{MF}} + \sum_{\vec{\mathbf{k}}} A_{\vec{\mathbf{k}}} \left(b_{\vec{\mathbf{k}}}^\dagger b_{\vec{\mathbf{k}}} + b_{-\vec{\mathbf{k}}}^\dagger b_{-\vec{\mathbf{k}}} \right) + \sum_{\vec{\mathbf{k}}} B_{\vec{\mathbf{k}}} \left(b_{\vec{\mathbf{k}}}^\dagger b_{-\vec{\mathbf{k}}}^\dagger + b_{\vec{\mathbf{k}}} b_{-\vec{\mathbf{k}}} \right).
\tag{5.20}
$$

The sum over $\vec{\mathbf{k}}$ is over the first Brillouin zone and the mean field Hamiltonian $\mathcal{H}_{\mathrm{MF}}$ corresponds to the mean field grand canonical potential Ω_{MF} in (5.7). The variables $A_{\vec{\mathbf{k}}}, B_{\vec{\mathbf{k}}}$ are here given by

$$
A_{\vec{\mathbf{k}}} = \frac{zt}{2} + \frac{\gamma_{\vec{\mathbf{k}}}}{4} \left[(V - 2t) - \frac{(2\mu - zV)^2}{z^2(2t + V)} \right],
\tag{5.21}
$$

$$
B_{\vec{\mathbf{k}}} = \frac{\gamma_{\vec{\mathbf{k}}}}{z^2(2t + V)} \left[tz^2(t + V) + \mu(zV - \mu) \right],
\tag{5.22}
$$

$$
\gamma_{\vec{\mathbf{k}}} = \sum_{i=1}^{\frac{z}{2}} \cos\left(k_i\right).
\tag{5.23}
$$

The spin wave Hamiltonian in (5.20) retains the same form as in Ref. [109] except for the coefficients of the operators. In order to diagonalize (5.20), we employ the Bogoliubov transformation

$$
\begin{aligned}
b_{\vec{\mathbf{k}}} &= u_{\vec{\mathbf{k}}} \alpha_{\vec{\mathbf{k}}} - v_{\vec{\mathbf{k}}} \alpha_{-\vec{\mathbf{k}}}^\dagger \\
b_{\vec{\mathbf{k}}}^\dagger &= u_{\vec{\mathbf{k}}} \alpha_{\vec{\mathbf{k}}}^\dagger - v_{\vec{\mathbf{k}}} \alpha_{-\vec{\mathbf{k}}},
\end{aligned}
\tag{5.24}
$$

to separate the MF ground state and the excited states above it, represented by the $\alpha, \alpha^\dagger$ bosons. The overall scheme is depicted in Fig. 5.4. In order to satisfy bosonic commutation relations for the $\alpha, \alpha^\dagger$ operators, the relation

$$
\left[\alpha_{\vec{\mathbf{k}}}, \alpha_{\vec{\mathbf{k}}'}^\dagger \right] = \delta_{\vec{\mathbf{k}}, \vec{\mathbf{k}}'}
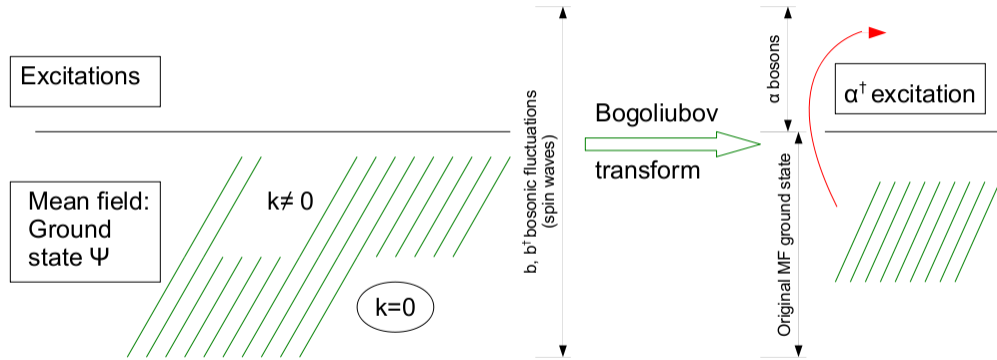\tag{5.25}
$$

Figure 5.4: Mean field and spin wave fluctuations of a Hamiltonian. Bogoliubov transformation (5.24) separates the bosonic excitations from the ground state.

must be enforced, where δ is the Kronecker delta function. This immediately leads to the condition

$$u_{\vec{k}}^2 - v_{\vec{k}}^2 = 1. \tag{5.26}$$

From (5.26), we may choose the parametrization $u_{\vec{k}} = \sinh(\phi_{\vec{k}})$ and $v_{\vec{k}} = \cosh(\phi_{\vec{k}})$. Assuming that $u_{\vec{k}} = u_{-\vec{k}}$ and $v_{\vec{k}} = v_{-\vec{k}}$, and using (5.24) in (5.20), we get the spin wave Hamiltonian to be

$$\mathcal{H}_{\text{SW}} = \mathcal{H}_{\text{MF}} + \sum_{\vec{k}} \left[A_{\vec{k}} \left(u_{\vec{k}}^2 + v_{\vec{k}}^2 \right) - 2u_{\vec{k}}v_{\vec{k}}B_{\vec{k}} \right] \left(\alpha_{\vec{k}}^\dagger \alpha_{\vec{k}} + \alpha_{-\vec{k}}^\dagger \alpha_{-\vec{k}} \right) + \sum_{\vec{k}} \left(2v_{\vec{k}}^2 A_{\vec{k}} - 2u_{\vec{k}}v_{\vec{k}}B_{\vec{k}} \right) +$$

$$\sum_{\vec{k}} \left[B_{\vec{k}} \left(u_{\vec{k}}^2 + v_{\vec{k}}^2 \right) - 2u_{\vec{k}}v_{\vec{k}}A_{\vec{k}} \right] \left(\alpha_{\vec{k}} \alpha_{-\vec{k}} + \alpha_{\vec{k}}^\dagger \alpha_{-\vec{k}}^\dagger \right). \tag{5.27}$$

The coefficients in the last line are set to zero to preserve gauge invariance in the $\alpha, \alpha^\dagger$ operators (bosonic excitations) i.e.

$$2u_{\vec{k}}v_{\vec{k}} = \frac{B_{\vec{k}}}{A_{\vec{k}}} \left(u_{\vec{k}}^2 + v_{\vec{k}}^2 \right). \tag{5.28}$$

The parameters $u_{\vec{k}}$ and $v_{\vec{k}}$ may be evaluated from (5.28) by defining $r \equiv u_{\vec{k}}/v_{\vec{k}}$ and solving a simple quadratic equation to give

$$u_{\vec{k}}^2(v_{\vec{k}}^2) = \frac{1}{2} \left(\frac{A_{\vec{k}}}{\sqrt{A_{\vec{k}}^2 - B_{\vec{k}}^2}} \pm 1 \right). \tag{5.29}$$

With this, the diagonalized spin-wave Hamiltonian in terms of the Bogoliubov operators is given by

$$\mathcal{H}_{SW} = \mathcal{H}_{MF} + \sum_{\vec{k}} \left(\sqrt{A_{\vec{k}}^2 - B_{\vec{k}}^2} - A_{\vec{k}} \right)$$

$$+ \sum_{\vec{k}} \sqrt{A_{\vec{k}}^2 - B_{\vec{k}}^2} \left(\alpha_{\vec{k}}^\dagger \alpha_{\vec{k}} + \alpha_{-\vec{k}}^\dagger \alpha_{-\vec{k}} \right). \tag{5.30}$$

5.4 Thermodynamic quantities

Using the above results, we can generalize the results in Ref. [109] to a hypercubic lattice in arbitrary dimensions. The average particle density, including the spin waves within the MF state, is given by

$$\rho_{SW} = -\frac{\partial \Omega_{SW}}{\partial \mu} = \rho_{MF} + \mu \frac{2\mu - zV}{z^2 N(2t + V)} \sum_{\vec{k}} \gamma_{\vec{k}} \left(\frac{A_{\vec{k}} - B_{\vec{k}}}{\sqrt{A_{\vec{k}}^2 - B_{\vec{k}}^2}} - 1 \right), \tag{5.31}$$

where Ω_{SW} is given by the expectation value of the first line of (5.30), whereas the coefficient $\sqrt{A_{\vec{k}}^2 - B_{\vec{k}}^2}$ in the second line represents the dispersion of the excitations. In Fig. 5.5a we compare the boson density calculated using SWT, with results of QMC simulations (SSE implemented using the ALPS library [115]) and MF analysis on the square lattice for $V/t = 10$. In the SSE simulation we used inverse temperature $\beta \equiv 1/T = 40$ on an $L \times L = 25 \times 25$ system with half a million sweeps and a thermalization of ten thousand; the error bars are not shown (because they are only as large as the symbol size) and simulations were done for various system sizes ($L = 25, 12, 6, 4$), sweeps, thermalization and inverse temperatures ($\beta = 40, 20, 10$) to check for convergence. As can be seen SWT is an improvement over the MF results but compares only approximately with SSE, with the differences increasing towards the phase boundary of the checkerboard solid; the comparison is not as good as with the non-interacting system in Ref. [109], which we have verified as shown in the inset of Fig. 5.5b. On the square lattice at $V/t = 1$, where no checkerboard solid is nearby in phase space, SWT is much more accurate as seen from the inset of Fig. 5.5a. For one dimension higher, i.e. simple cubic lattice, and again at $V/t = 1$, spin wave analysis compares extremely well with an SSE simulation with the aforementioned thermalization, sweeps, and temperature values on a system of size 5x5x5.

The energy density in the SW approximation is obtained as before within mean field i.e. $E_{SW} = \Omega_{SW} + \mu \rho_{SW}$. Finally, the functional expressions for the expectation value of the condensate fraction ρ_0 - particle density in the zero momentum sector - within MF and SW remain the same as in the absence of NN interactions of Ref. [109]:

$$\rho_{0,MF} = \rho_{MF}(1 - \rho_{MF}),$$
$$\rho_{0,SW} = \rho(1 - \rho) - \frac{1}{N} \sum_{\vec{k} \neq \vec{0}} v_{\vec{k}}^2. \tag{5.32}$$

The energy density in the simple cubic lattice for 2 different interaction strengths V are computed as functions of the SW particle density by Legendre transforming from the μ variable and shown in Fig. 5.5b. The condition $E(\rho) = E(1 - \rho)$ is not satisfied at a finite V because it is clear that larger particle densities contribute more to the inter-site repulsive energy. From the figure, the usual expectations are borne out: higher inter-site repulsion adds more SW contributions to the MF value. That is, lower the interaction, better is the MF description. This may be seen by the distance between the location of the arrows (MF values) and the corresponding SW values for two different interaction strengths at density $\rho = 1$. It is worth noting from (5.32) that the MF condensate fraction depends only on the particle density and not on the interaction strength; whereas the larger the V value, the more will Bose-Einstein condensation be suppressed within SWT. We point out that this need not have any direct bearing on the superfluid fraction in the system because Bose-Einstein condensation and superfluidity are distinct phenomena, although incorrectly interchangeably used oftentimes; see Appendix A for a clarification of the conceptual differences between the two.
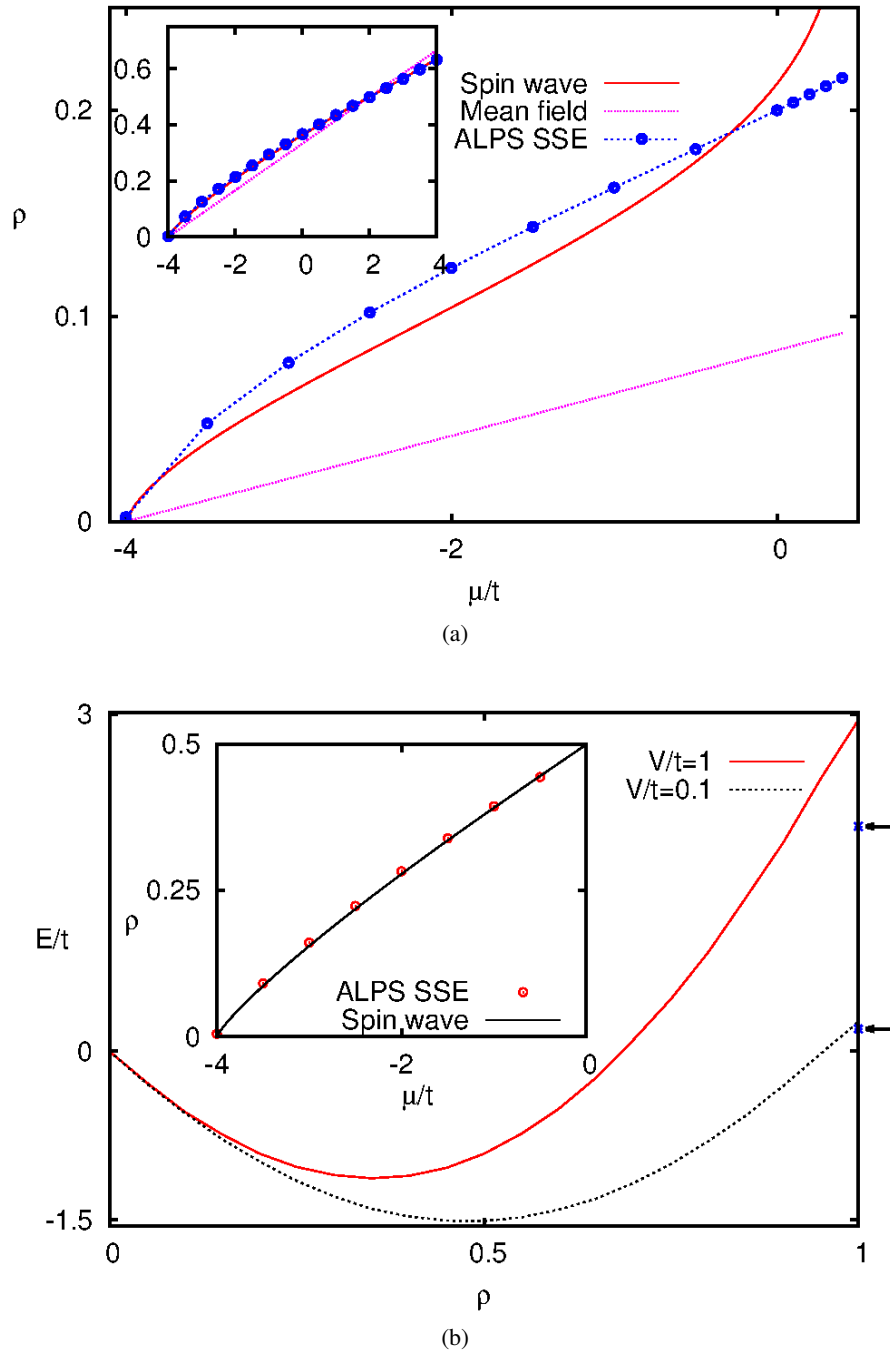
(a)

(b)

Figure 5.5: (a) Mean field particle density on the square lattice compared with spin-wave results and implementation of Stochastic Series Expansion (SSE) using the ALPS library [115] at $V/t = 10$ and $V/t = 1$ (inset). At strong coupling and close to the first-order transition to the checkerboard solid, spin wave theory does not converge. (b) Energy density for the simple cubic lattice in the full boson density range, with arrows indicating MF values at $\rho = 1$. Inset shows the boson density computed using spin-wave and ALPS's SSE [115] on the square lattice at $V = 0$, verifying the result of Ref. [109].

5.5 Excitations

As seen in the previous section, the excitation spectrum of the α bosons is given by $\omega(\vec{\mathbf{k}}) = \sqrt{A_{\vec{\mathbf{k}}}^2 - B_{\vec{\mathbf{k}}}^2}$. The quantities $A_{\vec{\mathbf{k}}}$, $B_{\vec{\mathbf{k}}}$ still depend on μ, V but the dependence is notationally suppressed. The dispersion is calculated along the line $k_x = k_y = k_z$ for a simple cubic lattice and plotted in Fig. 5.6a for two different interaction strengths. Far away from the expected checkerboard solid phase, antiferromagnetic ordering is not expected for any particle density. This is indeed true and checked for $V/t = 1$ for all range of densities between the empty and full phases. That is, the dispersion in this case is always gapped at $\vec{\mathbf{k}} = (\pi, \pi, \pi)$. The dispersion at the boundaries of these two ferromagnetic phases - $\mu/V = -6, 12$ - show $\lim_{|\vec{\mathbf{k}}| \to 0} \omega(\vec{\mathbf{k}}) \propto |\vec{\mathbf{k}}|^2$ (upper panel of Fig. 5.6a) as expected for such ordering. The gap to magnon excitations in the polarized MI phase is given by $\Delta = \left(\mu - (\mu)_c^{PT}\right)/2$.

In the strong coupling limit - $V/t = 10$ - antiferromagnetic ordering sets in as the checkerboard solid is approached. This is seen in the lower panel of Fig. 5.6a, where for $\mu/V = 0.6$,

$$
\omega(\vec{\mathbf{k}}) \propto \begin{cases} |\vec{\mathbf{k}}|, & |\vec{\mathbf{k}}| \approx 0 \\ |\vec{\mathbf{k}} - (\pi, \pi, \pi)|, & |\vec{\mathbf{k}}| \approx (\pi, \pi, \pi). \end{cases} \tag{5.33}
$$

Finally, although the SWT ground state phase diagram has already been fleshed out in detail [117, 118], our purpose here is merely to compare it with other known results. The SWT construction proceeds in the usual way: for every interaction strength, the particle density is calculated for all chemical potentials. The density ρ (5.31) will have a discontinuity at two values of μ corresponding to the first order phase transition between the solid and superfluid. These will define the boundaries of the expected checkerboard solid lobe with density $\rho = 1/2$. Moreover, it must be recalled that within our SWT, only collinear phases are describable because we chose $\theta_i = \theta$. Therefore, we do not expect convergence in the solid phase anyway. With these assumptions, the SWT phase diagram is constructed for the HCB model on a d-dimensional hypercubic lattice; the separation between the massless and the ferromagnetic phase was already given by (5.16).

This is compared to QMC calculations in two dimensions [116] and the Bethe ansatz solution in one dimension. The latter was solved for the anisotropic Heisenberg model on a chain [98]; the critical line $\left(\dfrac{\mu}{V}\right)_c$ separating the massless and antiferromagnetic phase is given by

$$
\frac{V}{2t}\left[\left(\frac{\mu}{V}\right)_c - 1\right] = \sinh(\lambda) \sum_{n=-\infty}^{\infty} (-1)^n \cosh^{-1}(n\lambda), \tag{5.34}
$$

where $\lambda = \cosh^{-1}\left(\dfrac{V}{2t}\right)$. The Pokrovsky-Talapov line remains the same. The comparisons between Bethe ansatz in one dimension, QMC in two dimensions, and MF and SWT in d dimensions is shown in Fig. 5.6b. Note that as pointed out in Ref. [117], the spin wave fluctuations retain the stability of the checkerboard solid phase obtained via a mean field treatment although particle fluctuations within the phase will be induced by the spin waves. The upper mean field contour of the solid phase is given by [117]

$$
\frac{\mu}{dV} = 1 + \sqrt{1 - 4\frac{t^2}{V^2}}, \tag{5.35}
$$

which agrees well with the spin wave solution as shown in Fig. 5.6b.
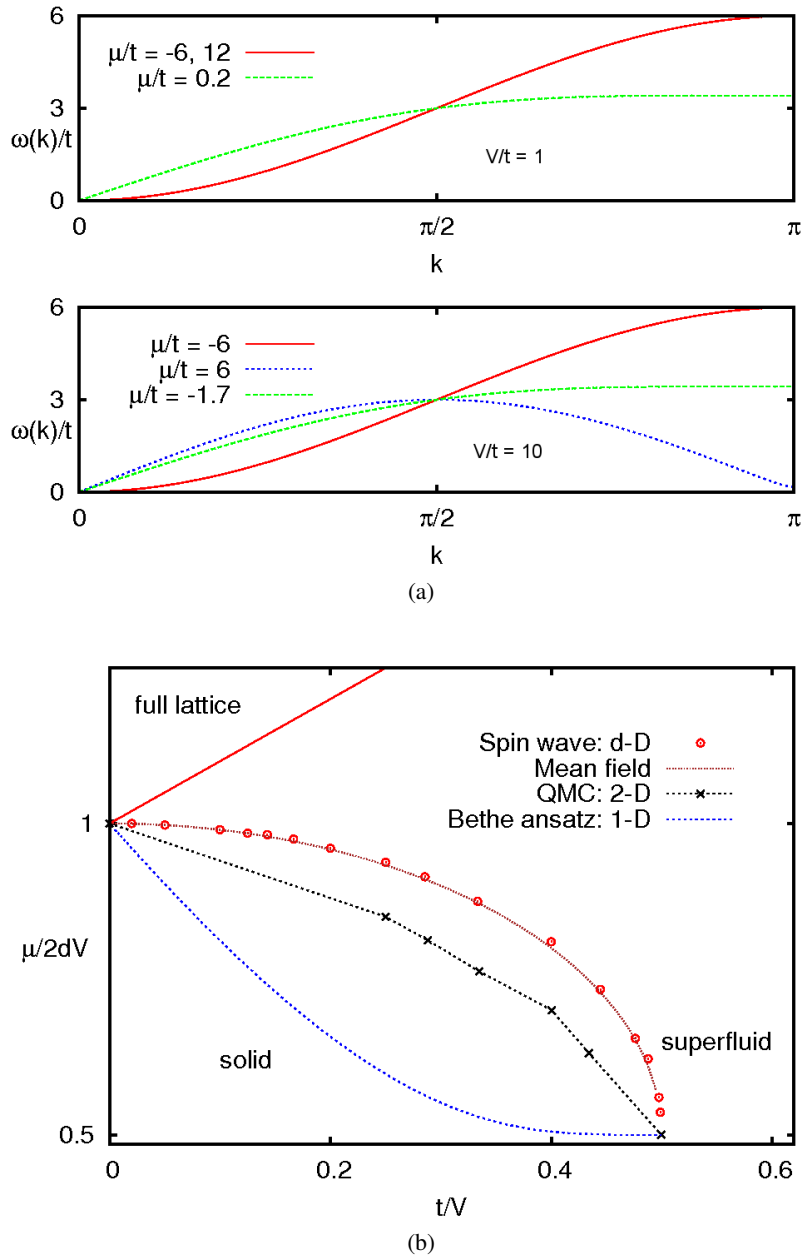
Figure 5.6: (a) Quasiparticle - α bosons - dispersion for 2 interaction strengths along $k_x = k_y = k_z$ in the simple cubic lattice. As explained in the text, ferromagnetic and antiferromagnetic ordering is readily seen from behaviour near the zone edge or centre. (b) Mean field or spin wave phase diagram compared with other known results like QMC [116] on a square lattice and Bethe ansatz on a linear chain. The role of quantum fluctuations on decreasing dimensionality may be appreciated from this diagram.

5.6 Conclusions

We have presented a generalized spin wave theory for hypercubic lattices in arbitrary dimensions for a hard-core boson model with nearest neighbour interaction. Based on earlier work [109, 110], where in Ref. [109] it was suggested that such a spin-wave theory should give reasonable results for the

interacting system as well, we find that the comparison with Stochastic Series Expansion (quantum Monte Carlo) for the square lattice with strongly repelling ($V/t = 10$) nearest neighbour bosons is not as good as it is with the non-interacting case. The agreement is considerably improved at lower V/t values.

Although we did not start with a bond-ordered phase, as suggested in Ref. [109], we can compute observables like particle density and internal energy as long as the system is not within or close to the checkerboard solid phase: the collinear mean field states should, in principle, describe the superfluid and polarized Mott insulating phases. These quantities are evaluated for the square and simple cubic lattices, and compared with the mean field values. At $V/t = 1$ away from the strongly-repulsive regime i.e. away from any neighbouring checkerboard phase, we find good comparison for the particle density between results of spin-wave theory and stochastic series expansions for both the square and simple cubic lattices.

Our comparison of the ground-state phase diagrams - showing the checkerboard solid, superfluid and polarised Mott phases - using Bethe ansatz in one dimension, quantum Monte Carlo in two dimensions, and spin-wave theory in $d \geq 2$ dimensions provides a good gauge on the effect of dimensionality on quantum fluctuations in the system.

Acknowledgements

Lattice hard-core bosons: series expansions

6.1 Motivation

As outlined in the previous chapter, bosonic systems are naturally modelled by the hard-core boson Hamiltonian (5.5). Whereas there we concentrated on bipartite and hypercubic lattices, in this chapter we will focus our studies on the kagome lattice (Fig. 3.2a). The geometry of the lattice that the particles (whether spins or fermions or bosons) occupy determines their motion and possible arrangements, much as a bumpy or pockmarked road constrains vehicular motion. In the latter, one major energy scale of concern is the friction between the surface and the body. In materials however, moderate temperature changes can often contribute enough energy to the system to compete with other effects like quantum mechanical ones; these two effects induce thermal and quantum fluctuations of particle configurations in the system. Therefore, in order to study the material with solely its quantum mechanical effects, the energy scale of the temperature needs to be substantially reduced compared with all the inherent quantum mechanical energy scales. Indeed in recent times, there has been much work devoted in this direction to identify possible new phases of matter as dictated by the lattice geometry and the quantum effects of the particles involved. An illustrative case in point is that of the kagome lattice of Fig. 3.2a where spin and boson systems have been extensively investigated [119–123]. We briefly review the interest in the field thereby motivating work of this chapter.

In Ref. [120], the authors considered the spin dynamics of the material $ZnCl_3(OD)_6Cl_2$ (herbertsmith-ite) which has two dimensional planes of copper ions arranged in a kagome lattice pattern; the Cu^{2+} ions interact via Heisenberg spin-1/2 interactions with a coupling of $J \approx 200K$ (17 meV). The material is shown in Fig. 6.1a. The authors reduced the temperature to about 50 mK, many orders of magnitude below the exchange coupling strength, but found no evidence for ordering of the spins, as might be expected in usual materials when the constituent particles "freeze" out; such appearance of long range order occurs for the corresponding square lattice model. For the kagome lattice model, further evidence [123] using inelastic neutron scattering strongly suggested the presence of an unconventional phase, a spin liquid; the continuum in the excitation spectrum for a range of exchange energies, as shown in Fig. 6.1b across symmetry cuts in the Brillouin zone, was argued to be indicative of fractionalized excitations harboured by the ground state spin liquid.

We had already indicated in (5.4) the equivalence between hard-core bosons and spin-1/2 systems. Therefore it is not unreasonable to expect a hard-core boson model to support an exotic ground state like a spin liquid under appropriate conditions. Indeed a non-trivial spin liquid was demonstrated to

exist for hard-core bosons on the kagome lattice modelled by a Hamiltonian much like (5.5) except that the interactions between bosons involved all sites along hexagons on the lattice [121]. The same authors later identified a novel quantum phase transition in the same system driven by fractionalized excitations [122] and suggested, due to the topological nature of the transition, that such systems might prove useful for quantum computing purposes in the future.
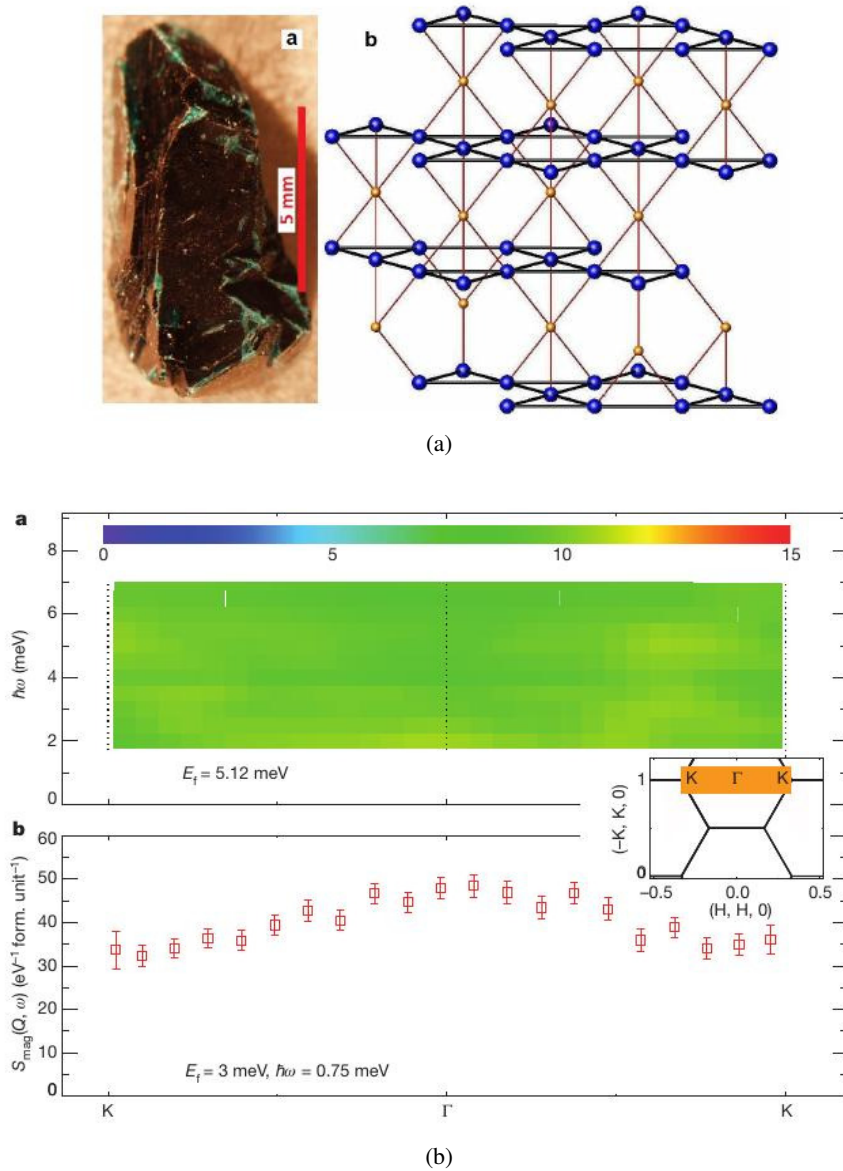

(a)

(b)

Figure 6.1: (a) Mineral $ZnCl_3(OD)_6Cl_2$ (herbertsmithite). On the right the kagome planes with Cu^{2+} ions (large blue circles) are clearly visible. The Zn^{2+} ions (small brown circles) and copper ions do not couple strongly. (b) Dynamic structure factor, in barn per steradian per electron Volt per formula unit, measured by inelastic neutron scattering for a range of energy transfers ($\hbar\omega$) along the indicated direction in the Brillouin zone (inset). The data show a broad continuum, taken to be a signature of fractionalized spin excitations in the compound. Both figures are taken from Ref. [123].

The upshot of all this is that the kagome lattice has been shown, both theoretically and experimentally

over the years, to support exotic phases and new physics for spin and boson models. The exploration of their possible phases and properties is an active area of research. A hotly pursued technique for the quantum simulation of lattice models is through ultra-cold atoms in optical lattices. Indeed there has been much progress in the manipulation of interactions and modelling of physical systems using ultra-cold gases. A wide range of condensed matter systems like Ising spin systems [124], Bose-Hubbard models [77], Fermi gases [125], to name a few, have been simulated using ultra-cold gases; an equally wide range of condensed matter phases continue to be uncovered in these ultra-cold systems. The hard-core boson model (in the absence of nearest neighbour interactions V) has indeed been realized in an optical lattice with ^{87}Rb atoms [126]. Moreover, an optical kagome lattice has been realized recently by the overlay of two commensurate triangular optical lattices [127]. Our work in this chapter, where we primarily investigate thermodynamical and critical properties of interacting hard-core bosons on the kagome lattice, will therefore be relevant for experimental realizations of interacting hard-core bosons on such optical kagome lattices. We make some comparisons of the kagome model with the properties of the simpler one dimensional lattice. Our computations will employ the thermodynamic Bethe ansatz, statistics of the 8-vertex model, transfer matrix methods, and numerical linked cluster expansions.

6.2 Numerical linked cluster expansion

As explained in chapter 2 and Ref. [9], the series expansion can be done via bond, site or cell based expansions. In the present work, we work mainly with site and cell expansions; for the kagome lattice, a cell is a simple triangular graph. In our notation, an n-site/cell numerical linked cluster expansion (NLCE) refers to n being the maximum number of sites/triangles in the list of finite clusters. And unless otherwise specified, angular averages are taken in the grand canonical ensemble.

Additionally, as explained in the aforementioned chapter and reference, we need to extrapolate the series of results for finite clusters to the result for an infinitely large cluster: this essentially increases the temperature range of convergence. Here we use Wynn's epsilon algorithm [26] and a numerically more stable version of it known as the Bordering method [27]; these were explained in detail in chapter 2 and Appendix C. Curiously, and perhaps satisfactorily, both bordering algorithms give the same result as the last Wynn approximants. Unless otherwise specified, we use 4 Wynn cycles for the 10-cells expansion, 2 Wynn cycles for 7-cells expansion and 6 Wynn cycles for the 14-sites expansion for interacting hard-core bosons on the kagome lattice.

The procedure is as follows: each of the partial sums s_i in (2.39) correspond to the calculation of some thermodynamic quantity P via the basic linked cluster expansion equation (2.2) at order (explained in 2.1.2) i. Thus we obtain a sequence of partial sums for a range of i values; this is then extrapolated using Wynn's algorithm and Brezinski's bordering techniques described in section 2.4.3 to push down the temperature range of convergence. The desired observable $P(c)$ appearing in (2.3) for every finite cluster is computed by determining all the eigenvalues of the Hamiltonian in question on the cluster c using the exact diagonalization technique outlined in section 2.3.

6.2.1 Thermodynamic quantities

In this chapter most of our analysis will be carried out within the grand canonical ensemble i.e. the chemical potential μ is a free variable and our system will access states with all possible occupation densities for every finite cluster. This will enable us, via an inversion of variables through the Legendre transformation, to later inspect the system properties at a fixed density, which is relevant for bosonic systems in cold atom experiments. The partition function in the grand canonical ensemble at inverse

temperature $\beta = 1/T$ for the cluster c is given by

$$\mathcal{Z}(c) = \sum_l \exp\left[-\beta\left(\epsilon_l^{(c)} - \mu n_l^{(c)}\right)\right],\tag{6.1}$$

where the states in the cluster are labelled by l, the eigenvalue by $\epsilon_l^{(c)}$, and the number of particles in the state l by $n_l^{(c)}$. The observable $P(c)$ is computed as

$$P(c) = \frac{\sum_l P_l \exp\left[-\beta\left(\epsilon_l^{(c)} - \mu n_l^{(c)}\right)\right]}{\mathcal{Z}(c)}.\tag{6.2}$$

Eigenvalues and eigenvectors of three simple clusters are computed and indicated in table 6.1 for the interacting hard-core boson model at particular values of V/t and μ/t for illustrative purposes.

Table 6.1: Eigenvalues and eigenvectors for three clusters for all particle fillings at $V/t = 0.5$, $\mu/V = 0$, $t = 1$. Numbers within the ket indicate the number of bosons on each site.

Cluster c	Eigenvalue $\epsilon_l^{(c)}$	Eigenvector
●	0	$|0\rangle$
	0	$|1\rangle$
●—●	0	$|0,0\rangle$
	-1	$0.707|0,1\rangle + 0.707|1,0\rangle$
	1	$0.707|0,1\rangle - 0.707|1,0\rangle$
	0.5	$|1,1\rangle$
●—●—●	0	$|0,0,0\rangle$
	-1.414	$-0.5|1,0,0\rangle - 0.5|0,0,1\rangle - 0.707|0,1,0\rangle$
	0	$-0.707|1,0,0\rangle + 0.707|0,0,1\rangle$
	1.414	$-0.707|0,1,0\rangle + 0.5|1,0,0\rangle + 0.5|0,0,1\rangle$
	-1.186	$0.454|1,1,0\rangle + 0.454|0,1,1\rangle + 0.766|1,0,1\rangle$
	0.5	$-0.707|1,1,0\rangle + 0.707|0,1,1\rangle$
	1.686	$-0.542|1,1,0\rangle - 0.542|0,1,1\rangle + 0.643|1,0,1\rangle$
	1	$|1,1,1\rangle$

Particle density and compressibility

Having determined the partition function in (6.1), we may use equation (6.2) to compute other thermodynamic quantities. The easiest is the particle density

$$\begin{aligned}
\rho &= \frac{1}{\beta}\frac{\partial \log \mathcal{Z}}{\partial \mu} \\
&= \frac{1}{\mathcal{Z}}\sum_l n_l \exp\left(-\beta(\epsilon_l - \mu n_l)\right).
\end{aligned}\tag{6.3}$$

We need not perform the differentiation in the first line of the above formula because within linked cluster expansions, the second line of the above formula may be readily evaluated. This may be performed for a wide range of chemical potentials so as to obtain the region in phase space where the system has all possible filling factors for every temperature range of interest. From the particle density, we may evaluate the compressibility of the system i.e. how easily the density of the system can be changed via a small change in the chemical potential. In a phase where a finite particle gap exists, the compressibility is therefore zero; else it is finite. The compressibility we calculate is taken to be

$$
\begin{aligned}
K &= \left(\frac{\partial \rho}{\partial \mu}\right)_T \\
&= \beta \left(\langle \mathcal{N}^2 \rangle - \langle \mathcal{N} \rangle^2\right),
\end{aligned}
\tag{6.4}
$$

where $\mathcal{N}$ is the operator $\sum_i \hat{n}_i$ measuring the number of particles in the system, and the angular averages are taken in the grand canonical ensemble as in (6.1). Again within linked cluster expansions, we may directly compute the compressibility using the second line of (6.4). We will henceforth denote the mean square fluctuations, appearing in (6.4), of an operator O as $\langle \Delta O^2 \rangle$.

Energy and entropy

The internal energy of the system is the expectation value of the Hamiltonian without the chemical potential terms

$$
\langle \tilde{\mathcal{H}} \rangle \equiv \langle \mathcal{H} + \mu \mathcal{N} \rangle = \frac{1}{\mathcal{Z}} \sum_l \epsilon_l \exp\left(-\beta(\epsilon_l - \mu n_l)\right).
\tag{6.5}
$$

The entropy per site of the system, in units of the Boltzmann constant k_B, is given at temperature $T = 1/\beta$ by

$$
\begin{aligned}
S &= -\frac{\partial F}{\partial T} \\
&= \log \mathcal{Z} + \beta \langle \mathcal{H} \rangle,
\end{aligned}
\tag{6.6}
$$

where $F = -T \log \mathcal{Z}$ is the free energy of the system.

Specific heat and Grüneisen parameter

The constant volume specific heat at any chemical potential μ and temperature T values may be determined from the entropy and particle number by the formula [128]

$$
C_v(\mu, T) = T\left(\frac{\partial S}{\partial T}\right)_\mu - \frac{T\left(\frac{\partial S}{\partial \mu}\right)_T^2}{K}.
\tag{6.7}
$$

The equation (6.7) may be modified to a form more amenable to our calculations as follows, culminating in (6.12). From (6.6), we get

$$
T\left(\frac{\partial S}{\partial T}\right)_\mu = \langle \Delta \mathcal{H}^2 \rangle,
\tag{6.8}
$$

and

$$T\left(\frac{\partial S}{\partial \mu}\right)_T = \left(\frac{\partial \langle \tilde{\mathcal{H}} \rangle}{\partial \mu}\right)_T - \mu\left(\frac{\partial \rho}{\partial \mu}\right)_T, \tag{6.9}$$

where $\langle \tilde{\mathcal{H}} \rangle$ was defined in (6.5). Using (6.4), (6.8) and (6.9) in (6.7), we get

$$C_v(\mu, T) = \frac{\langle \Delta \tilde{\mathcal{H}}^2 \rangle}{T^2} - \frac{1}{T}\frac{\left(\frac{\partial \langle \tilde{\mathcal{H}} \rangle}{\partial \mu}\right)_T^2}{\left(\frac{\partial \rho}{\partial \mu}\right)_T}, \tag{6.10}$$

which is equation 11 in Ref. [9]. This may be further simplified by using $\left(\frac{\partial S}{\partial \mu}\right)_T = \left(\frac{\partial \rho}{\partial T}\right)_\mu$ [128] and

$$\left(\frac{\partial \rho}{\partial T}\right)_\mu = \frac{\langle \Delta (\mathcal{H N}) \rangle}{T^2}; \tag{6.11}$$

the latter may be obtained by differentiating (6.3) with respect to temperature T. This leads to the simplified formula for the specific heat

$$C_v(\mu, T) = \frac{1}{T^2}\left[\langle \Delta \mathcal{H}^2 \rangle - \frac{\langle \Delta (\mathcal{H N}) \rangle^2}{\langle \Delta \mathcal{N}^2 \rangle}\right]. \tag{6.12}$$

The distinct advantage of using formula (6.12) is that it avoids numerical differentiation of thermodynamic quantities as in (6.7) or (6.10), thus doing away with that much bit of numerical noise inextricably associated with the procedure of numerical differentiation. A related quantity of interest, also obtainable from the entropy, is the Grüneisen parameter, which is defined by [129]

$$\Gamma(T, r) = -\frac{1}{T}\frac{\left(\frac{\partial S}{\partial \mu}\right)_T}{\left(\frac{\partial S}{\partial T}\right)_\mu} \tag{6.13}$$

where r is some parameter that measures the deviation from a critical point in the model; in our case, $r = \frac{\mu - \mu_c}{\mu_c}$, with the subscript c indicating a critical value. Proceeding as before, (6.13) may be simplified so that differentiation is avoided to give

$$\Gamma(T, r) = -\frac{\langle \Delta (\mathcal{H N}) \rangle}{\langle \Delta \mathcal{H}^2 \rangle}. \tag{6.14}$$

The authors of [129] argue that the Grüneisen parameter will scale with temperature T as

$$\Gamma(T, 0) \propto T^{-\left(\frac{1}{\nu z}\right)} \tag{6.15}$$
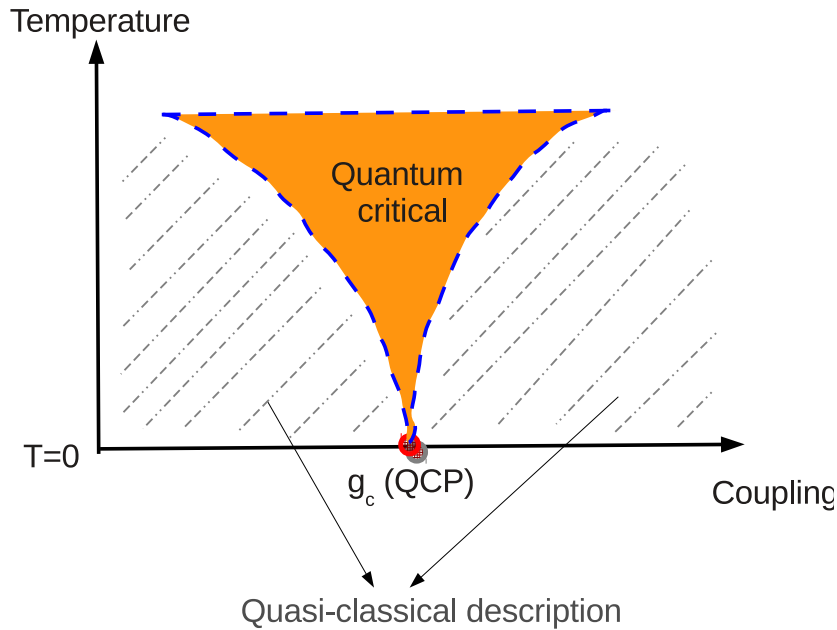
Figure 6.2: Generic phase diagram showing the extent of a quantum critical region into finite temperatures due to the presence of a quantum critical point at zero temperature. A classical description of the phases within this fan will not be sufficient to explain their properties.

at the critical point $r = 0$ or more accurately within the quantum critical fan; ν is the coherence length critical exponent and z is the dynamical exponent measuring asymmetry between space and time directions. The quantum critical fan is illustrated in Fig. 6.2 in orange (dark); in this region of phase space, the quantum nature of the model persists to finite temperatures due to the presence of a quantum critical point at zero temperature. Outside this region a quasi-classical description of the phases will suffice. It is indeed an astonishing character of the quantum critical point that it presents itself as a singularity in the phase diagram, with its effects permeating to finite temperatures which are oftentimes accessible to experiments. Therefore a study of the quantum critical point can afford vital information about the phases within this quantum critical fan and vice versa.

6.3 One dimensional lattice

For one dimensional chains, the hard-core boson model (5.5) is integrable for any ratio of interaction to hopping i.e. $V/t = 0 \rightarrow \infty$. We first investigate the Ising limit and then the limit $V = -t/2$, which is simply the isotropic Heisenberg limit; in each case the exact solutions for certain thermodynamic quantities are compared with numerical linked cluster expansion results. In the Ising limit, a simple transfer matrix solution can readily provide explicit expressions for the partition function and hence any thermodynamic quantity. Away from the Ising limit, the thermodynamic Bethe ansatz method will be employed for which we merely provide the necessary telegraphic recipe. For further details, the intrepid reader is directed to Ref. [130] and the references therein.

6.3.1 Ising limit

In the Ising limit, the interacting hard-core boson Hamiltonian in (5.5) is described by

$$\mathcal{H}_I = V \sum_{<i,j>} \hat{n}_i \hat{n}_j - \mu \sum_i \hat{n}_i, \tag{6.16}$$

with the inter-site hopping amplitude t set to 0. This is the limit when $V/t = \infty$ and is equivalent to the Ising spin-1/2 model in a longitudinal magnetic field as seen from the mapping between hard-core bosons and spins in (5.4).

Certain properties in this Ising limit of similar lattice models can often be solved exactly at $\mu/V = z/2$ [52, 58, 131], with z being the number of nearest neighbours, for two dimensional lattices. In fact for one dimensional chains away from the Ising limit for any anisotropy and filling, the hard-core boson model is integrable [130]. However an exact solution neither subsumes everything there is to be known about the system like correlation functions nor does it imply the ability to get exact results for any parameter range.

In the one dimensional Ising lattice model, we may exactly solve (6.16) via a transfer matrix method [132] formulated for the corresponding spin system. The partition function of (6.16) at inverse temperature β is given by

$$\mathcal{Z}_I = \sum_{\{n\}} \exp\left[-\beta(Vn_1n_2 + Vn_2n_3 + Vn_3n_4 + \ldots - \mu n_1 - \mu n_2 - \mu n_3 - \ldots)\right], \tag{6.17}$$

with $\{n\}$ indicating all possible arrangements of bosons over the N sites of the chain. Introducing the "transfer" matrix

$$P = \begin{pmatrix} 1 & \exp(\beta\mu/2) \\ \exp(\beta\mu/2) & \exp(-\beta(V-\mu)) \end{pmatrix}, \tag{6.18}$$

so that $\langle n_i|P|n_j\rangle = P_{n_i,n_j}$, where $n_i = 0, 1$ denotes the absence or presence of a boson. Then (6.17) may be written as

$$
\begin{aligned}
\mathcal{Z}_I &= \sum_{\{n\}} \Pi_{i=0}^{N-1} P_{n_{i(\text{mod}N)},n_{(i+1)(\text{mod}N)}} \\
&= \sum_{\{n\}} \Pi_{i=0}^{N-1} \langle n_{i(\text{mod}N)}|P|n_{(i+1)(\text{mod}N)}\rangle \\
&= \sum_{n_0} \langle n_0|P^N|n_0\rangle \\
&= \text{Tr}P^N = \sum_i \lambda_i^N.
\end{aligned}
\tag{6.19}
$$

The final summation runs over all eigenvalues λ_i of the matrix P in (6.18). In the thermodynamic limit as $N \to \infty$, the dominant λ dominates in (6.19). This gives the logarithm of the partition function per site as

$$\log\left(\mathcal{Z}_I\right) = \log\left[\exp(\beta(\mu - V)) + 1 + \sqrt{4\exp(\beta\mu) + (\exp(\beta(\mu - V)) - 1)^2}\right] - \log 2. \tag{6.20}$$
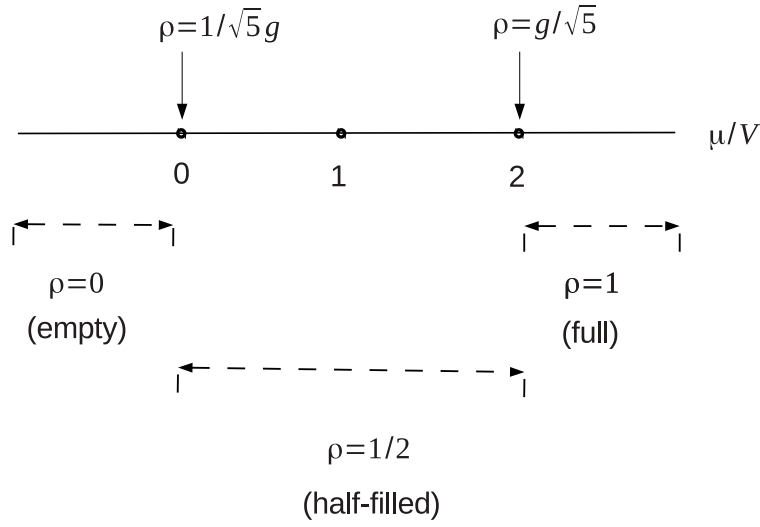
Figure 6.3: Phases of the one dimensional chain of hard-core bosons with no inter-site hopping modelled by (6.16) in the ground state $\beta = \infty$; $g = \dfrac{1 + \sqrt{5}}{2}$ is the golden ratio. Inclusion of hopping results in finite extent of the indicated phases as shown in 5.6b.

The particle density is then given

$$\rho = \frac{1}{\beta} \frac{\partial \log (\mathcal{Z}_{\mathrm{I}})}{\partial \mu}$$

$$= \frac{\left\{ \exp \left(\beta(\mu - V) \right) + \dfrac{\left[\exp \left(\beta(\mu - V) \right) - 1 \right] \exp \left(\beta(\mu - V) \right) + 2\exp(\beta\mu)}{\sqrt{4\exp(\beta\mu) + \left(\exp \left(\beta(\mu - V) \right) - 1 \right)^2}} \right\}}{\exp \left(\beta(\mu - V) \right) + 1 + \sqrt{4\exp(\beta\mu) + \left(\exp \left(\beta(\mu - V) \right) - 1 \right)^2}}. \tag{6.21}$$

In the ground state i.e. $\beta = \infty$, (6.21) may be evaluated to give the densities for the full range of chemical potentials μ at a given repulsive strength V. For $\mu/V < 0$, an empty lattice with $\rho = 0$ is formed while for $\mu/V > 2$ a full lattice is obtained; both are incompressible phases. In between the two limits, a half-filled incompressible phases arises. Just at the first order transition points (as indicated in Fig. 3.6), the densities jump and take finite values of $\dfrac{1}{\sqrt{5}g}$ and $\dfrac{g}{\sqrt{5}}$, where $g = \dfrac{1 + \sqrt{5}}{2}$ is the golden ratio. Addition of inter-site hopping terms will result in a finite extension of these phases and a surrounding superfluid phase as shown in Fig. 5.6b of the previous chapter.

Using the exact expression (6.20) for the partition function of the one dimensional chain, we compute the specific heat (6.7) and the Grüneisen parameter (6.13) at $\mu/V = 0$. This system is taken as a test-bed and compared with the 10-bond NLCE calculations that employ the equivalent expressions (6.12) and
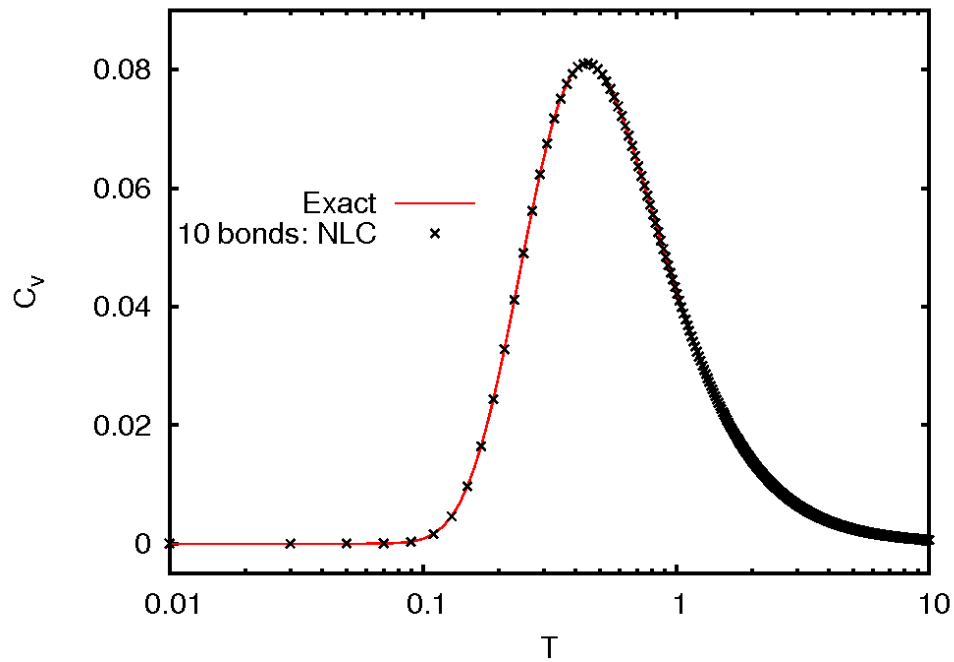
(a)
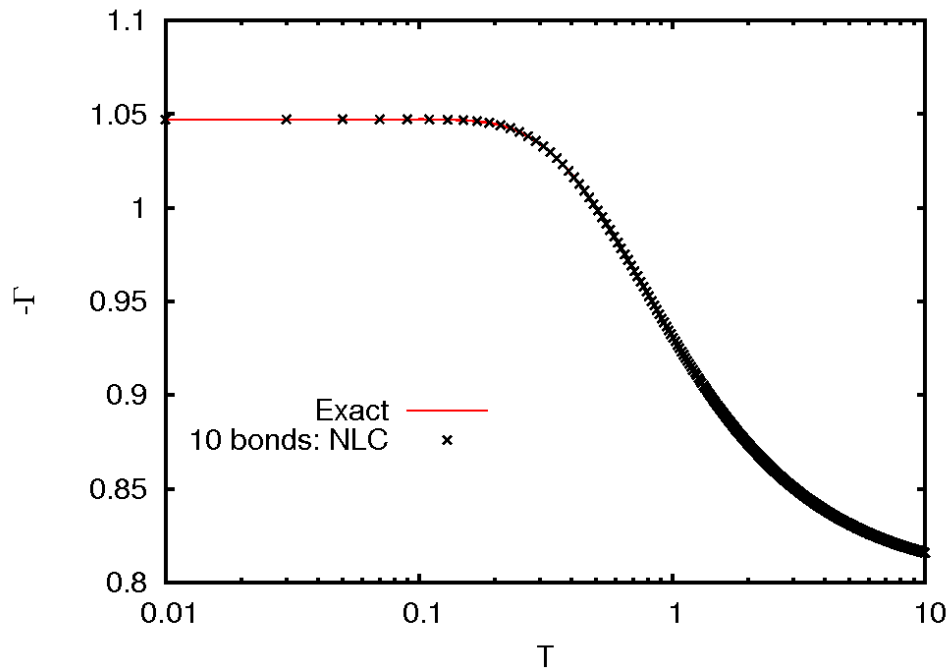
(b)

Figure 6.4: (a) Specific heat at constant volume for the one dimensional Ising chain of hard-core bosons at $\mu/V = 0$ using a 10-bond numerical linked cluster expansion (black symbols) and the exact solution (red line) as a function of temperature T. (b) Grüneisen parameter for the same system.

(6.14); the comparisons are shown in Figs. 6.4a and 6.4b.

6.3.2 Anisotropic limit

Away from the Ising limit when $V/t \neq \infty$, the hard-core boson model may be solved for any filling and temperature on the linear chain. Here we consider the case $V/t = -1/2$, which is the isotropic antiferromagnetic Heisenberg model on a linear chain. We employ NLCE in this one dimensional spin-1/2 model which may be solved exactly using the thermodynamic Bethe ansatz (TBA) method at any temperature. We recapitulate a simplified presentation [130] of the latter approach that utilizes only a single complex integral equation to be solved.

For a spin-1/2 Hamiltonian on a chain of N sites, the Hamiltonian is described by

$$\mathcal{H}(J, \Delta, h) = -J \sum_{l=1}^{N} \left[\hat{S}_l^x \hat{S}_{l+1}^x + \hat{S}_l^y \hat{S}_{l+1}^y + \Delta \left(\hat{S}_l^z \hat{S}_{l+1}^z - \frac{1}{4} \right) \right] - 2h \sum_{l=1}^{N} \hat{S}_l^z, \tag{6.22}$$

where the $\hat{S}_l^k$ are the usual spin-1/2 Pauli operators at site l and direction $k = x, y, z$. Defining the auxiliary variables

$$\phi = \cosh^{-1} \Delta, Q \equiv \pi/\phi,$$

$$s(x) = \frac{1}{4} \sum_{n=-\infty}^{\infty} \operatorname{sech} \frac{\pi(x - 2nQ)}{2}, \text{ and}$$

$$a_1(x) = \frac{\phi \sinh \phi / 2\pi}{\cosh(\phi) - \cos(\phi x)}, \tag{6.23}$$

the equation to be solved at temperature T becomes

$$u(x) = 2 \cosh(h/T) + \oint_C \frac{\phi}{2} \left\{ \cot\left(\frac{\phi}{2}[x - y - 2i]\right) \exp\left[\frac{2\pi J \sinh \phi}{T\phi} a_1(y + i)\right] \right.$$

$$\left. + \cot\left(\frac{\phi}{2}[x - y + 2i]\right) \exp\left[\frac{2\pi J \sinh \phi}{T\phi} a_1(y - i)\right] \right\} \frac{1}{u(y)} \frac{dy}{2\pi i}. \tag{6.24}$$

The free energy is then given by $f = -T \log u(0)$. The integral equation in (6.24) may be solved by fixed point iteration over a circle of suitable radius r (such that convergence is assured at all temperatures) within a complex plane grid. The central value $u(0)$ will simply be the average over the circle. Generally 1000 iterations ensure convergence.

Solving the above equation for the isotropic antiferromagnetic Heisenberg chain i.e. *XXX* spin-1/2 model for $\mathcal{H}(-1, 1, 0)$, we compare the free energy with that obtained by a 14-site numerical linked cluster expansion in Fig. 6.5. We remark that although it may be possible to push down the temperature scales of convergence of the TBA compared to our solution, the implicit integral in (6.24) will anyhow have a lower temperature limit of convergence largely determined by Δ. In the present case, we see that the NLCE fares better down to lower temperature range.

6.4 Kagome lattice

For the two dimensional case, the Ising spin model on the kagome lattice in zero longitudinal magnetic field ("half-filling" in terms of hard-core bosons) is exactly soluble [52] and found to be disordered at all
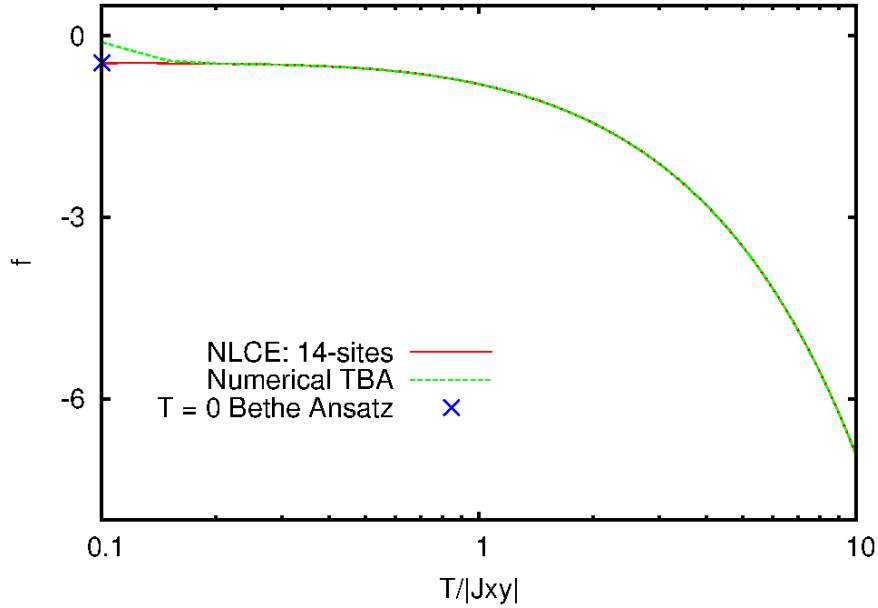
Figure 6.5: Free energy f versus temperature T of the isotropic antiferromagnetic Heisenberg spin-1/2 chain using thermodynamic Bethe ansatz, and a numerical linked cluster expansion of 14 sites. The exact ground state energy from the Bethe ansatz [133] is shown as a cross.

temperatures. By decimating spins appropriately, this can be mapped to a symmetrical 16-vertex model on the square lattice [134], which is in turn a subclass of the 8-vertex model [135], whose free energy is exactly representable by a relatively simple integral [136]. But upon going away from half-filling i.e. adding a longitudinal magnetic field in the spin system, the Ising problem is no longer tractable exactly except at certain critical external field strengths (see next section). Thus, away from half-filling, numerical simulations are called for even in the Ising limit.

The Ising spin model at zero field is equivalent, via the spin-boson mapping (5.4) described in chapter 5, to the Ising limit of the hard-core boson model at half-filling i.e. $\mu/V = 2$ in (6.16). In this section, we formulate the equivalence between the Ising spin model on the kagome lattice at zero external field and the symmetrical 16-vertex model; the exact solutions of the latter's partition function and NLCE calculations of the former will be compared.

6.4.1 Ising limit: half-filled system

In this section, we consider the Ising spin model at zero longitudinal field. Effectively we are considering the hard-core boson model in the Ising limit and half-filling, and clarify its integrable nature. Our discussion will combine the results of Refs. [134–136].

16-vertex model

Consider the general 16-vertex model with the weights $\omega_1, \omega_2 \cdots \omega_{16}$. In this model on a square lattice, there are two states associated with each edge connecting two vertices on the lattice; these are represented by up/down or right/left arrows for the vertical or horizontal edges as depicted in Fig. 6.6. The

model can be represented by the matrix

$$\boldsymbol{\Omega} = \begin{pmatrix} \omega_1 & \omega_{16} & \omega_{12} & \omega_8 \\ \omega_{13} & \omega_4 & \omega_6 & \omega_{10} \\ \omega_9 & \omega_5 & \omega_3 & \omega_{14} \\ \omega_7 & \omega_{11} & \omega_{15} & \omega_2 \end{pmatrix}. \tag{6.25}$$

The ordering is based on the various representations of the 16 configurations of the arrows at any site shown in Fig. 6.6 and is as follows [135]: every 2×2 submatrix ω of (6.25) starting from the top-left and proceeding clockwise has the same orientation of the vertical arrows in Fig. 6.6; and within each submatrix ω, the horizontal arrows follow the same pattern of changes proceeding clockwise from top-left. ω_k is the Boltzmann weight associated with each configuration and the partition function of the model is given by

$$\mathcal{Z} = \sum_C \prod_{i,j} \omega_{i,j}. \tag{6.26}$$

Here i, j run through the lattice points and C is the configuration space of all allowed up-down-left-right configurations of arrows. It was shown in Ref. [135] that the partition function $\mathcal{Z}(\boldsymbol{\Omega})$ is invariant under the general similarity transformation

$$\boldsymbol{\Omega} \to \boldsymbol{\Omega}' = \left(S^{-1} \bigotimes T^{-1} \right) \boldsymbol{\Omega} \left(S \bigotimes T \right). \tag{6.27}$$

Here the 2×2 T matrix acts on the horizontal arrows while the 2×2 S matrix acts on the vertical arrows.

But because the partition function is independent of the frame of reference, $\mathcal{Z}$ cannot depend on all 16 vertex weights separately, but only on those combinations of parameters which are invariant under the application of arbitrary rotations. By suitably grouping elements so that one element transforms as a scalar, two elements transform like 3-vectors and the last nine grouped into a 3×3 matrix, it can be shown that only 10 such invariants can exist [135]. This is called the standard representation, where the elements satisfy (Condition I):

$$
\begin{aligned}
\omega_5' &= \omega_6', \\
\omega_7' &= \omega_8', \\
\omega_9' &= \omega_{11}', \\
\omega_{13}' &= \omega_{15}', \\
\omega_{10}' &= \omega_{12}', \\
\omega_{14}' &= \omega_{16}'.
\end{aligned} \tag{6.28}
$$

8-vertex and symmetrical 16-vertex model

The general 8-vertex model is gotten by setting (Condition II)

$$\omega_9 = \cdots = \omega_{16} = 0. \tag{6.29}$$

In the standard representation, both the Conditions I and II in (6.28) and (6.29) are satisfied. As a subclass of this general 8-vertex model, we obtain the symmetrical 16-vertex model using the trans-
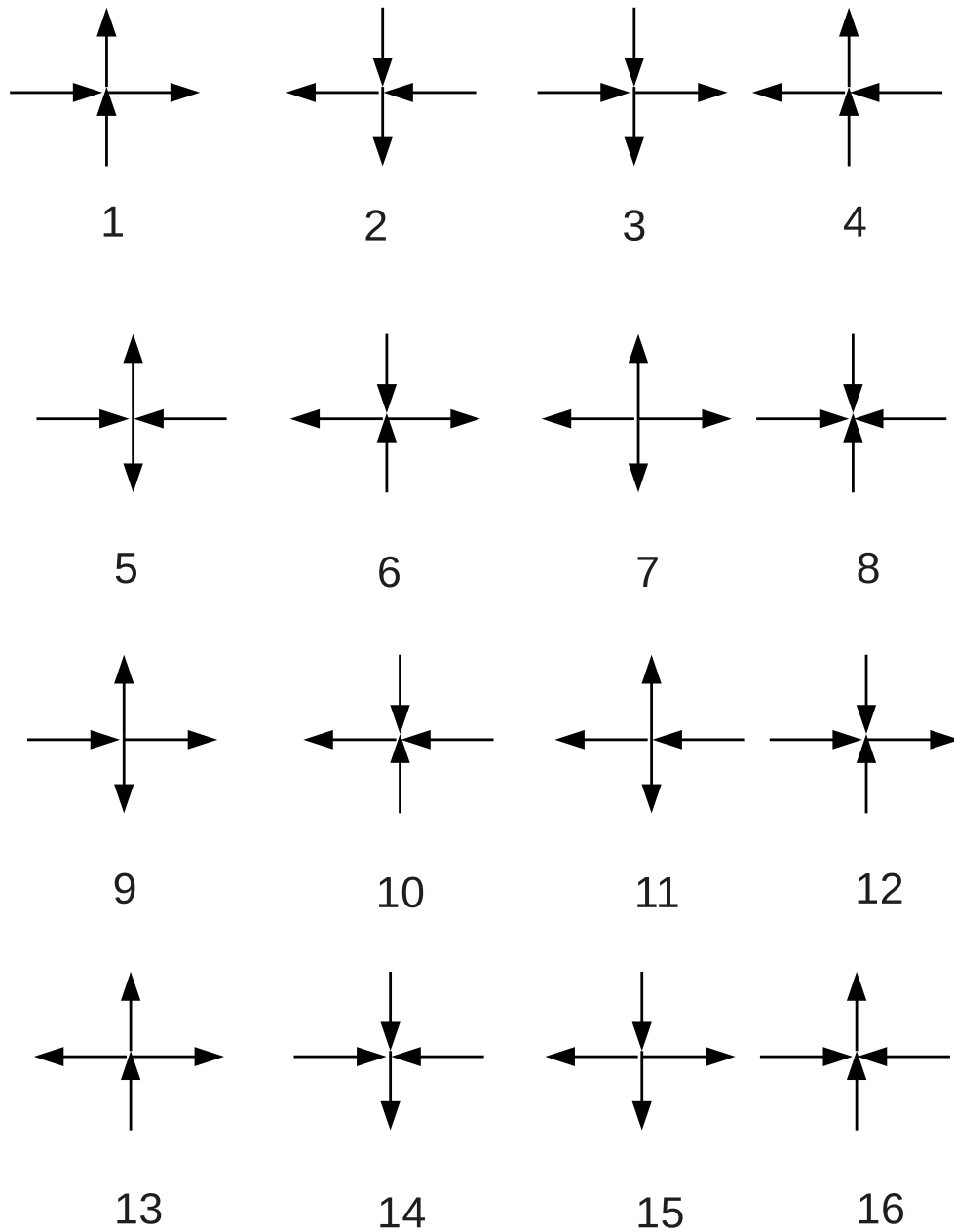
Figure 6.6: Configurations of the 16 vertex model numbered 1 to 16, as used in the matrix representation (6.25).

formation matrices of (6.27) as

$$S = T = \frac{1}{\sqrt{2}} \begin{pmatrix} 1 & -1 \\ 1 & 1 \end{pmatrix}. \tag{6.30}$$

This then may be readily seen to give the following relations between the weights in the symmetrical 16-vertex model:

$$
\begin{aligned}
\omega_1^{(16)} &= \omega_2^{(16)}, \\
\omega_3^{(16)} &= \omega_4^{(16)}, \\
\omega_5^{(16)} &= \omega_6^{(16)}, \\
\omega_7^{(16)} &= \omega_8^{(16)}, \\
\omega_9^{(16)} &= \omega_{10}^{(16)} = \omega_{11}^{(16)} = \omega_{12}^{(16)}, \\
\omega_{13}^{(16)} &= \omega_{14}^{(16)} = \omega_{15}^{(16)} = \omega_{16}^{(16)}.
\end{aligned}
\tag{6.31}
$$

Free fermion condition

If in the 8-vertex model, the variables additionally satisfy

$$
\omega_1\omega_2 + \omega_3\omega_4 = \omega_5\omega_6 + \omega_7\omega_8,
\tag{6.32}
$$

then it is exactly solvable [136] and is called the free fermion condition (Condition III). Then the free energy is given by

$$
\beta f = -\frac{1}{8\pi^2} \int_0^{2\pi} \int_0^{2\pi} g(\theta, \phi)\, d\phi\, d\theta,
\tag{6.33}
$$

with

$$
g(\theta, \phi) = \log\left[2a + 2b\cos\theta + 2c\cos\phi + 2d\cos\overline{\theta - \phi} + 2e\cos\overline{\theta + \phi}\right],
\tag{6.34}
$$

where the auxiliary variables are given by

$$
\begin{aligned}
2a &= \omega_1^2 + \omega_3^2 + \omega_3^2 + \omega_4^2, \\
b &= \omega_1\omega_3 - \omega_2\omega_4, \\
c &= \omega_1\omega_4 - \omega_2\omega_3, \\
d &= \omega_3\omega_4 - \omega_7\omega_8, \\
e &= \omega_3\omega_4 - \omega_5\omega_6.
\end{aligned}
\tag{6.35}
$$

Using the identity

$$
\int_0^{2\pi} \log\left[2A + 2B + 2C\cos\theta\right] d\theta = 2\pi \log\left[A + \sqrt{A^2 - B^2 - C^2}\right],
\tag{6.36}
$$

(6.33) can be converted to a one dimensional integral

$$
\begin{aligned}
\beta f &= -\frac{1}{4\pi} \int_0^{2\pi} \log\left[A + \sqrt{Q(\phi)}\right] d\phi, \\
Q(\phi) &= y^2 + z^2 - x^2 - 2yz\cos\phi + x^2\cos\phi^2, \\
x &= \omega_2\omega_3 - \omega_1\omega_4, \\
2y &= \omega_2^2 - \omega_1^2 - \omega_4^2 + \omega_3^2, \\
z &= \omega_2\omega_3 + \omega_1\omega_4.
\end{aligned}
\tag{6.37}
$$

Mapping to Ising kagome

It was shown in Ref. [134] that the Ising model on the kagome lattice can be mapped (by decimating the central spins in the kagome) onto a symmetrical 16-vertex model, with each vertex corresponding to 3 spins. The corresponding weights are shown to satisfy the free fermion condition (Condition III in (6.32)), and the weights in the equivalent 8 vertex model are [134]

$$
\begin{aligned}
\omega_1 &= \exp(2K)\cosh(4K) + 2\exp(-2K) + \exp(2K) + 4\cosh(2K), \\
\omega_2 &= \omega_1 - 8\cosh(2K), \\
\omega_3 &= \omega_4 = \omega_5 = \omega_6 = \exp(2K)\cosh(4K) - \exp(2K), \\
\omega_7 &= \omega_8 = \omega_1 - 4\cosh(2K) - 4\exp(2K).
\end{aligned}
\tag{6.38}
$$

The free fermion condition may be explicitly checked to hold for the weight variables ω in (6.38). Then (6.33) may be used to calculate the partition function $\mathcal{Z}$; this is seen to compare well with 10-site NLCE calculations for the Ising model on the kagome lattice as shown in Fig. 6.7.
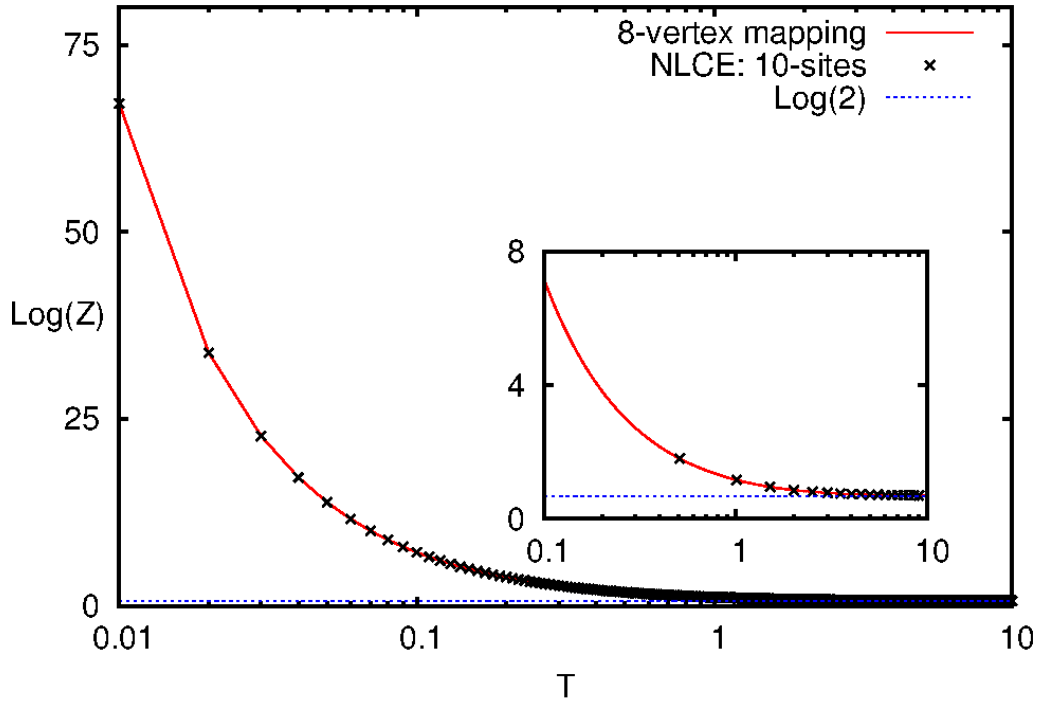
Figure 6.7: Logarithm of the partition function for the antiferromagnetic Ising spin model on the kagome lattice as a function of temperature computed using 10-site NLCE and simulation of the equivalent 8-vertex model. In the HCB language, this is at $\mu/V = 2$ i.e. half-filling.

Alternatively, we may also use (6.37) but with the equivalent symmetrical 16-vertex $\omega_i^{(16)}$ weights, which will satisfy the equivalent free fermion condition

$$
\omega_1^{(16)}\omega_3^{(16)} + \omega_5^{(16)}\omega_7^{(16)} = \omega_9^{(16)}\omega_{11}^{(16)} + \omega_{13}^{(16)}\omega_{15}^{(16)}.
\tag{6.39}
$$

6.4.2 Ising and strong-coupling limits: arbitrary filling

At an arbitrary chemical potential μ/V, there is no exact solution of the Ising limit (6.16) on the kagome lattice. The Fock basis diagonalizes the Hamiltonian readily in the Ising limit and there is no need for an exact diagonalization procedure in this limit. Therefore, we may employ large order expansions; to 10th order in cell expansions, there are in total 120 cell expanded graphs. This may be to taken to produce relatively exact solutions due to the large order of the expansion. In the strong coupling limit $V/t \gg 1$, we employ various expansion schemes which will be explicitly mentioned. For instance, we show in Fig. 6.8a the comparison between the convergence limits of the bare (unextrapolated) series obtained from a 10-cells expansion versus its Wynn extrapolated series for the particle density; we generally use the Wynn series down to the point at which all the Wynn extrapolants begin to move away from each other.

In Fig. 6.8b is shown the temperature dependence of the boson density on the kagome lattice for a range of chemical potentials in the Ising (10-cells expansion) and strong-coupling limit with $V/t = 100$ (14 sites expansion). As such a small hopping amplitude is added to the Ising limit, small fluctuations from the Ising limit are expected; these small fluctuations are expected to be better behaved numerically and hence more amenable to non-linear extrapolation schemes. These fluctuations are then added atop the Ising limit. Alternatively, the strong-coupling limit can be directly simulated. Results of both these techniques are shown in the same figure. The appearance of the 1/3 and 2/3 filled valence bond solid (VBS) phases can be clearly seen at low-T. However, because we see no significant differences between adding fluctuations on top of the Ising limit and direct calculations, we stick to the latter in the rest of this work. As in previous published reports [9], high or low values of fillings converge down to lower temperatures compared to intermediate fillings.

Density

Of all the observables, the boson density is the simplest to obtain once the partition function is evaluated. We make some initial remarks about this from Fig. 6.8b before proceeding further: (a) in the Ising limit, we see a residual density of approximately 0.2 at $\mu/V = 0$, and this occurs concomitantly with a residual entropy (next subsection) at this low-T, and (b) due to the symmetry about the density $n_b \equiv \rho = 1/2$ (we add the subscript to exemplify the bosonic nature of the particles), we need only calculate all observables up to half-filling.

In optical lattices where our forthcoming results should find application and relevance as described in section 6.1, the system is usually kept at fixed densities and not fixed chemical potentials. Therefore we invert the $n_b(\mu/V, T/V)$ (or any other property P) dependence to obtain $\mu(n_b, T/V)$, which is accomplished as follows: the system properties are evaluated for a dense set of chemical potential μ/V and temperature T/V values. Then for the desired fixed density and temperature, we run through this list of computed values and find the μ/V that corresponds to said density and temperature. After this Legendre transformation, the chemical potential dependence on temperature at fixed densities is shown in Fig. 6.9a-6.10a in the Ising limit and strong coupling limit of $V/t = 8$. For very low densities in the Ising limit, there is a clear linear dependence of the chemical potential on the temperature at low-T; we will later see from the specific heat for these same densities that the low-T behaviour fits approximately with those of roton-like quasiparticles as well as a polynomial T-dependence. But at $n_b = 0.15$ the $\mu - T$ dependence changes to a quadratic one, which is reminiscent of Fermi-liquid like behaviour (where the sign of the T^2 coefficient is determined by the quasiparticle mass dependence on the system density [137]). As the hopping is turned on, and close to the zero-T lobe tip $V/t = 8$ [138, 139], we see that such a linear dependence disappears even for low-densities and only (approximately) quadratic fits
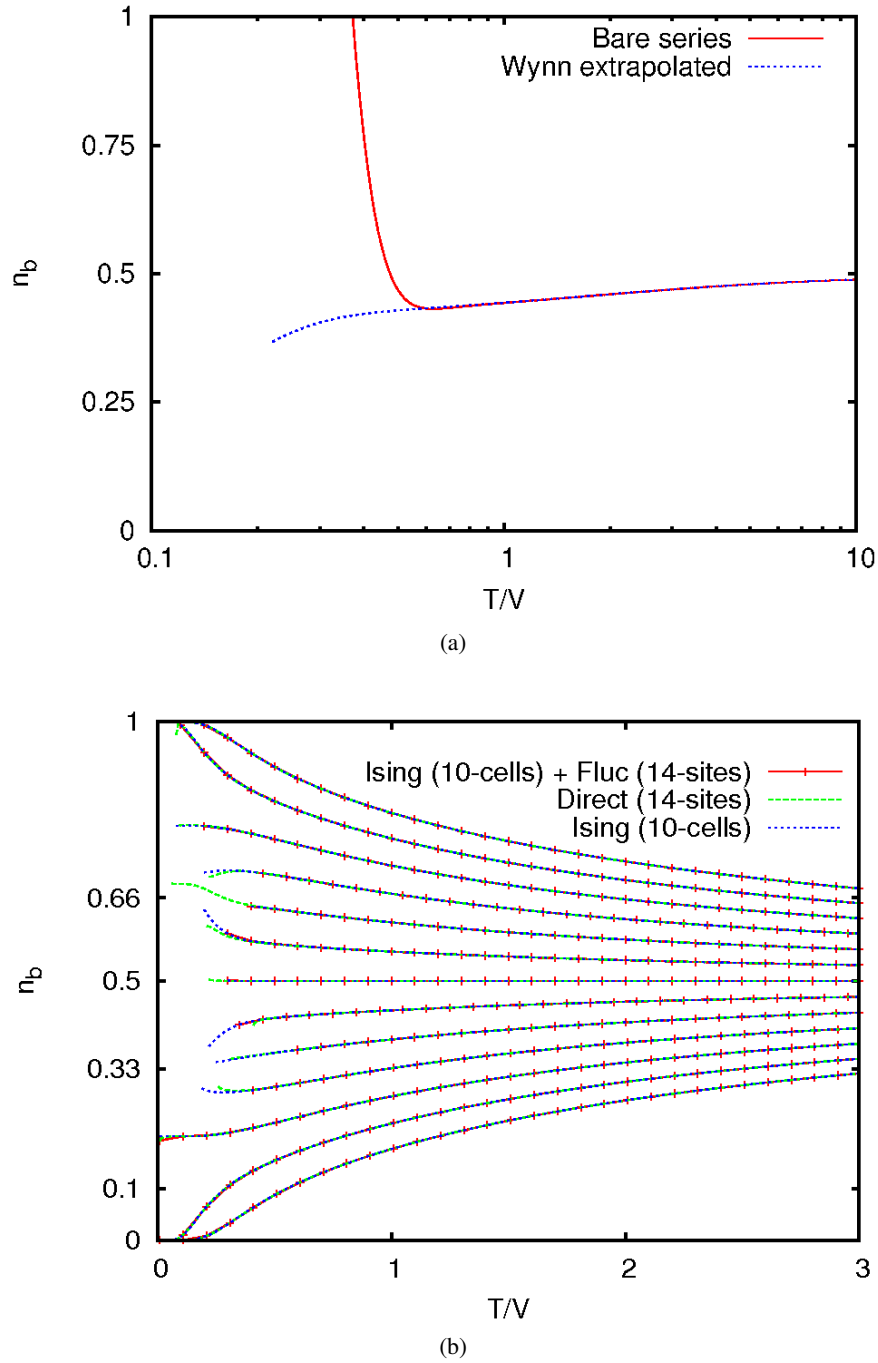
(a)

(b)

Figure 6.8: Particle density in the hard-core boson model on the kagome lattice: (a) In the Ising limit for $\mu/V = 1.5$ with bare and Wynn extrapolated series using a 10-cells expansion. (b) In the Ising (blue-dotted) and strong coupling ($V/t = 100$) limits for various $\mu/V = -1, -0.5 \cdots 5$ from bottom to top. For $V/t = 100$, we implemented the calculations directly (green-dashed) and by adding fluctuations (see text) on top of the Ising limit (red-pointed).

remain.

Inverting the results to constant temperature, we observe from Fig. 6.9b an apparent jump in the density in the Ising limit close to the onset of the 1/3-filled phase at low-T. It is known that at zero-T and

(a)

(b)
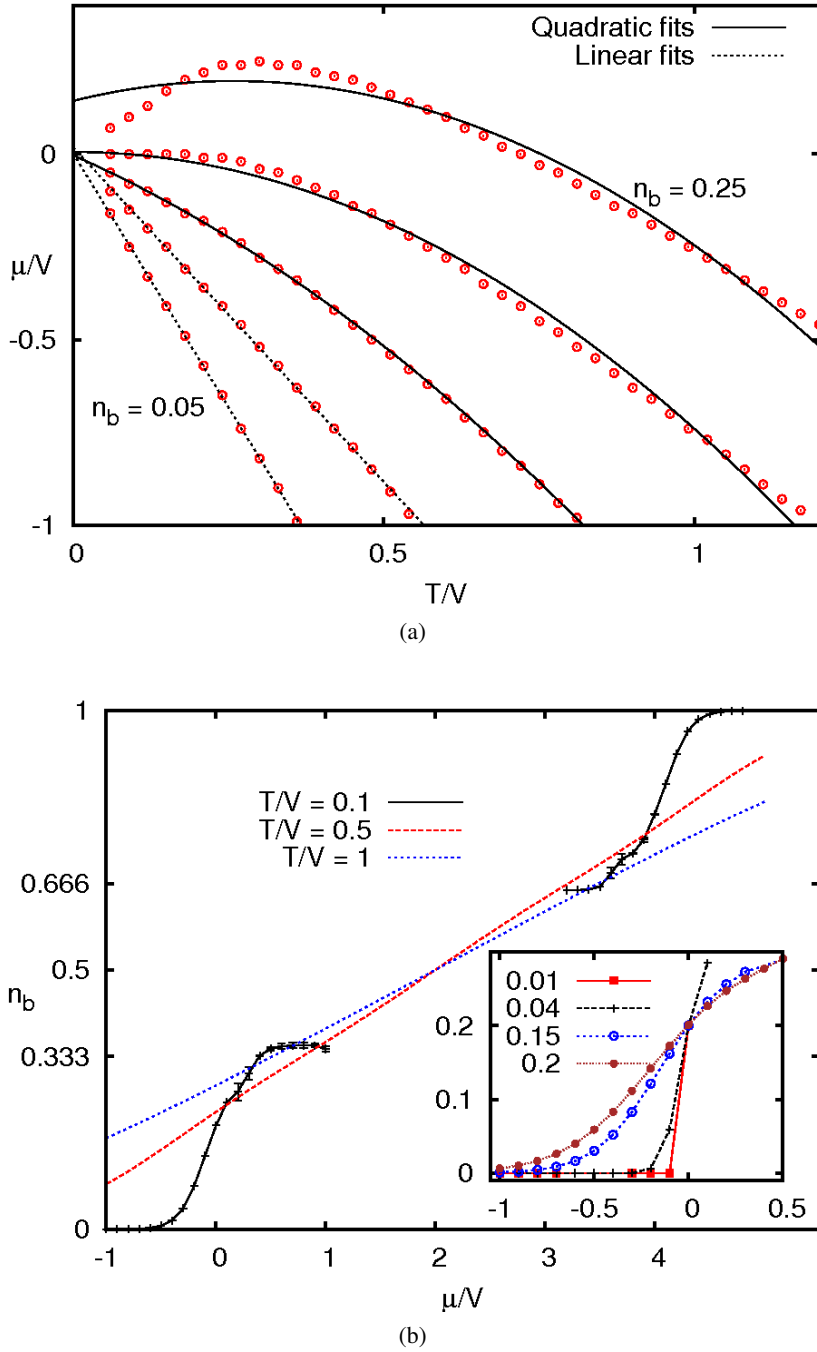
Figure 6.9: Boson density in Ising limit (a) In the Ising limit (using 10-cells), at very low densities ≤ 0.1, there is a clear linear dependency on temperature at low-T which develops into a mildly quadratic temperature dependence at slightly higher densities. (b) Density at fixed-T showing the tendency to jump across the transition, indicative of a first-order transition. We show variation in the Wynn extrapolated quantities across 4 and 5 cycles indicated by bars; the inset shows a zoomed-in version of the $n_b - \mu$ dependence.

finite V/t the transition from the Mott phase to the superfluid across the Pokrovsky-Talapov line [114] is a second-order transition; but then what about the transition in the Ising limit from the Mott phase to the

(a)

(b)
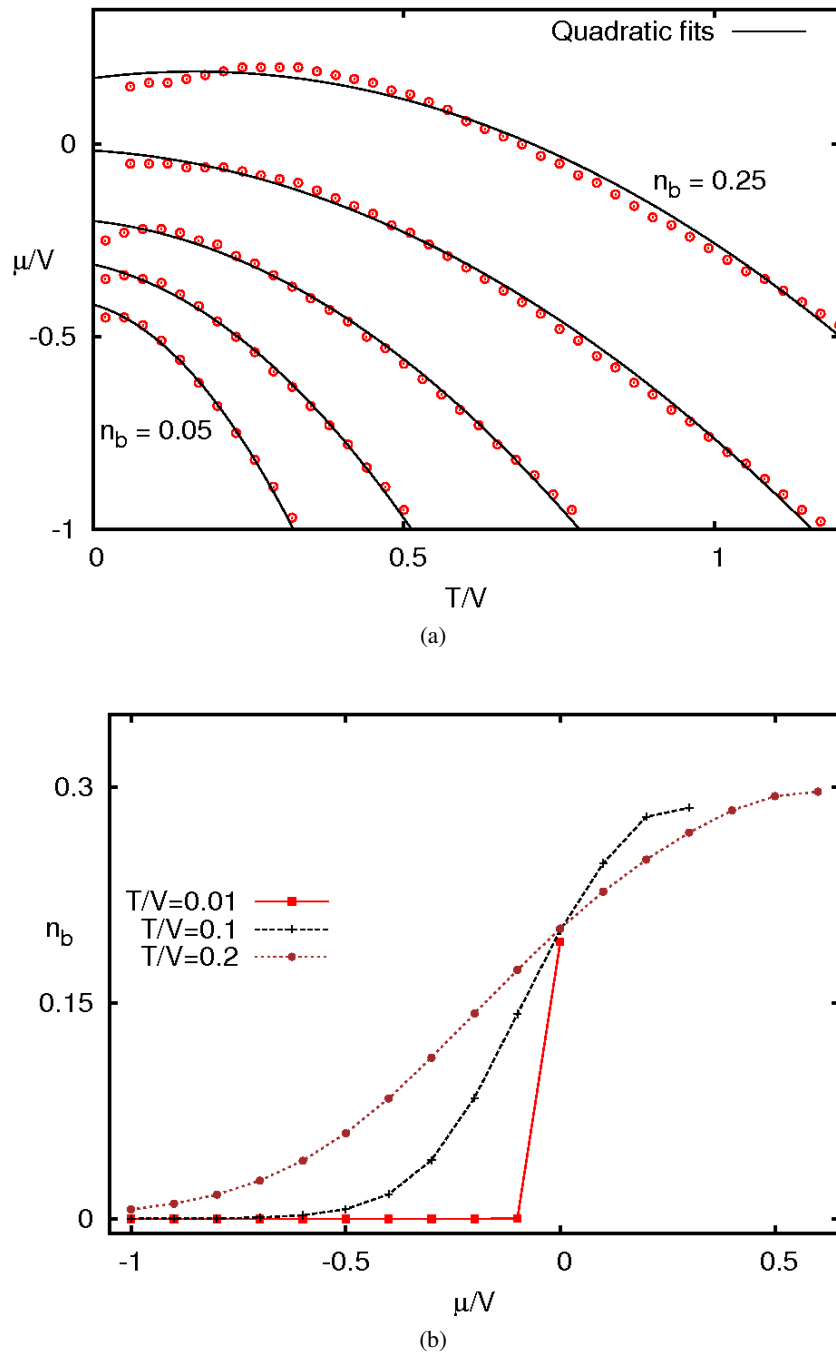
Figure 6.10: Similar to Fig. 6.9 but with $V/t \gg 1$. (a) In the strong coupling limit $V/t = 8$ (14-sites expansion), the linear dependence on T seen in Fig. 6.9a disappears even for very low densities. (b) Density at fixed-T for the strong coupling limit $V/t = 100$, showing the tendency to jump across the transition, indicative of a first-order transition as observed in the Ising limit in Fig. 6.9b.

1/3 phase, or the transition from the superfluid phase to the VBS phase? It seems reasonable to posit that the transition from the empty lattice to the 1/3 phase is a first order transition because the latter is exactly describable by perfect dimer coverings on the hexagonal lattice [140]; the two order parameters

(which quantitatively measure the ordering of phases) are unrelated and this indicates, precluding any other exotic possibilities in the Ising limit, a first order transition. Indeed we compute the densities at constant-T and lower the temperature as shown in Fig. 6.9b; we see a characteristic jump in the density indicative of a first-order transition in the Ising limit.

This may be seen as well by considering the equivalent spin system, the Ising model in a longitudinal field (3.30) on the kagome lattice, with spin-spin interaction J and magnetic field h. We use a 7-cell numerical linked cluster expansion with 2 and 3 Wynn extrapolation cycles to calculate the system's energy at a low temperature $T/J = 0.1$. This is plotted in Fig. 6.11. There are two main regimes of interest in the ground state: (a) a disordered state for $h/J = 0$ [52], and (b) an ordered state for $h/J > 0$ [51], although the ferromagnetic moment is different above $h/J = 4$ from below this value. As seen from Fig. 6.11, there is a cusp in the energy at $h/J = 4$, which we may taken to be indicative of a first order transition as in Ref. [141]. We investigate this further using Grüneisen parameter calculations in a subsequent subsection.
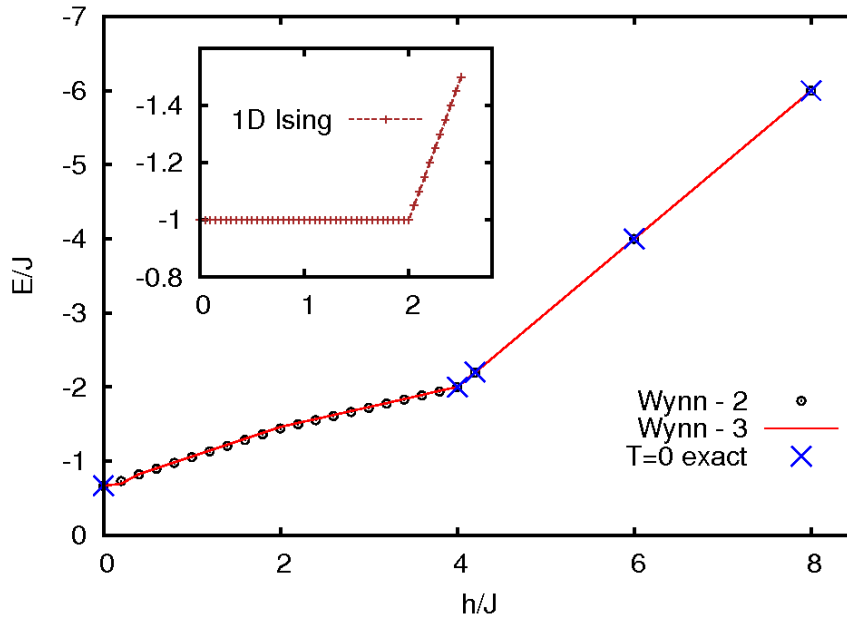
Figure 6.11: Energy of the Ising spin model (3.30) on the kagome lattice for field strength h/J at temperature $T/J = 0.1$. 7-cell numerical linked cluster expansion was employed with 2 (circles) and 3 (lines) Wynn cycles of extrapolation; crosses indicate exact values of the energy at $T/J = 0$, known for $h/J = 0$ and $h/J \geq 4$. At $h/J = 4$ (equivalent to $\mu/V = 0$ in the hard-core boson model (6.16)) there is a cusp in the energy versus field dependence, indicative of a first order transition [141]. Inset shows the situation for the one dimensional Ising spin chain obtainable from (6.20) for the corresponding spin system.

Adding small quantum fluctuations to this phase, the density is still pinned to 1/3 but local resonances in hexagons set in [138, 142]; it was argued [138] that this too exits the solid phase to the superfluid via a first order transition. A jump similar to that in the Ising limit as observed in Fig. 6.9b, although less substantial, is also seen in the strong coupling limit of $V/t = 100$ as plotted in Fig. 6.10b. At $V/t = 100$, because of the presence of a small region of superfluid between the empty lattice and the VBS phases at zero temperature [138], two transitions are expected: a second order transition between the empty lattice and superfluid, and a transition between the superfluid and the VBS. Therefore, solely from the density jump in Fig. 6.10b, nothing specific may be said about the two transitions (specifically the latter

transition) due to their close proximity to each other. The nature of the VBS-superfluid transition will be further investigated using hyperscaling relations in a subsection to follow.

Entropy
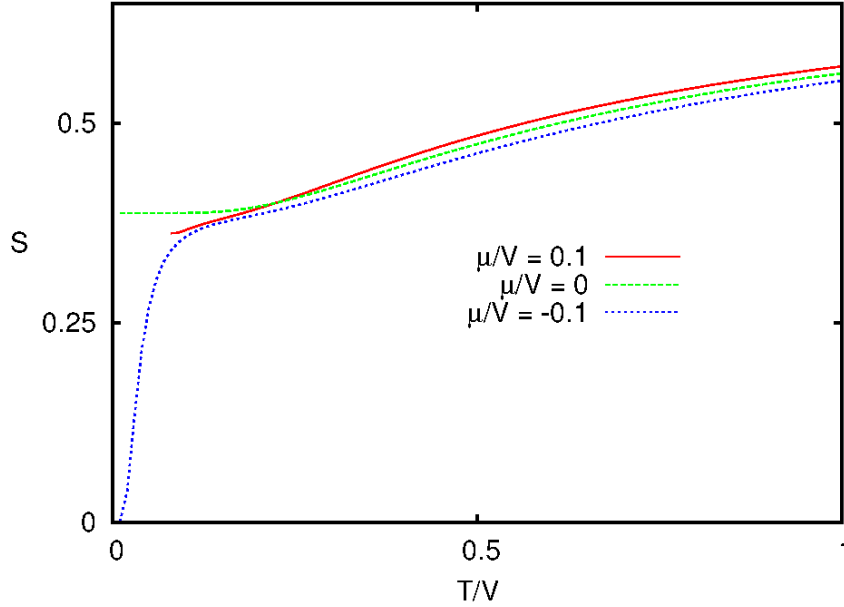
Figure 6.12: (a) Entropy, in k_B units, of the hard-core boson model in the Ising limit at μ/V values close to the transition from the empty lattice to the 1/3 filled phase.

The entropy was defined in (6.6), in units of k_B, and as with the density, is directly amenable to a linked cluster expansion. In the Ising limit, we have already seen in chapter 3 that at the saturation field for the spin model (or at $\mu/V = 0$ for the hard-core boson model), there is a residual entropy associated with degenerate spin flips (or boson creation and annihilation). As shown in Fig. 6.12, there is a drop to zero of the entropy at low temperatures for $\mu/V < 0$ ($T = 0$ empty lattice) and a saturation value right at the transition point $\mu/V = 0$. We may see this more clearly by computing the entropy at constant and low temperatures over a certain range of chemical potentials in the Ising limit as shown in Fig. 6.13. In the Ising limit, a clear peaking and saturation (without accumulation, however) of the entropy is seen about the point $\mu/V = 0$ (PT1) where the system transits from the polarised Mott state to the 1/3 state. In addition to a stronger peak, such a peaking about PT1 persists even in the strong coupling limit as seen in the inset. It is unclear what the stronger peak seen in these strong coupling limits is, visible also for other V/t. This saturation entropy value of ≈ 0.387 for the Ising limit kagome lattice that sets in already at temperature scale $T/V = 0.2$ from the NLCE calculations is in fact within 1.6% of the zero-temperature extensive value calculated by transfer matrix methods and Binder's algorithm in chapter 3. We point out that the comparison between the two approaches for the square and triangular lattices is two orders of magnitude better than in the case of the kagome lattice; it is unclear to us why this is so. That the Ising limit lattices possess an extensive entropy is not a new phenomenon whether in zero external field (in spin model terminology) or at zero chemical potential (in hard-core boson terminology). In table 6.2, we have tabulated the extensive entropy values for various lattices; curiously, it is only for the kagome lattice that the extensive entropy is *higher* at zero field than when away from
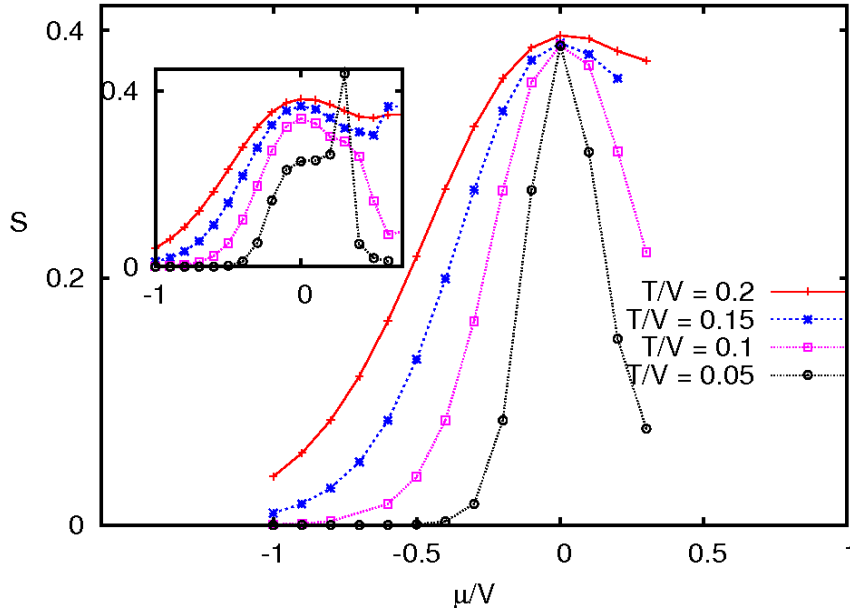
Figure 6.13: Peaking and saturation of entropy at constant temperatures in the Ising limit about the point of phase transition from the empty lattice to the 1/3 phase at $\mu/V = 0$ (PT1). Inset shows entropy for the strong coupling limit $V/t = 10$; some peaking about PT1 is still visible at finite temperatures in addition to a stronger second peak visible at much lower T.

it. Moreover in the Ising limit on the kagome lattice, we present further evidence in the next subsection using Grüneisen parameter calculations that a particular signature indicative of a second order transition, as the system transits from the empty lattice to the 1/3 phase, is absent, an expected result perhaps given our arguments in the previous subsection.

Lattice	$\mu/V = z/2$	$\mu/V = 0$
Kagome	0.502 [52]*	0.387
Square	0	0.407 [64]*
Triangular	0.323 [58]	0.333 [64, 72]*
Linear	0	0.481 [63]*

Table 6.2: Residual entropies, up to three digits, for lattice models in the Ising limits at (right column) or away (left column) from the saturation point. The starred values are known from earlier results and verified by current work. z denotes the number of nearest neighbours.

Grüneisen parameter

The Grüneisen parameter $\Gamma(r, T)$ was defined in (6.13) and reformulated in (6.14). As a test-bed for scaling of the Grüneisen parameter $\Gamma(r, T)$ close to critical points [129] as in (6.15), we calculate $\Gamma(r, T)$ in the Ising limit at $\mu/V = 0$ where the system transits from an empty lattice to a 1/3 filled phase (equivalent to the hard dimer covered hexagon as remarked earlier). We see from Fig. 6.14, using (6.13) with 10-cells and (6.14) with 8-cells, that the best fit with such a form to our calculated Grüneisen

parameter does not quite agree; this suggests that the transition in the Ising limit is indeed a first-order transition unless the regular contributions to Γ dominate over the critical contributions [129]. This analysis validates the well-known point that there cannot be a second-order transition between two ordered states which have unrelated order-parameters. We had provided further support for the first order nature of the transition at this point $\mu/V = 0$ through the density calculations (Fig. 6.9b) and energy calculations (Fig. 6.11).

(a)
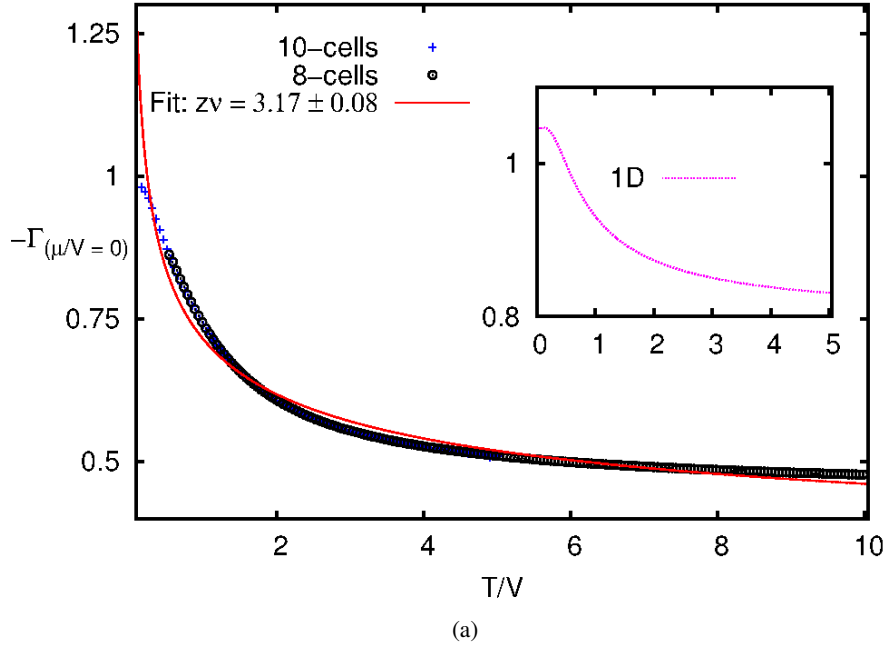
Figure 6.14: Grüneisen parameter calculated using 10-cells (6.13) (up to $T/V = 5$ due to noise in differentiation) and 8-cells with (6.14) at $\mu/V = 0$ does not quite fit to the expected behaviour $\Gamma(0, T) \propto T^{-(1/\nu z)}$, which it would have were it a quantum critical point with no dominant non-critical contributions. Inset shows the low-T saturation of the exact Γ in the 1D case which, similar to the kagome, evidently cannot be captured by a scaling behaviour; the calculation of which was previously illustrated in Fig. 6.4b.

As illustrated in the one dimensional case there is no $T^{-(1/\nu z)}$ scaling because as is known for the transition from the empty lattice to the half-filled Néel state, this is indeed a first-order transition. And similar to the residual density observed at $\mu/V = 0$ in the Ising limit kagome lattice, here too in the one dimensional case a residual density was computed at this phase point as illustrated in Fig. 6.3. Because this occurs concomitantly with a residual extensive entropy, there should be a true ground state degeneracy in this case [128].

But at finite t values, the transitions need not be first order. Specifically, we expect there to be a quantum critical point at the tip of the VBS phase as it transits to the superfluid, which was determined quite accurately earlier [139]. Therefore, to investigate whether this is in fact indicative of a quantum critical point, we calculate the Grüneisen parameter (6.14) using 7-cells numerical linked cluster expansions. If the critical contributions dominate at $\mu = \mu_c$ [129], then (6.15) holds and νz may be determined. Therefore we check if the critical scaling of Γ holds at this phase space point i.e. the tip of the VBS lobe. This phase space point was determined to be $\{\mu/V = 3.127, t/V = 0.1302\}$ for the 2/3 VBS phase [139]. At this phase space point we scale the Grüneisen parameter as (6.15) over approximately 1.2 decades using 2 Wynn cycles of extrapolation as shown in Fig. 6.15a to obtain a value $\nu z \approx 0.62$. This procedure

(a)

(b)
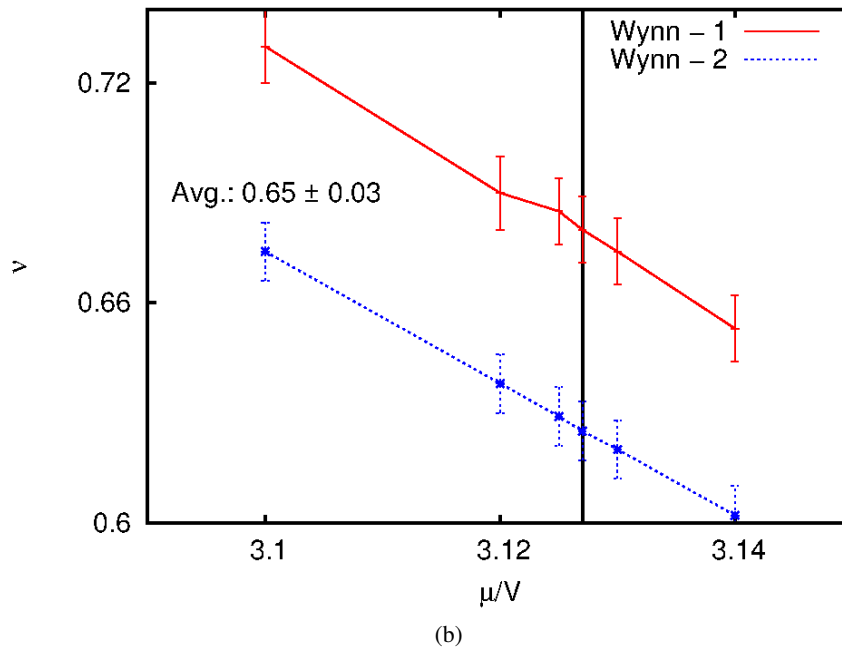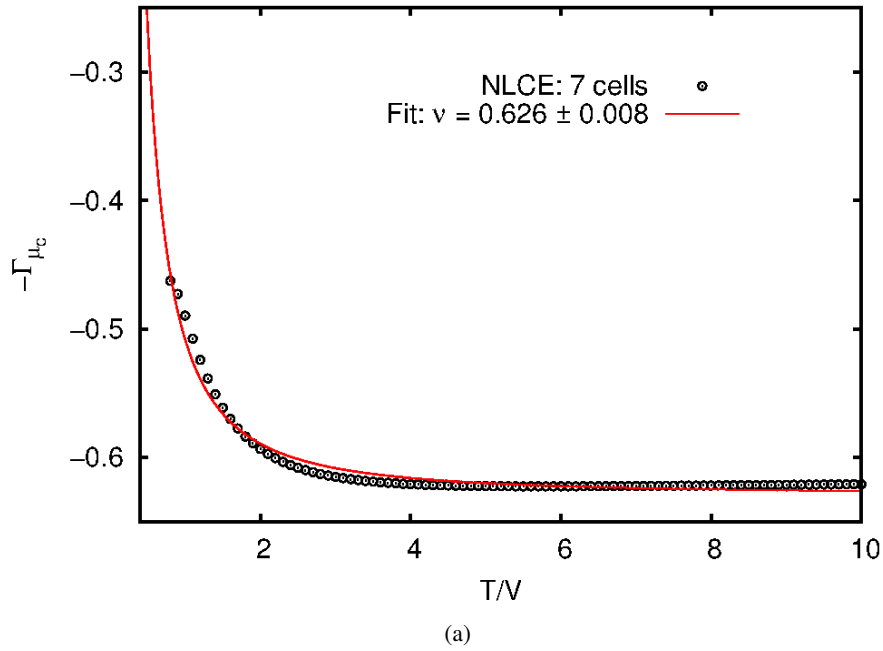
Figure 6.15: (a) Scaling of Grüneisen parameter at $t/V = 0.1302, \mu/V = 3.127$ to give the exponent $\nu z \approx 0.62$. The fit is slightly better than in the Ising case. (b) Critical exponents obtained by fitting the Grüneisen parameter, as in Fig. 6.15a, $\Gamma \propto T^{-(1\nu z)}$ close to and at the quantum critical point obtained in Ref. [139], indicated by a vertical line.

is repeated keeping $t/V = 0.1302$ fixed but varying μ/V about 3.127 (vertical line in Fig. 6.15b) to gauge the extent of scaling in phase space. The average of 1 and 2 cycles of Wynn extrapolation along

the vertical line gives $vz = 0.65 \pm 0.03$, which is to be compared with the value obtained in [139] i.e. $vz = 0.69 \pm 0.1$. Our fit is only moderately accurate, suggesting either higher orders of expansions are required to better capture the Grüneisen divergence, or that some other effect is eventually delimiting the scaling behaviour; as we shall see, we have reason to suspect the latter over the former.

The critical exponent calculated here is approximately the same value obtained at the multicritical point between the Mott lobe and superfluid for *soft-core* bosons on the square lattice [83], hard-core bosons on the star-lattice [143] (where the transition was argued to be in the XY^* universality) and XXZ model on the depleted square lattice [144]. While the various exponents do lie relatively close to one other, seeming to validate universality, there is a subtlety. The order parameter critical exponent β (not to be confused with the inverse temperature) defined by

$$m \propto |r|^\beta \tag{6.40}$$

for the order parameter m and dimensionless "distance" from the critical point r. β for the transition was calculated [139] to be $\beta = 0.26 \pm 0.07$; as an aside, for the same model and transition (VBS to superfluid) on the triangular lattice, a linked cluster expansion study found $\beta = 0.09(1)$ at zero temperature [145]. We may now evaluate the correlation exponent using the hyperscaling relation in $d = 2$ dimensions

$$2\beta = (d + z + \eta - 2)v \tag{6.41}$$

to be $\eta \approx -0.2$; $z = 1$ at the tip of the lobe due to particle-hole symmetry at this point [139]. The authors of [138] also find a negative η value close to the tip with other observables scaling as per the theory of continuous transitions; they interpret this to be a signature of weak first order transitions. We have thus provided further evidence that there is a weak first order transition at the tip of the lobe and that the latter is associated with an effective critical exponent $vz = 0.65 \pm 0.03$. Indeed a weak first order transition to the superfluid from the tip of the insulating lobe for hard-core bosons with tetrahedral interaction terms on the checkerboard lattice was earlier suggested from extensive quantum Monte Carlo studies [146].

Compressibility

The measure of compressibility K of a phase was defined in (6.4). The compressibility can serve as an indicator of how responsive the phase is to external perturbations; the analogous magnetic quantity is the spin susceptibility. For example, the incompressibility of a polarised Mott phase is indicative of the excitation gap required to create or destroy a particle; conversely a divergent compressibility indicates the appearance of a collective mode or a critical point.

The $K(\mu)$ values for $\mu/V = -1 \ldots 0$ are generally well converged for all Wynn approximants; as an illustration, consider a 14-sites expansion with 5 Wynn cycles for the strong coupling limit $V/t = 20, 50$ on the kagome lattice. The compressibility K for chemical potentials $\mu/V = -1, -0.9, \ldots, -0.2$ are shown in Fig. 6.16a. As the temperature is lowered the hopping terms are seen to induce a more compressible phase. The vanishing of the compressibilities at low temperatures for these μ values indicates the appearance of the $n_b = 0$ incompressible phase and a gap towards particle excitations. There is generally good convergence in these low density limits $n_b \lesssim 0.3$. We compute the compressibilities in the Ising limit at fixed temperatures and low densities; we notice that over a finite temperature range $T/V = 0.4 \rightarrow 0.1$, a system with $n_b \approx 0.15$ is maximally compressible compared to neighbouring densities as shown in Fig. 6.16b.

As the hopping t is switched on and for a given chemical potential, it is generally expected that when thermally induced fluctuations are weak, the system becomes more compressible because the repulsive interactions become weaker in comparison; this was seen in Fig. 6.16a. However, this need not be
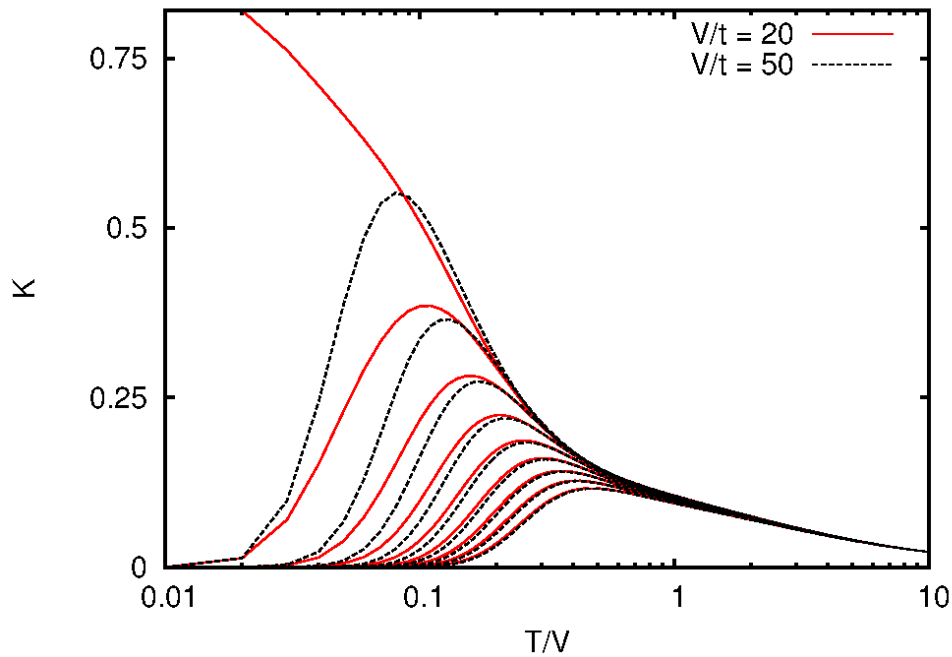
(a)
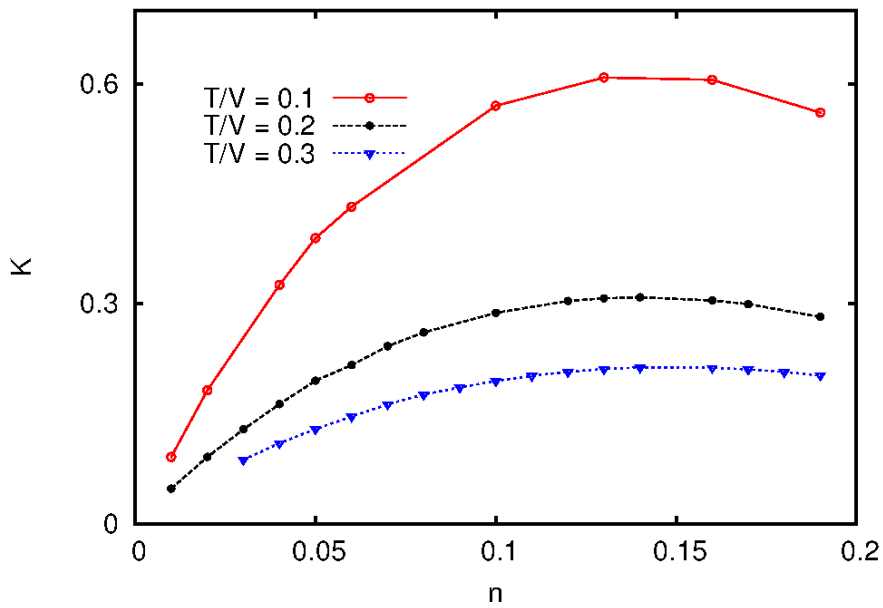
(b)

Figure 6.16: (a) Compressibility (6.4) for $V/t = 20, 50$ at $\mu/V = -1, -0.9, \ldots, -0.2$ (bottom to top) for hard-core bosons on the kagome lattice; 14-sites numerical linked cluster expansions were used. (b) Compressibility of hard-core bosons on the kagome lattice in the Ising limit as a function of particle density at fixed temperatures.

true for a given density because the density generally increases, below half-filling, as t is switched on for a given chemical potential. Indeed, this is what is seen as shown in Fig. 6.17 comparing the
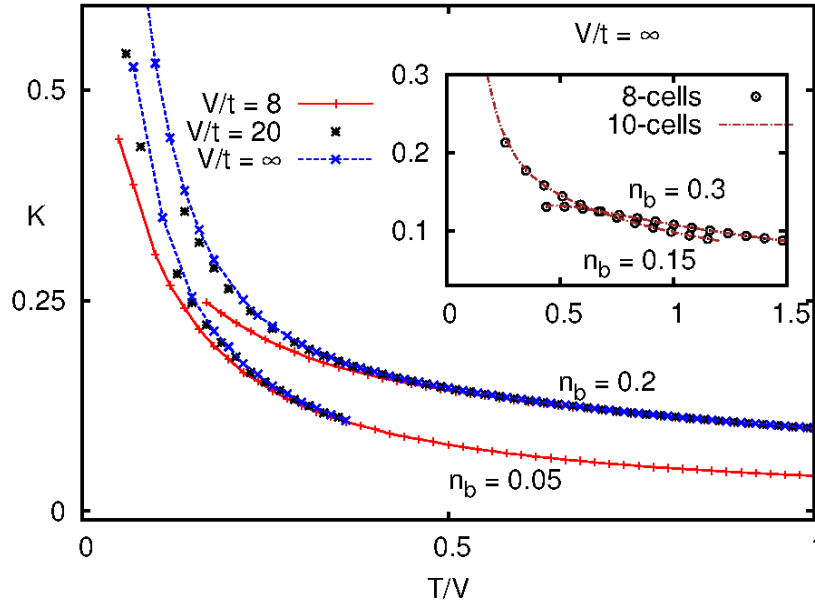
Figure 6.17: Low temperature compressibility at fixed densities n_b for $V/t = 8, 20, \infty$ for hard-core bosons on the kagome lattice. Inset shows comparisons between 8-cells and 10-cells expansions in the Ising limit.

compressibilities for $V/t = \infty, 20, 8$ (10-cells, 14-sites, and 7-cells expansions respectively) at boson densities $n_b = 0.05, 0.2$. The convergence of these quantities is verified by comparisons with other orders of expansions: 10-cells expansions are compared with 8-cells expansions in the Ising limit (inset of Fig. 6.17), and 14-sites expansions have been compared with 7-cells expansions for $V/t = 8$.

Specific heat

The calculation of specific heat proceeds via the use of formulas (6.10) and (6.12). As before, these are computed at fixed chemical potentials and inverted to constant boson densities. The functional form of the specific heat at low temperature often gives crucial information about the low energy excitations present in the material. For instance, a linear T-dependence of the specific heat is a signature of a Fermi gas or Fermi liquid state [137]; if we know a priori that interactions exist, then the former may be ruled out trivially. In the Ising limit, we use (6.10) on the 10-cells expansions (with 4 Wynn extrapolations) and (6.12) on the 8-cells expansions (with no extrapolations) for system densities $n_b = 0.05, 0.1 \cdots 0.3$; the results of these computations are shown in Fig. 6.18. We notice that at low-T and low densities (as shown in the inset), there are approximate fits to roton-like behaviour and a polynomial T-dependence. The former is given by [147]

$$C_v^{\text{roton}}\Big|_{T\to 0} \propto \exp(-|a|/T)\sqrt{T}, \tag{6.42}$$

whereas the polynomial fitting function we take to be

$$C_v^{\text{poly}}\Big|_{T\to 0} \propto bT^c, \tag{6.43}$$

for some constants a, b, c; we find that the exponent $c \approx 3 - 5$.

108
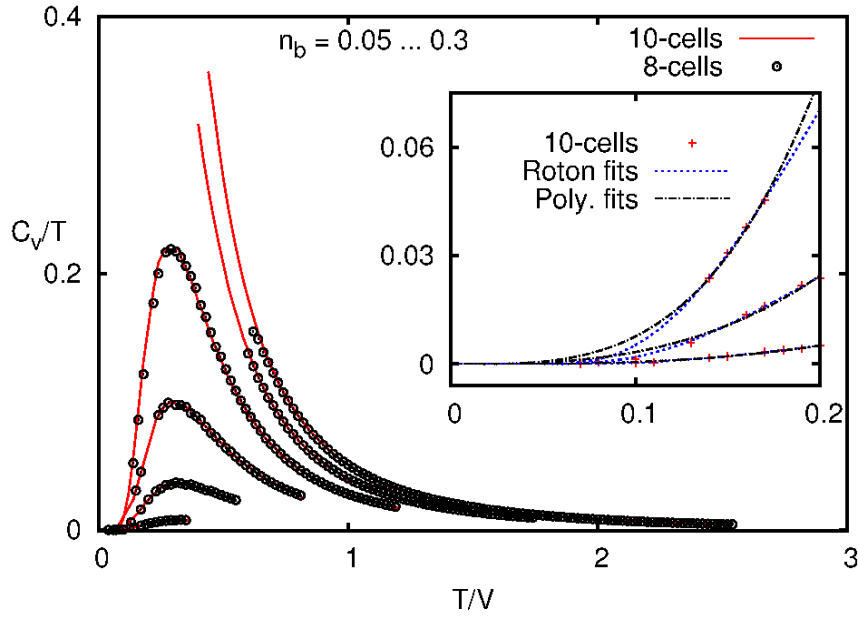
Figure 6.18: Specific heat per unit Kelvin C_v/T, at the fixed densities indicated (decreasing from top to bottom), in the Ising limit calculated using (6.10) (10-cells) and (6.12) (bare 8-cells). Inset shows the roton and polynomial fits as per (6.42), (6.43) at low densities $n_b = 0.05, 0.1, 0.15$.
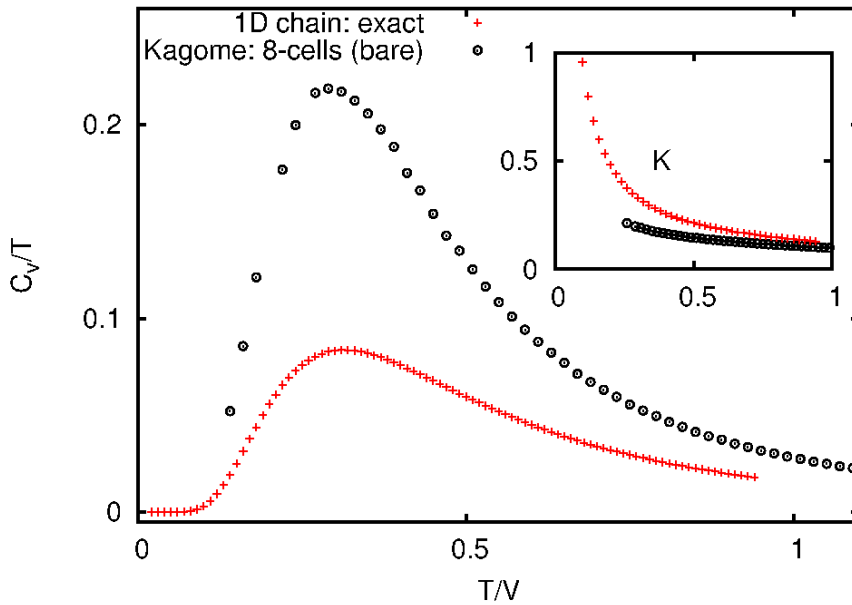
Figure 6.19: Comparison of specific heat per unit Kelvin C_v/T and compressibility K (inset) for the one dimensional chain of (exact results from (6.20)) and bare 8-cells expansions for hard-core bosons on the kagome lattice in the Ising limit at density $n_b = 0.2$.

Recall that in Fig. 6.9a we observed scaling laws for the chemical potential at these very same densities to be linear ($n_b = 0.05, 0.1$) and quadratic ($n_b = 0.15$); these do not conform to the roton-like

or polynomial behaviour observed in Fig 6.18 for the specific heat. Therefore this renders the existence of rotons as low energy excitations at these densities equivocal. That is to say, whether it is indeed (6.42) or (6.43) that scales our low-T specific heat data is not quite resolvable from our expansions at these temperatures. More work is required to clarify the nature of these low temperature excitations.

It must be noted that, surprisingly, there is a rise in the compressibility at these low-densities as seen in Fig. 6.17. In spin systems like sodium iridate, a fall in specific heat and rise in susceptibility was interpreted [148] as being the result of low energy excitations with large S_z values; these would contribute to the susceptibility but not to the specific heat. Such systems were argued [148] to be on the verge of a ferromagnetic instability. In the present case as well, we may thus suggest the reason for this seemingly anomalous behaviour as due to the system being locally surrounded (in phase space or energy landscape) by many low energy states of variable fillings; being of low energy, they contribute little to the specific heat at these temperatures. This is also seen in the one dimensional hard-core boson chain in the Ising limit which may be exactly solved via (6.20) as plotted in Fig. 6.19. As seen from the figure, the one dimensional system at these low densities is more compressible but with lesser specific heat than the kagome lattice system due to the geometry and added dimension of the latter.

Finally, away from the Ising limit, say at $V/t = 8$, we cannot make quantitative analyses for the scaling laws at low-T and low densities for the specific heat because we do not obtain convergent behaviour for the Wynn extrapolants; convergence ceases at $T/V \approx 0.2$ i.e. $T/t \approx 1.5$ for $V/t = 8$ even for low densities.

6.5 Momentum distribution

The momentum distribution was introduced in section 2.2.2 and defined in (2.27). In this section, we calculate the expectation values of the real-space correlators $\langle b_i^\dagger b_j \rangle$ using linked cluster expansions as described in the paragraph preceding (2.8) for two different systems (a) a square lattice model for high temperature superconductivity known as the $t - J$ model [15], and (b) the hard-core boson model on the one dimensional chain [16]. The former was computed earlier using high-temperature expansions at finite temperatures in Ref. [15]; the latter was computed using exact diagonalizations at zero temperature in Ref. [16]. We compare numerical linked cluster expansions at finite temperatures for the two half-filled systems and compare with their results.

For the $t - J$ model at $J/t = 0.5$, we use 6-bonds expansion for $T/t = 5, 2.5, 1$ and bare 3-cells expansions for $T/t = 0.5$ on the square lattice to compare with the eighth order high-temperature expansion results of [15]; based on which, a Fermi surface was argued [15] to develop as the temperature was lowered.. The results of the higher three temperatures are shown in the main plot of Fig. 6.20. Moreover, we stress the unique simplicity of our 3-cells expansions which uses only 5 topologically distinct graphs and no extrapolations; and yet, as seen in the inset of Fig. 6.20 for $T/t = 0.5$, the comparison is quite remarkable. The Padé extrapolation of Ref. [15] introduces error bars (only the error bars at the ends of the Brillouin zone are taken from the authors' results) at this lowest temperature and our results tend to agree within the error bars.

Further, we compute the momentum distribution of hard-core bosons on the one dimensional chain at half-filling at $V/t = 2$. This is compared to a zero temperature calculation using exact diagonalizations [16]. As seen from Fig. 6.21 computed at temperature $T/V = 0.3$ and a 12-bond expansion, there is good agreement between the finite temperature Wynn extrapolated result and the $T = 0$ result.

Based on these two results i.e. the accuracy of cell-based expansions for the momentum distribution in two dimensions, and the correspondence of finite temperature momentum distribution of hard-core bosons in the one dimensional chain to the zero temperature values, we expect to obtain reasonably
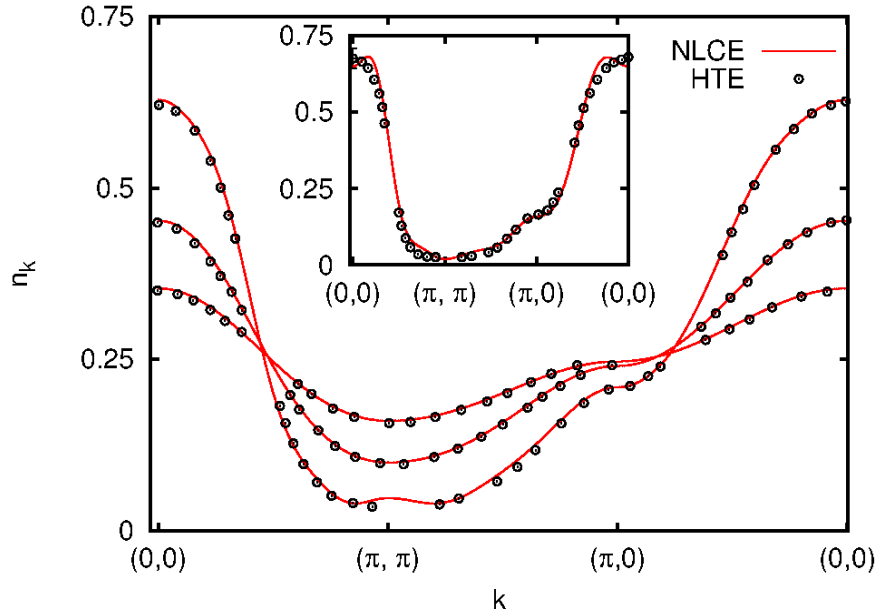
Figure 6.20: Momentum distribution computed using numerical linked cluster expansions (NLCE) in the half-filled $t - J$ model with $J/t = 0.5$ at temperatures $T/t = 5, 2.5, 1$ (main plot with 6-bonds expansion) and $T/t = 0.5$ (inset with bare 3-cells expansion), compared with high temperature expansions (HTE) of Ref. [15].
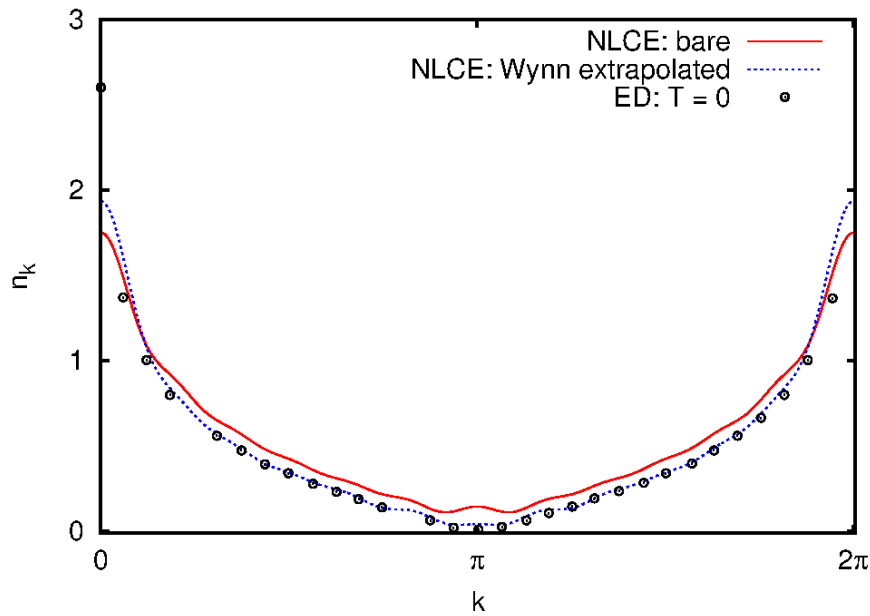

Figure 6.21: Momentum distribution in the half-filled linear chain of the hard-core boson model at finite temperature $T/V = 0.3$ computed with 12-bonds numerical linked cluster expansions (NLCE), and compared with the exact diagonalization (ED) results at zero temperature of Ref. [16].

accurate momentum distribution properties of hard-core bosons on the kagome lattice close to zero temperature using a cell-based numerical linked cluster expansion; this is scope for future work.

6.6 Conclusions

In this chapter we investigated interacting hard-core bosons modelled by (5.5) on the kagome lattice using high order numerical linked cluster expansions. We focussed on the Ising limit $V/t = \infty$ and the strong coupling limit $V/t \gg 1$. Thermodynamical and critical properties of the model at finite and low temperatures were investigated.

At finite but small temperatures away from the transition between the empty lattice and 1/3 filled phase, we found the zero-point entropy setting in at a temperature scale of $T/V = 0.2$. At the tip of the 2/3-filled valence bond solid lobe where $t/V \approx 0.1302$, we determined the effective quantum critical exponent to be $\nu z = 0.65 \pm 0.03$ based on scaling of the Grüneisen parameter in the critical regime of the system. A negative critical exponent thereby obtained from hyperscaling relations, $\eta \approx -0.2$, suggests a weak underlying first order transition between the superfluid and valence bond solid phase even at the tip of the lobe. Indeed it would be interesting to complement our study with an optical lattice realization of the model through ultra-cold gases, and determine the experimental characteristics of the transition between the valence bond solid and superfluid.

Scaling laws for chemical potential and specific heat were determined in the Ising limit and strong coupling limit at low temperatures. At $n_b = 0.15$ in the Ising limit, a quadratic dependence on the temperature for the chemical potential was observed, reminiscent of Fermi-liquid behaviour. However, by obtaining two approximate low-T scaling forms (roton-like and polynomial) for the specific heat at similar low densities, we are left inconclusive as to the actual scaling function. Clarifying the nature of the low temperature excitations at these densities constitutes prospect for future theoretical and experimental work.

We further compared the compressibilities of the system at constant densities for varying V/t values. As in the one dimensional chain of hard-core bosons in the Ising limit, we found evidence for a state with suppressed specific heat but rising compressibility at finite temperature. This suggests the ease of adding a particle to the system but that the adjacent (in phase space or energy landscape) states are of very low energy, thereby contributing little to the specific heat.

Finally, we investigated the momentum distribution of hard-core bosons at varying V/t on the one dimensional chain and found that even at finite temperatures, there is good comparison with zero temperature results from exact diagonalization studies. Computation of the momentum distribution of hard-core bosons on the kagome lattice will provide a better understanding of the underlying physics and phases in the model.

Acknowledgements

Summary

In this thesis we have investigated lattice models as applicable to ultra-cold atoms in optical lattices and magnetic materials, using a variety of techniques such as linked cluster expansions (perturbation theory and exact diagonalization), lattice Green's functions, spin wave analysis, transfer matrix methods, and Binder's algorithm. Where applicable, implementations of quantum Monte Carlo, Bethe ansatz, and integrable relations of the 8-vertex model were employed for purposes of comparison.

In the non-interacting limit of particles on lattices, describable by tight-binding models, the statistical properties of three related lattices were investigated: kagome, diced and hyperkagome lattices. Indeed, tight-binding model on the honeycomb lattice and its statistical properties have been quite successful in describing the physics of graphene, a material of great topical interest. We calculated the diagonal and off-diagonal lattice Green's functions for the three cases, and their corresponding density of states. For particles on the hyperkagome lattice, we found that its density of states is expressible in a functional form that closely resembles other exactly solvable lattices with a simple cubic unit cell. However, the presence of extra terms in the relevant integral appears to destroy integrability for the hyperkagome; for future work, it would be interesting to check if this density of states may in fact be expressed in closed form. Such a form could benefit dynamical mean field theory calculations and our understanding of the role of introducing interactions to the non-interacting limit on the hyperkagome lattice, where the metal-insulator transition is a present day topic of research.

In the opposite limit of immobile particles, we considered the Ising spin models on quasi-one dimensional ladders and the kagome lattice. Specifically, at special longitudinal field values before spin ordering sets in, we enumerate all spin configurations allowed in the absence of thermal fluctuations and demonstrate their contribution to a residual entropy in the system. Ising spins at saturation on the kagome lattice describes the physics of the decoupled planes of the spin ice compound $Dy_2Ti_2O_4$ at saturation. We compute the residual entropy at this transition point using transfer matrix methods and Binder's algorithm, the latter procedure enabling us to exactly evaluate the partition function of over 1300 spins. The value is compared to experimental entropy measurements of $Dy_2Ti_2O_4$ at low temperature and there is good agreement. Our procedure for constructing higher dimensional lattices from lower dimensional ones may be used in conjunction with Binder's algorithm to accurately compute the partition function of physical models on complex lattice geometries.

For mobile and interacting particles in the strongly coupled limit, we investigated the zero temperature physics of the soft-core Bose-Hubbard model on the one dimensional chain lattice and the two dimensional square lattice with three and four body local interactions. Using linked cluster expansions and

Thiele's algorithm, we formulated a novel scheme to exactly renormalize, at every perturbative order, the strong two body interactions due to the presence of the three and four body interactions. We suggested that all higher body local interactions may be re-summed in this manner for both single particle excited properties and ground state properties. Indeed, such a scheme may even be used, akin to the Padé extrapolation, to approximately renormalize critical and thermodynamical properties from the effect of a second perturbation variable for any physical system analysable through series expansion techniques, such as spin systems or perturbative quantum chromodynamics. The universality of the transition from the Mott insulator to the superfluid at the multicritical point is checked for both the one dimensional chain lattice (a Berezinskii-Kosterlitz-Thouless transition) and the two dimensional square lattice; the coherence length critical exponent of the latter was compared with that of the three dimensional *XY* model. Moreover, our re-summed formulas readily show the onset of perturbative instabilities for the first Mott lobe at certain attractive three body interactions. All these results will aid experimentalists in better understanding the physics and dynamics of higher body interactions in ultra-cold atoms, where the strength of such interactions may be manipulated in a controlled manner.

Further, we studied the properties of the phases and transitions in the hard-core Bose-Hubbard model with nearest neighbour interactions on *d*-dimensional (focussing on $d \geq 2$) hypercubic lattices and the kagome lattice. For the former, we formulated a collinear spin wave theory for arbitrary interactions and demonstrated the influence of spin wave excitations, atop the mean field solutions, on system properties such as partition function, particle density, and energy density. We simulated the model on the two dimensional square lattice and the three dimensional simple cubic lattice using an implementation of quantum Monte Carlo, and we found good agreement with the results of spin wave theory provided the checkerboard solid is not in the vicinity in phase space. By comparing the ground state phase diagram using Bethe ansatz in one dimension, quantum Monte Carlo in two dimensions, and spin wave theory in $d \geq 2$ dimensions, we provided a helpful pictorial gauge for the effect of quantum fluctuations as the dimensionality is changed. It would be interesting to investigate whether even the strongly coupled limit may be accurately handled using spin wave theory if interactions between spin waves are taken into account.

On the kagome lattice, we explored the physics of the nearest neighbour interacting hard-core Bose-Hubbard model using numerical linked cluster expansions (exact diagonalizations with linked cluster expansions). The study was performed with high orders of expansions at finite temperatures *T*, and the results were controllably extrapolated using Wynn's algorithm to low temperatures. We computed various thermodynamic quantities in the system such as particle density, energy, entropy, compressibility, specific heat and Grüneisen parameter in the immobile or Ising limit and the strong coupling limits. In the Ising limit, we provided evidence for the first order nature of the transition between the empty lattice and the 1/3 filled phase based on the low temperature behaviour of internal energy. In the Ising limit at low and fixed densities, we discovered linear and quadratic scaling laws of the chemical potential as a function of temperature, the latter being reminiscent of Fermi liquid behaviour; however, low temperature scaling behaviour of the specific heat at these densities fits approximately to a polynomial *T*-dependence as well as to roton-like contributions. Taken together, the nature of these low-lying excitations remains unclear and poses scope for future theoretical and experimental work.

Finally, in the strong coupling limit, we provided evidence, based on Grüneisen parameter scaling at finite temperatures, that the transition at the tip of the valence bond solid lobe to the superfluid at zero temperature has characteristics of a weak first order transition; the effective quantum critical exponent we compute, $\nu z \approx 0.65$, is compared favourably with earlier quantum Monte Carlo simulations. Our results and analyses of the model will be relevant for and complemented by experiments in ultra-cold bosonic gases with hard-core interactions on optical kagome lattices.

Bose condensate and superfluidity

In the table below we list out the conceptual differences between a Bose-Einstein condensate and the phenomenon of superfluidity alluded to in chapter 5. Representative references include [149–152].

Table A.1: Some major conceptual differences between a Bose-Einstein condensate and the phenomenon of superfluidity.

Criterion	Bose-Einstein condensate	Superfluidity
Characteristic	Occupation of single state	Hydrodynamic property: dissipationless flow
Example	Free bosons: BEC without superfluidity	He-4: superfluidity driven by BEC ($\approx 10\%$)
Periodic 1D/2D systems	No BEC at finite temperature	Superfluidity possible
Measurement in cold atoms	Expansion imaging	Optically induce $\vec{\mathbf{A}}$ field
Spin waves	Deplete condensate	Increase superfluid fraction
Vortices	Do not exist	Exist above certain rotational velocity
Existence	No proof with interactions	Can exist for interacting systems
Measurement ease	In cold atoms	In liquid He II
Off diagonal long range order	Yes	Only if coexists with BEC

Note that only massive, non-interacting bosons cannot condense in one or two dimensional periodic and ideal geometries; massless bosons may indeed condense in two dimensional systems. Moreover present day experiments using ultra-cold atoms are usually cut off by harmonic traps, thus excluding the validity of the above no-go theorem in point 3.

Embeddings on lattices

Here we illustrate the calculation of lattice constants in Fig. 2.4 for the 3-bond linear graph on the square lattice in a bond and site expansion, the kagome lattice in a site expansion, and the 2-bond linear graph on the triangular lattice in a site expansion. Note that for the kagome lattice, because there are three sites per unit cell, we need to keep track of the which of the three sites we choose as origin; this is labelled as *A* in Fig. B.3.
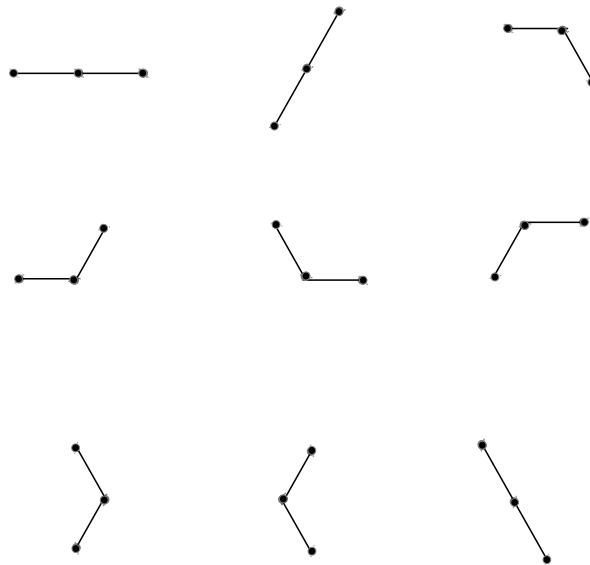
Figure B.1: Site embeddings of the 2-bond graph on the triangular lattice, giving a lattice constant of 9.
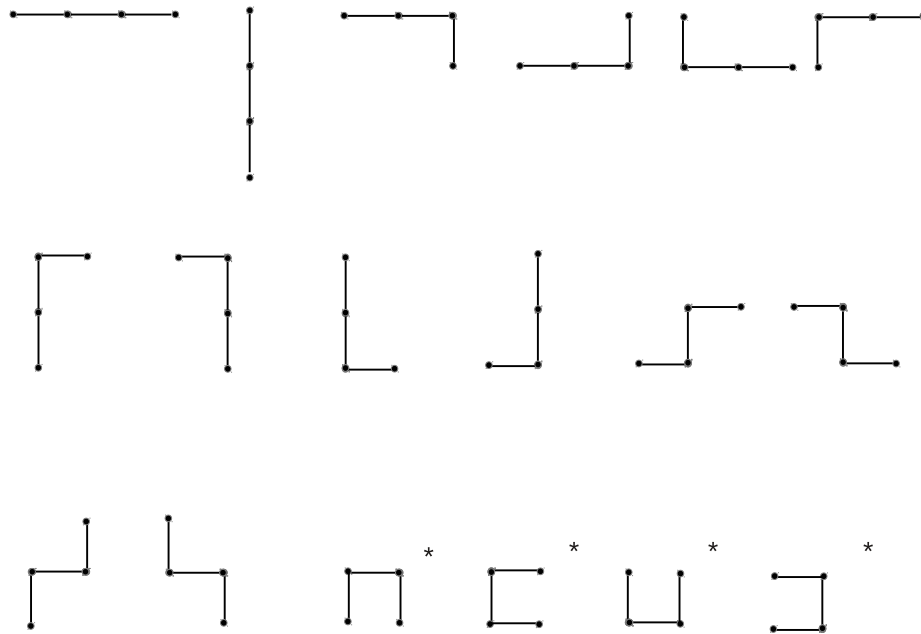
Figure B.2: Bond embeddings of the 3-bond graph on the square lattice, with starred embeddings being disallowed in a site expansion. The lattice constants for the bond and site expansions for this graph are therefore 18 and 14 respectively.
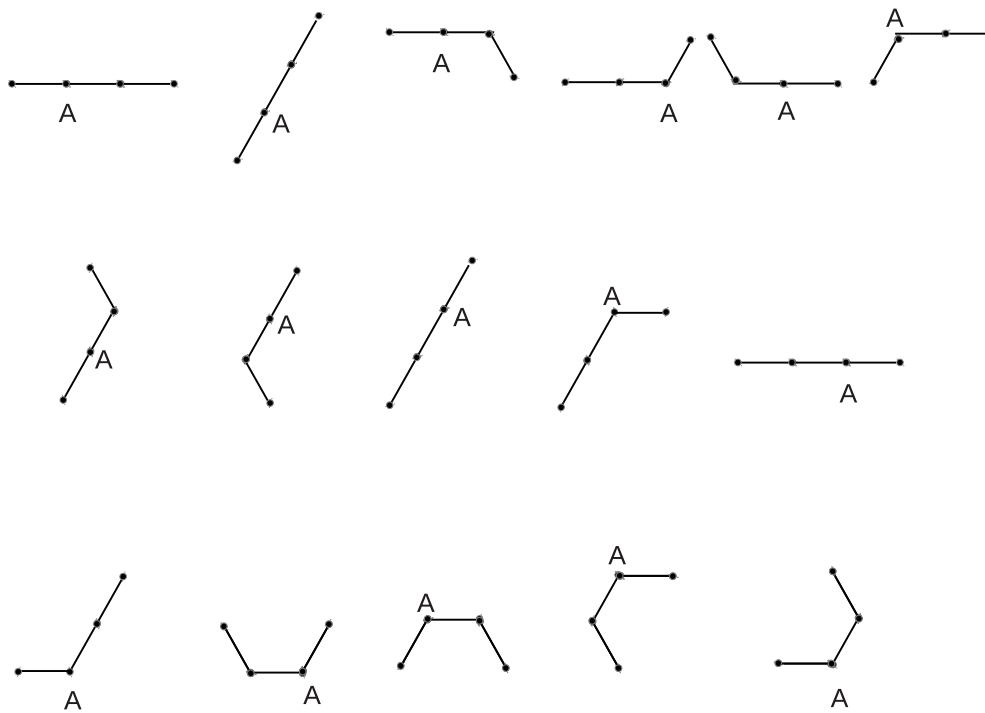
Figure B.3: Site embeddings of the 3-bond graph on the kagome lattice with respect to the *A* sublattice. The lattice constant is calculated by dividing the number of embeddings by the automorphism order of the graph as in (2.7) i.e. $L = 16/2 = 8$.

Brezinski's bordering methods

Here we outline the formulas required for implementing Brezinski's bordering methods [27] that compute the Wynn extrapolants [26]. The auxiliary quantities λ_k, d_k, σ_k that were introduced in section 2.4.3 will be precisely defined here. Additional quantities that do not directly occur in the bordering relations of (2.48) will also be introduced.

First bordering method

Initialization of the method for fixed n begins with

$$
\begin{aligned}
\gamma_{-1} = d_{-2} = 0, \qquad & \lambda_{-1} = d_{-1} = 1 \\
\lambda_0 = s_n \\
u_i^{(-2)} = 0 \qquad & \forall i, \qquad u_0^{(-1)} = 1 \\
u_0^{(-1)} = 0 \qquad & i \neq 0 \\
u_q^{(p)} = 0 \qquad & q > p + 1 \quad \text{and} \quad \forall q < 0 \\
u_{p+1}^{(p)} = 1 \qquad & p \geq 0 \\
s_0^{(n)} = s_n.
\end{aligned}
\tag{C.1}
$$

Then for the same fixed $n, k \geq 0$, the auxiliary variables are given by

$$
\begin{aligned}
\gamma_k &= \sum_{i=0}^{k} s_{n+k+i+1} u_i^{k-1} \\
u_i^{(k)} &= \left(\frac{\gamma_{k-1}}{\lambda_{k-1}} - \frac{\gamma_k}{\lambda_k} \right) u_i^{(k-1)} + u_{i-1}^{(k-1)} - \frac{\lambda_k}{\lambda_{k-1}} u_i^{(k-2)} \qquad i = 0, \dots, k \\
u_{k+1}^{(k)} &= 1 \\
d_k &= \left(\frac{\gamma_{k-1}}{\lambda_{k-1}} - \frac{\gamma_k}{\lambda_k} + 1 \right) d_{k-1} - \frac{\lambda_k}{\lambda_{k-1}} d_{k-2} \\
\lambda_{k+1} &= \sum_{i=0}^{k+1} s_{n+k+i+1} u_i^{(k)}.
\end{aligned}
\tag{C.2}
$$

Then the recursion relation for the even-subscripted Wynn extrapolated values is given as in (2.48)

$$\frac{1}{s_{2k+2}^{(n)}} = \frac{1}{s_{2k}^{(n)}} + \frac{d_k^2}{\lambda_{k+1}}.$$

(C.3)

Second bordering method

Initialization of the method begins with

$$
\begin{aligned}
d_{-1} &= \gamma_0 = 0, \\
d_0 &= \lambda_0 = 1, \\
b_i^{(-1)} &= 0 && \forall i, \\
b_0^{(0)} &= 1 && b_i^{(0)} = 0 && \forall i \neq 0, \\
b_i^{(p)} &= 0 && \forall i < 0 && \text{and} && \forall i > p, \\
b_0^{(p)} &= 1 && \forall p \geq 0.
\end{aligned}
$$

(C.4)

For a given $n \geq 0$ and $k = 1, 2, \ldots$, the auxiliary quantities in C.4 are given by

$$\lambda_k = \sum_{i=0}^{k-1} (s_{n+k+i} - s_{n+k+i-1}) b_{k-i-1}^{(k-1)}$$

$$\gamma_k = \sum_{i=0}^{k-1} (s_{n+k+i+1} - s_{n+k+i}) b_{k-i-1}^{(k-1)}$$

$$b_i^{(k)} = \left(\frac{\gamma_{k-1}}{\lambda_{k-1}} - \frac{\gamma_k}{\lambda_k} \right) b_{i-1}^{(k-1)} + b_i^{(k-1)} - \frac{\lambda_k}{\lambda_{k-1}} b_{i-2}^{(k-2)} \qquad i = 1, \ldots, k$$

$$b_0^{(k)} = 1$$

$$d_k = \left(\frac{\gamma_{k-1}}{\lambda_{k-1}} - \frac{\gamma_k}{\lambda_k} + 1 \right) d_{k-1} - \frac{\lambda_k}{\lambda_{k-1}} d_{k-2}$$

$$\sigma_k = \sum_{i=0}^{k} b_i^{(k)} s_{n+k-i}.$$

(C.5)

Then the even subscripted Wynn extrapolated values are given as in (2.48)

$$s_{2k}^{(n)} = \frac{\sigma_k}{d_k}.$$

(C.6)

Re-summed coefficients with 4-body interactions

Table D.1: Coefficients for perturbative expansion of ground state energy in $\lambda = t/U$ for 8th and 10th orders in the Bose-Hubbard chain for various 4 body interaction strengths. Lower order coefficients are independent of r_4.

r_4	c_8	c_{10}
0	$-\dfrac{5068}{81}$	$\dfrac{88342}{729}$
$\dfrac{1}{10}$	$-\dfrac{303740}{4941}$	$\dfrac{17722027582}{165469149}$
$\dfrac{1}{5}$	$-\dfrac{151700}{2511}$	$\dfrac{2030541082}{21717639}$
$\dfrac{1}{4}$	$-\dfrac{121291}{2025}$	$\dfrac{989461654}{11390625}$
$\dfrac{1}{3}$	$-\dfrac{90884}{1539}$	$\dfrac{380308642}{5000211}$
$\dfrac{1}{2}$	$-\dfrac{4652}{81}$	$\dfrac{524206}{9477}$
1	$-\dfrac{30068}{567}$	$\dfrac{183062}{250047}$
2	$-\dfrac{3716}{81}$	$-\dfrac{265283}{2916}$
3	$-\dfrac{9796}{243}$	$-\dfrac{3157886}{19683}$
4	$-\dfrac{14524}{405}$	$-\dfrac{19641058}{91125}$
5	$-\dfrac{28708}{891}$	$-\dfrac{252578158}{970299}$
6	$-\dfrac{788}{27}$	$-\dfrac{72268}{243}$
10	$-\dfrac{1688}{81}$	$-\dfrac{9292771}{23328}$

Bibliography

[1]   L. P. Gor'kov,
      "Microscopic derivation of the Ginzburg-Landau equations in the theory of superconductivity",
      Sov. Phys., JETP 36(9) (1959) 1364.

[2]   P. W. Anderson, *More and Different: notes from a thoughtful curmudgeon*,
      Singapore: World Scientific, 2011.

[3]   R. Roy, "Discovery of the series formula for π by Leibniz, Gregory and Nilakantha",
      Math. Mag. 63 (1990) 291.

[4]   P. Beckmann, *A History of π*, Boulder: Golem Press, 1982.

[5]   C. Domb and M. S. Green, *Phase Transitions and Critical Phenomena Vol 3*,
      Academic Press, 1974.

[6]   M. P. Gelfand and R. R. P. Singh,
      "High-order convergent expansions for quantum many particle systems",
      Adv. in Phys. 49 (2000) 93.

[7]   V. K. Varma, "Quasiparticle dynamics on frustrated lattices",
      Master of Physics thesis, University of Bonn, MA thesis, 2010.

[8]   J. Oitmaa, C. Hamer and W. Zheng,
      Series Expansion Methods for Strongly Interacting Lattice Models, 1st ed.,
      Cambridge: Cambridge University Press, 2006.

[9]   M. Rigol, T. Bryant and R. R. P. Singh, "Numerical linked-cluster algorithms. I. Spin systems
      on square, triangular, and kagomé lattices", *Phys. Rev. E* 75 (2007) 061118.

[10] D. Eppstein, *Live Journal*, `http://www.ics.uci.edu/~eppstein/`, (visited on 10–2011).

[11] B. D. McKay, "*nauty* User's guide" (2004).

[12] J. H. Siek, L. Lee and A. Lumsdaine, *The Boost Graph Library*,
      Upper Saddle River, New Jersey: Addison-Wesley, 2001.

[13] G. Baym, *Lectures on Quantum Mechanics*, Lecture Notes and Supplements in Physics,
      England: Benjamin/Cummings, 1969.

[14] M. P. Gelfand, "Series expansions for excited states of quantum lattice models",
      Solid State Comm. 98 (1996) 11.

[15] R. R. P. Singh and R. L. Glenister,
      "Momentum Distribution function for the two-dimensional t-J model",
      Phys. Rev. B 46 (1992) 14313(R).

[16] M.-C. Cha, J.-G. Shin and J.-W. Lee,
"Momentum distribution of the hard-core extended boson Hubbard model in one dimension",
Phys. Rev. B 80 (2009) 193104.

[17] E. Anderson, Z. Bai, C. Bischof, S. Blackford, J. Demmel, J. Dongarra, J. Du Croz,
A. Greenbaum, S. Hammarling, A. McKenney and D. Sorensen, *LAPACK Users' Guide*,
Third Edition, Philadelphia, PA: Society for Industrial and Applied Mathematics, 1999.

[18] A. Kloeckner, *Boost numeric bindings*,
`http://mathema.tician.de/dl/software/boost-numeric-bindings/`,
(visited on 06–2011).

[19] L. N. Trefethen and D. Bau III, *Numerical Linear Algebra*,
Philadelphia: Society for Industrial and Applied Mathematics, 1997.

[20] G. A. Baker Jr., J. L. Gammel and J. G. Wills,
"An investigation of the applicability of the Padé approximant method",
J. Math. Anal. and Appl. 2 (1961) 405.

[21] G. A. Baker Jr., "Application of the Padé Approximant Method to the Investigation of Some
Magnetic Properties of the Ising Model", *Phys. Rev.* 124 (1961) 768.

[22] G. A. Baker Jr. and P. Graves-Morris, *Padé Approximants: Part I*,
Encyclopedia of Mathematics and its applications, Addison-Wesley Publishing, 1981.

[23] I. Wolfram Research, "Mathematica Edition: Version", *Champaign, Illinois* (2011).

[24] J. Stoer and R. Bulirsch, *Introduction to Numerical Analysis*, 3rd ed.,
Texts in Applied Mathematics, Springer, 2002.

[25] F. Bornemann, D. Laurie, S. Wagon and J. Waldvogel, *The SIAM 100-Digit Challenge*,
Society for Industrial and Applied Mathematics, 2004.

[26] P. Wynn, "On a device for computing $e_m(s_n)$ transformation", *MTAC* 10 (1956) 91.

[27] C. Brezinski, "Computation of Padé approximants and continued fractions",
Journal of Comp. and Appl. Mathematics 2 (1976) 113.

[28] J. W. Negele and H. Orland, *Quantum Many-Particle systems*,
Redwood city, California: Addison-Wesley, 1979.

[29] A. H. Castro Neto, F. Guinea, N. M. R. Peres, K. S. Novoselov and A. K. Geim,
"The electronic properties of graphene", *Rev. Mod. Phys.* 81 (1 2009) 109–162.

[30] R. Saito, G. Dresselhaus and M. S. Dresselhaus, *Physical Properties of Carbon Nanotubes*,
London: Imperial College Press, 1999.

[31] H.-M. Guo and M. Franz, "Topological insulator on the kagome lattice",
Phys. Rev. B 80 (11 2009) 113102.

[32] E. N. Economou, *Green's functions in Quantum Physics*,
Berlin: Springer series in Solid-state physics, 1979.

[33] I. S. Gradshteyn, I. M. Ryzhik and A. Jeffrey, *Tables of Integrals, Series and Products*,
Fifth edition, San Diego: Academic Press, Inc., 2007.

[34] S. Katsura, T. Morita, S. Inawashiro, T. Horiguchi and Y. Abe,
"Lattice Green's Function. Introduction", *J. Math. Phys.* 12 (5) (1971) 892.

[35] A. J. Guttmann and T. Prellberg,
"Staircase polygons, elliptic integrals, Heun functions, and lattice Green functions",
Phys. Rev. E 47 (1993) R2233.

[36] R. M. Ziff, "Flux to a trap", *Journal of Statistical Physics* 65 (1991) 1217.

[37] T. Horiguchi and C. C. Chen, "Lattice Green's Function for the diced lattice",
J. Math. Phys. 15 (5) (1974) 659.

[38] T. Horiguchi, "Lattice Green's functions for the triangular and Honeycomb lattices",
J. Math. Phys. 13 (9) (1972) 1411.

[39] T. Hanisch, G. S. Uhrig and E. Müller-Hartmann,
"Lattice dependence of saturated ferromagnetism in the Hubbard model",
Phys. Rev. B 56 (21) (1997) 13960.

[40] H. Lee and H. Monien, "Mott transition in the Hubbard model on the hyper-kagome lattice",
arXiv:0903.3005[cond-mat.str-el](unpublished), Mar. 2009.

[41] M. Udagawa and Y. Motome, "Cluster dynamical mean-field study of the Hubbard model on a 3D frustrated hyperkagome lattice", *J. Phys.: Cond. Series* 145 (2009) 012013.

[42] M. L. Glasser and I. J. Zucker, "Extended Watson integrals for the cubic lattices",
Proc. Natl. Acad. Sci. USA 74(5) (1977) 1800.

[43] M. L. Glasser, "Closed form expressions for a class of lattice Green's functions",
J. Phys.: Conf. Ser. 42 (2006) 95.

[44] M. L. Glasser, "Definite Integrals of the Complete Elliptic Integral",
J. Res. NBSB. Mathematical Sciences 80B (2006) 313.

[45] M. Z. Hasan and C. L. Kane, "*Colloquium* : Topological insulators",
Rev. Mod. Phys. 82 (4 2010) 3045.

[46] E. Ising, "Beitrag zur Theorie des Ferromagnetismus",
Zeitschrift fuer Physik A: Hadrons and Nuclei 31 (1925) 253.

[47] P. J. Puddephatt, *The periodic table of the elements*, Oxford: Clarendon Press, 1972.

[48] G. A. Prinz, "Optical Absorption Spectra of Coupled Nd^{3+} Ions in $NdCl_3$ and $NdBr_3$",
Phys. Rev. 152 (1 1966) 474.

[49] J. C. Wright, H. W. Moos, J. H. Colwell, B. W. Mangum and D. D. Thornton,
"$DyPO_4$: A Three-Dimensional Ising Antiferromagnet", *Phys. Rev. B* 3 (3 1971) 843.

[50] J. C Bonner and M. E Fisher, "The Entropy of an Antiferromagnet in a Magnetic Field",
Proc. Phys. Soc. 80 (1962) 2304.

[51] R. Moessner, S. L. Sondhi and P. Chandra,
"Two-Dimensional Periodic Frustrated Ising Models in a Transverse Field",
Phys. Rev. Lett. 84 (19 2000) 4457.

[52] K. Kano and S. Naya, "Antiferromagnetism: The Kagomé Ising Net",
Prog. of Theo. Phys. 10 (1953) 158.

[53] P. Sen, "Quantum phase transitions in the Ising model in a spatially modulated field",
Phys. Rev. E 63 (1 2000) 016112.

[54] A. A. Ovchinnikov, D. V. Dmitriev, V. Y. Krivnov and V. O. Cheranovskii,
      "Antiferromagnetic Ising chain in a mixed transverse and longitudinal magnetic field",
      Phys. Rev. B 68 (21 2003) 214406.

[55] P. G. de Gennes, "Collective motions of hydrogen bonds",
      Solid State Communications 1.6 (1963) 132.

[56] S. V. Isakov, K. S. Raman, R. Moessner and S. L. Sondhi,
      "Magnetization curve of spin ice in a [111] field", *Phys. Rev. B* 70 (2004) 104418.

[57] Z. Hiroi, K. Matsuhira, S. Takagi, T. Tayama and T. Sakakibara,
      "Specific Heat of Kagomé Ice in the Pyrochlore Oxide $Dy_2Ti_2O_7$",
      J. Phys. Soc. Jpn. 72.2 (2003) 411.

[58] G. H. Wannier, "Antiferromagnetism: The Triangular Ising Net", *Phys. Rev.* 79 (1950) 357.

[59] P. W. Anderson, "Ordering and Antiferromagnetism in Ferrites", *Phys. Rev.* 102 (1956) 1008.

[60] R. Liebmann, *Statistical Mechanics of Periodic Frustrated Ising Systems*,
      Berlin Heidelberg New York Tokyo: Springer-Verlag, 1986.

[61] M. Udagawa, M. Ogata and Z. Hiroi, "Exact Result of Ground-State Entropy for Ising
      Pyrochlore Magnets under a Magnetic Field along [111] Axis",
      J. Phys. Soc. Jpn. 71 (2002) 2365.

[62] R. Moessner and S. L. Sondhi, "Theory of the [111] magnetization plateau in spin ice",
      Phys. Rev. B 68 (2003) 064411.

[63] C. Domb, "On the theory of cooperative phenomena in crystals",
      Advances in Physics 9.34 (1960) 149.

[64] B. D. Metcalf and C. P. Yang, "Degeneracy of antiferromagnetic Ising lattices at critical
      magnetic field and zero temperature", *Phys. Rev. B* 18 (5 1978) 2304.

[65] J. Schulenburg, A. Honecker, J. Schnack, J. Richter and H.-J. Schmidt, "Macroscopic
      Magnetization Jumps due to Independent Magnons in Frustrated Quantum Spin Lattices",
      Phys. Rev. Lett. 88 (16 2002) 167207.

[66] O. Derzhko and J. Richter, "Finite low-temperature entropy of some strongly frustrated
      quantum spin lattices in the vicinity of the saturation field", *Phys. Rev. B* 70 (10 2004) 104415.

[67] J. F. Nagle, "New Series-Expansion Method for the Dimer Problem",
      Phys. Rev. 152 (1 1966) 190.

[68] A. R Gordon, "The Calculation of Thermodynamic Quantities from Spectroscopic Data for
      Polyatomic Molecules; the Free Energy, Entropy and Heat Capacity of Steam",
      J. Chem. Phys. 2.7 (1934) 65.

[69] P. W Atkins, *Physical Chemistry*, Oxford: Oxford University Press, 1986.

[70] W. F. Giauque and J. W. Stout, "The Entropy of Water and the Third Law of Thermodynamics.
      The Heat Capacity of Ice from 15 to 273 K.",
      Journal of the American Chemical Society 58.7 (1936) 1144.

[71] L. Pauling, "The Structure and Entropy of Ice and of Other Crystals with Some Randomness of
      Atomic Arrangement", *Journal of the American Chemical Society* 57.12 (1935) 2680.

[72] R. J. Baxter, "Hard hexagons: exact solution", *J. Phys. A* 13 (1980) L61.

[73] S. Milošević, B. Stošić and T. Stošić,
"Towards finding exact residual entropies of Ising antiferromagnets",
Physica A 157 (1989) 899.

[74] W. Keller-Gehrig, "Fast algorithms for the characteristic polynomial",
Theoretical Computer Science 36 (1985) 309.

[75] K. Binder, "Statistical mechanics of finite three-dimensional Ising models",
Physica 62 (1972) 508.

[76] D. Jaksch, C. Bruder, J. I. Cirac, C. W. Gardiner and P. Zoller,
"Cold bosonic atoms in optical lattices", *Phys. Rev. Lett.* 81 (1998) 3108.

[77] M. Greiner, O. Mandel, T. Esslinger, T. W. Haensch and I. Bloch,
"Quantum phase transition from a superfluid to a Mott insulator in a gas of ultracold atoms",
Nature 415 (2002) 39.

[78] M. P. A. Fisher, P. B. Weichman, G. Grinstein and D. S. Fisher,
"Boson localization and the superfluid-insulator transition", *Phys. Rev. B* 40 (1989) 546.

[79] V. Berezinskii, "Destruction of long-range order in one-dimensional and two-dimensional
systems having a continuous symmetry group II. Quantum systems",
Sov. Phys., JETP 34 (1971) 610.

[80] J. M. Kosterlitz and D. J. Thouless,
"Ordering, metastability and phase transitions in two-dimensional systems",
Journal of Physics C: Solid State Physics 6.7 (1973) 1181.

[81] C. Itzykson and J.-M. Drouffe, *Statistical Field Theory*,
Cambridge: Cambridge University Press, 1989.

[82] T. D. Kuehner and H. Monien, "Phases of the one-dimensional Bose-Hubbard model",
Phys. Rev. B 58 (1998) R14741.

[83] N. Elstner and H. Monien, "Dynamics and thermodynamics of the Bose-Hubbard model",
Phys. Rev. B 59 (1999) 12184.

[84] J. K. Freericks and H. Monien,
"Strong-coupling expansions for the pure and disordered Bose-Hubbard model",
Phys. Rev. B 53 (1996) 2691.

[85] P. B. Weichman, "Crossover scaling in a dilute bose superfluid near zero temperature",
Phys. Rev. B 38 (1988) 8739.

[86] S. Sachdev, *Quantum Phase Transitions*, Cambridge: Cambridge University Press, 1999.

[87] Z. Hadzibabic, P. Kruger, M. Cheneau, B. Battelier and J. Dalibard,
"Berezinskii-Kosterlitz-Thouless crossover in a trapped atomic gas",
Nature 441 (2006) 1118–1121.

[88] M. Endres, T. Fukuhara, D. Pekker, M. Cheneau, P. Schauss, C. Gross, E. Demler, S. Kuhr and
I. Bloch,
"The Higgs amplitude mode at the two-dimensional superfluid/Mott insulator transition",
Nature 487 (2013) 454.

[89] R. D. Murphy and J. A. Baker, "Three-Body Interactions in Liquid and Solid Helium",
Phys. Rev. A 3 (1971) 1037.

[90] H. P. Buechler, A. Micheli and P. Zoller, "Three-body interactions with cold polar molecules",
Nat. Phys. 3 (2007) 726.

[91] J. M. Sage, S. Sainis, T. Bergeman and D. DeMille,
"Optical Production of Ultracold Polar Molecules", *Phys. Rev. Lett.* 94 (20 2005) 203001.

[92] B.-l. Chen, X.-b. Huang, S.-p. Kou and Y. Zhang,
"Mott-Hubbard transition of bosons in optical lattices with three-body interactions",
Phys. Rev. A 78 (2008) 043603.

[93] P. R. Johnson, E. Tiesinga, J. V. Porto and C. J. Williams,
"Effective three-body interactions of neutral bosons in optical lattices",
New Journal of Physics 11 (2009) 093022.

[94] K. Zhou, Z. Liang and Z. Zhang, "Quantum phases of a dipolar Bose-Einstein condensate in an
optical lattice with three-body interaction", *Phys. Rev. A* 82 (2010) 013634.

[95] J. Silva-Valencia and A. M. C. Souza,
"First Mott lobe of bosons with local two- and three-body interactions",
Phys. Rev. A 84 (2011) 065601.

[96] M. Singh, A. Dhar, T. Mishra, R. V. Pai and B. P. Das, "Three-body on-site interactions in
ultracold bosonic atoms in optical lattices and superlattices",
Phys. Rev. A 85 (2012) 051604(R).

[97] T. Sowiński, "Exact diagonalization of the one-dimensional Bose-Hubbard model with local
three-body interactions", *Phys. Rev. A* 85 (2012) 065601.

[98] C. N. Yang and C. P. Yang,
"One-Dimensional Chain of Anisotropic Spin-Spin Interactions III: Applications",
Phys. Rev. 151 (1966) 258.

[99] N. J. A. Sloane, *The On-Line Encyclopedia of Integer Sequences*,
`http://oeis.org/A006318`, 2012.

[100] M. Campostrini, M. Hasenbusch, A. Pelissetto, P. Rossi and E. Vicari,
"Critical behavior of the three-dimensional XY universality class",
Phys. Rev. B 63 (2001) 214503.

[101] A. Safavi-Naini, J. von Stecher, B. Capogrosso-Sansone and S. T. Rittenhouse, "First-Order
Phase Transitions in Optical Lattices with Tunable Three-Body Onsite Interaction",
Phys. Rev. Lett. 109 (2012) 135302.

[102] T. Sowinski, R. W. Chhajlany, O. Dutta, L. Tagliacozzo and M. Lewenstein,
"Violation of the universality hypothesis in ultra-cold atomic systems",
arXiv:1304.4835 [cond-mat.quant-gas](unpublished), Apr. 2013.

[103] H. Matsuda and T. Matsubara, "A Lattice Model of Liquid Helium I",
Prog. Theor. Phys. 16 (1956) 569.

[104] J. Wilks, *The Properties of Liquid and Solid Helium*,
International Series of Monographs on Physics, Oxford: Oxford University Press, 1967.

[105] H. Matsuda and T. Tsuneto, "Off-diagonal Long Range Order in Solids",
Prog. Theo. Phys., Suppl. 46 (1970) 411.

[106] K. S. Liu and M. E. Fisher, "Quantum Lattice Gas and the Existence of a Supersolid",
J. Low Temp. Physics 10 (1973) 655.

[107] R. T. Scalettar, G. G. Batrouni, A. P. Kampf and G. T. Zimanyi,
"Simultaneous diagonal and off-diagonal order in the Bose-Hubbard Hamiltonian",
Phys. Rev. B 51 (1995) 8467.

[108] M. Boninsegni and N. V. Prokof'ev, "*Colloquium* : Supersolids: What and where are they?",
Rev. Mod. Phys. 84 (2 2012) 759.

[109] K. Bernardet, G. G. Batrouni, J.-L. Meunier, G. Schmid, M. Troyer and A. Dorniech,
"Analytical and numerical study of hardcore bosons in two dimensions.",
Phys. Rev. B 65 (2002) 104519.

[110] I. Hen and M. Rigol,
"Superfluid to Mott insulator transition of hardcore bosons in a superlattice",
Phys. Rev. B 80 (2009) 134508.

[111] T. Coletta, N. Laflorencie and F. Mila,
"Semiclassical approach to ground-state properties of hard-core bosons in two dimensions",
Phys. Rev. B 85 (2012) 104421.

[112] S.-K. Ma, *Statistical Mechanics*, Singapore: World Scientific Press, 1985.

[113] A. Auerbach, *Interacting Electrons and Quantum Magnetism*,
New York: Springer-Verlag, 1994.

[114] V. L. Pokrovsky and A. L. Talapov, "The theory of two-dimensional incommensurate crystals",
Sov. Phys. JETP 51 (1980) 134.

[115] B. Bauer, L. D. Carr, H. G. Evertz, A. Feiguin, J. Freire, S. Fuchs, L. Gamper, J. Gukelberger,
E. Gull, S. Guertler, A. Hehn, R. Igarashi, S. V. Isakov, D. Koop, P. N. Ma, P. Mates,
H. Matsuo, O. Parcollet, G. Pawlowski, J. D. Picon, L. Pollet, E. Santos, V. W. Scarola,
U. Schollwoeck, C. Silva, B. Surer, S. Todo, S. Trebst, M. Troyer, M. L. Wall, P. Werner and
S. Wessel,
"The ALPS project release 2.0: open source software for strongly correlated systems",
Journal of Statistical Mechanics: Theory and Experiment 2011 (2011) P05001.

[116] F. Hebert, G. G. Batrouni, R. T. Scalettar, G. Schmid, M. Troyer and A. Dorneich,
"Quantum Phase transitions in the hard-core boson model", *Phys. Rev. B* 65 (2001) 014513.

[117] C. Bruder, R. Fazio and G. Schön,
"Superconductor-Mott-insulator transition in Bose systems with finite-range interactions",
Phys. Rev. B 47 (1993) 342.

[118] C. Pich and E. Frey,
"Phase diagrams, critical, and multicritical behavior of hard-core Bose-Hubbard models",
Phys. Rev. B 57 (1998) 13712.

[119] P. A. Lee, "An End to the Drought of Quantum Spin Liquids",
Science 321.5894 (2008) 1306–1307.

[120] J. S. Helton, K. Matan, M. P. Shores, E. A. Nytko, B. M. Bartlett, Y. Yoshida, Y. Takano,
A. Suslov, Y. Qiu, J.-H. Chung, D. G. Nocera and Y. S. Lee,
"Spin Dynamics of the Spin-1/2 Kagome Lattice Antiferromagnet $ZnCu_3(OH)_6Cl_2$",
Phys. Rev. Lett. 98 (10 2007) 107204.

[121] S. V. Isakov, M. B. Hastings and R. G. Melko,
"Topological entanglement entropy of a Bose-Hubbard spin liquid",
Nature Physics 7.10 (2011) 772.

[122] S. V. Isakov, R. G. Melko and M. B. Hastings,
"Universal Signatures of Fractionalized Quantum Critical Points",
Science 335.6065 (2012) 193.

[123] T.-H. Han, J. S. Helton, S. Chu, D. G. Nocera, J. A. Rodriguez-Rivera, C. Broholm and
Y. S. Lee,
"Fractionalized excitations in the spin-liquid state of a kagome-lattice antiferromagnet",
Nature 492.7429 (2012) 406–410.

[124] J. Simon, W. S. Bakr, R. Ma, M. E. Tai, P. M. Preiss and M. Greiner,
"Quantum simulation of antiferromagnetic spin chains in an optical lattice",
Nature 472 (2011) 307.

[125] A. Sommer, M. Ku and M. W. Zwierlein,
"Spin transport in polaronic and superfluid Fermi gases",
New Journal of Physics 13.5 (2011) 055009.

[126] B. Paredes, A. Widera, V. Murg, O. Mandel, S. Folling, I. irac, G. V. hlyapnikov, T. W. Hansch
and I. Bloch, "Tonks-Girardeau gas of ultracold atoms in an optical lattice",
Nature 429 (2004) 277.

[127] G.-B. Jo, J. Guzman, C. K. Thomas, P. Hosur, A. Vishwanath and D. M. Stamper-Kurn,
"Ultracold Atoms in a Tunable Optical Kagome Lattice", *Phys. Rev. Lett.* 108 (2012) 045305.

[128] L. D. Landau and E. M. Lifshitz, *Statistical Physics I*, Third Edition,
Oxford: Butterworth-Heinemann, 1980.

[129] L. Zhu, M. Garst, A. Rosch and Q. Si, "Universally diverging Gruenerisen parameter and the
magnetocaloric effect close to quantum critical points", *Phys. Rev. Lett.* 91 (2003) 066404.

[130] M. Takahashi, "Simplification of Thermodynamic Bethe Ansatz equations",
Physics And Combinatorics, chap. 13 299–304.

[131] L. Onsager,
"Crystal Statistics. I. A Two-Dimensional Model with an Order-Disorder Transition",
Phys. Rev. 65 (1944) 117.

[132] K. Huang, *Statistical Mechanics*, USA: John Wiley and Sons, Inc., 1987.

[133] H. Bethe,
"Zur Theorie der Metalle. I. Eigenwerte und Eigenfunktionen der linearen Atomkette",
Zeitschrift fuer Physik 71 (1931) 205.

[134] P. Azaria, H. T. Diep and H. Giacomini,
"Coexistence of order and disorder and reentrance in an exactly solvable model",
Phys. Rev. Lett. 59 (1987) 1629.

[135] A. Gaaff and J. Hijmans, "Symmetry relations in the sixteen-vertex model",
Physica A: Statistical and Theoretical Physics 80 (1975) 149.

[136] C. Fan and F. Y. Wu, "General Lattice Model of Phase Transitions",
Phys. Rev. B 2 (1970) 723.

[137] G. Baym and C. Pethick, *Landau Fermi-liquid theory*, Weinheim: Wiley-VCH Verlag, 2004.

[138] S. V. Isakov, S. Wessel, R. G. Melko, K. Sengupta and Y. B. Kim,
"Hard-core bosons on the kagome lattice: Valence-bond solids and their quantum melting",
Phys. Rev. Lett. 97 (2006) 147202.

[139] K. Damle and T. Senthil,
"Spin nematics and Magnetization Plateau Transition in Anisotropic Kagome Magnets",
Phys. Rev. Lett. 97 (2006) 067202.

[140] R. Moessner, S. L. Sondhi and P. Chandra,
"Phase diagram of the hexagonal lattice quantum dimer model",
Phys. Rev. B 64 (2001) 144416.

[141] T. Vekua and A. Honecker, "Quantum dimer phases in a frustrated spin ladder: Effective field theory approach and exact diagonalization", *Phys. Rev. B* 73 (2006) 214427.

[142] D. C. Cabra, M. D. Grynberg, P. C. W. Holdsworth, A. Honecker, P. Pujol, J. Richter, D. Schmalfuss and J. Schulenburg, "Quantum kagome antiferromagnet in a magnetic field: Low-lying nonmagnetic excitations versus valence-bond crystal order",
Phys B 71 (2005) 144420.

[143] S. V. Isakov, K. Sengupta and Y. B. Kim, "Bose-Hubbard model on a star lattice",
Phys. Rev. B 80 (2009) 214503.

[144] K.-K. Ng, "Phase diagrams of the XXZ model on a depleted square lattice",
Phys. Rev. B 81 (2010) 094426.

[145] J. Oitmaa, W. Zheng and D. Tompsett,
"Hard-core bosons on the triangular lattice at zero temperature: A series expansion study",
Phys. Rev. B 73 (2006) 172401.

[146] A. Sen, K. Damle and T. Senthil,
"Superfluid insulator transitions of hard-core bosons on the checkerboard lattice",
Phys. Rev. B 76 (2007) 235107.

[147] R. J. Donnelly, *Experimental Superfluidity*, Chicago: Univ. of Chicago Press, 1967, chap. 3.

[148] G. Chen and L. Balents,
"Spin-orbit effects in $Na_4Ir_3O_8$: A hyper-kagome lattice antiferromagnet",
Phys. Rev. B 78 (2008) 094403.

[149] A. J. Leggett,
Quantum liquids: Bose condensation and Cooper pairing in condensed-matter systems,
New York: Oxford University Press, 2006.

[150] C. N. Yang, "Concept of Off-Diagonal Long-Range Order and the Quantum Phases of Liquid He and of Superconductors", *Rev. Mod. Phys.* 34 (1962) 694.

[151] L. Pitaevskii and S. Stringari,
"Uncertainty principle, quantum fluctuations, and broken symmetries",
Journal of Low Temperature Physics 85 (1991) 377.

[152] N. R. Cooper and Z. Hadzibabic,
"Measuring the Superfluid Fraction of an Ultracold Atomic Gas",
Phys. Rev. Lett. 104 (2010) 030401.

List of Figures

List of Tables

Glossary and Abbreviations

$\hat{a}, \hat{a}^\dagger, \hat{b}, \hat{b}^\dagger$	Second-quantized field operators
BHH	Bose-Hubbard Hamiltonian
BKT	Berezinskii-Kosterlitz-Thouless
β	Inverse temperature
C_v	Constant volume specific heat density
DOS	Density of states
E_0	Ground state energy density
ϵ	Energy variable
Γ	Grüneisen parameter
h	Longitudinal magnetic field
$\mathcal{H}$	Hamiltonian
HCB	Hard-core boson
J	Spin coupling
k_B	Boltzmann's constant
$\mathbf{k}$	Lattice momentum
K	Compressibility
LGF	Lattice Green's function
λ	t/U
MF	Mean field
MI	Mott insulator
μ	Chemical potential
n_b	Boson density
PA	Padé approximant
ψ	Wavefunction
ρ	Particle density
$\rho(\epsilon)$	Density of states
R	Gas constant
S	Entropy density
SF	Superfluid
SW(T)	Spin wave (theory)
t	Nearest neighbour particle hopping amplitude
T	Temperature
U	On-site particle repulsion
V	Nearest neighbour particle interaction
VBS	Valence bond solid
$\mathcal{Z}, \Omega$	Partition function

Acknowledgements

I dedicate this page to my many kind benefactors who have helped "*forge in the smithy of my soul*" the community's shared scientific responsibility. I am constantly reminded, as I stand and stood atop others' shoulders, often with great trepidation, often with the heavy brunt of imperfect knowledge, that my humbling vantage point is and never will be my own. These giants of heroic hearts merit more than my words and work; for what I can give back and for what it's worth, I request, as if their measure be lacking, a morsel more of their infinite endurance and indulgence in accepting my gratitude, a gratitude that gently corrects, fondly cherishes, yet ever falls short:

Prof. Hartmut Monien, my thesis advisor, for his guidance and encouragement in all forms scientific and otherwise; his presence has been a remarkable and electric singularity during my graduate years.

Priv.-Doz Ralf Bulla for his careful mentoring, support and constant interest in my work.

Prof. Rajiv Singh for his many patient explanations, collaboration and advice.

Prof. Simon Trebst for rewarding correspondence and interactions.

In addition, I thank the researchers acknowledged in individual chapters for discussions which were instrumental in the progress of the research; Prof. Martin Weitz and Prof. Werner Müller for their generous time and efforts in forming the thesis committee; and Prof. Dieter Meschede for discussions and his interest. I am grateful to the selfless employees at the Physics Institute, in particular Herr. Dr. Wisskirchen, Frau. Zündorf and Frau. Weiss; Jie Gu for proofreading this work (any remnant misprints or notational inconsistencies are entirely his fault); and Evaristus Fuh Chuo for partaking in some of the related bureaucratic thrills.